Montclair State University
Montclair State University Digital Commons

Theses, Dissertations and Culminating Projects

5-2017

Determining Late Pleistocene to Early Holocene Deglaciation of the Baltic Ice Lake Through Sedimentological and Geochemical Analysis of IODP Site M0064

April Lynn Kelly

Follow this and additional works at: https://digitalcommons.montclair.edu/etd

 Part of the Earth Sciences Commons, and the Environmental Sciences Commons

Abstract

IODP Site M0064 within the Baltic Sea's Hanö Bay was drilled to investigate the deglaciation history of the Scandinavian Ice Sheet (SIS) from the Late Pleistocene to the Holocene. This research aims to better understand how deglaciation speed, SIS drainage patterns, and changes in relative sea level influences sediment deposition within the Baltic Ice Lake (BIL) on a high-resolution timescale. Site M0064 contains diamicton at ~47 – 9 mbsf, followed by an upward transition to cm-scale grey thinly laminated rhythmites at ~8 mbsf, and a sharp 2.5 cm thick dark brown organic layer at ~7.87 msbf, transitioning to reddish-brown thinly laminated rhythmites up section. Previous modeling, glacial till, and surface exposure dating studies have suggested ice retreated near the project site ~16.7 ka BP, signifying the project site underwent a subglacial to proglacial transition within the SIS's most recent deglaciation between 20 and 14 ka BP. This research uses particle size analysis to determine the late glacial depositional environment, and ICP-OES, –MS and XRF geochemical analysis to decipher the potential redox changes, Zr/Al ratios to understand meltwater current strength, and Al/Ti ratios to shed light on sediment provenance. Samples were chosen based on high-resolution core images using color and compositional transitions. XRF core scanning of the varve sequence at 1-cm intervals increased geochemical resolution of all listed elemental ratios. Averaged varve counting provided the time Site M0064 was influenced by annual meltwater fluxes, ~72 years. Particle size results yield a subglacial to proglacial shift, however alternating silt and clay layers in the notably color-changing varve sequence exhibit no grain size variation. Mn/Al ratios show little to no variation in redox sensitivity, and Zr/Al ratios exhibit no meltwater spikes across the color change. Grey varves in Unit IIIb display remarkable Th-enrichments, indicating a likely source change from a south central Swedish province, or the Norwegian Oslo igneous province, while the brown organic layer and red varves may originate from the Esrum/Alnarp paleovalley Jurassic red sandstones and coal seams. Based on data collected, the color shift in the varve sequence is not a

direct result of the BIL drainage 11,620 ka BP, but potentially an indirect result, causing a provenance change.

MONTCLAIR STATE UNIVERSITY

Determining Late Pleistocene to Early Holocene deglaciation of the Baltic Ice Lake through sedimentological and geochemical analysis of IODP Site M0064

by

April Kelly

A Master's Thesis Submitted to the Faculty of

Montclair State University

In Partial Fulfillment of the Requirements

For the Degree of

Master of Science

May 2017

College/School: College of Science and Mathematics

Department: Earth and Environmental Science

Thesis Committee:

[redacted]

Sandra Passchier
Thesis Sponsor

[redacted]

Stefanie Brachfeld
Committee Member

[redacted]

Xiaona Li
Committee Member

DETERMINING LATE PLEISTOCENE TO EARLY HOLOCENE DEGLACIATION OF THE BALTIC ICE LAKE THROUGH SEDIMENTOLOGICAL AND GEOCHEMICAL ANALYSIS OF IODP SITE M0064

A THESIS

Submitted in partial fulfillment of the requirements

For the degree of Master of Science

by

APRIL LYNN KELLY

Montclair State University

Montclair, NJ

2017

Copyright © 2017 by *April Lynn Kelly*. All rights reserved.

Acknowledgements

I would like to thank my advisor, Dr. Sandra Passchier, for giving me the opportunity to work on this project, and for guiding me through the process of proposal writing, data collection, and result analysis. I would also like to thank Dr. Stefanie Brachfeld and Dr. Xiaona Li for their support with my thesis project. Additionally, I would like to thank the other professors and Earth and Environmental Science graduate students at Montclair State University for their added knowledge and motivation throughout my academic career. I also want to thank all my professors at James Madison University, especially Dr. Anna Courtier and Dr. Kristen St. John, for providing me with basic geologic skills, and believing in me as an aspiring graduate student in paleoclimatology. My passions and drive for paleoclimatology, and for studying marine sediment cores, was immensely supported by these women, and by Dr. Passchier, and for this I am very grateful. I would also like to thank the engineers and scientists at the University of Bremen-MARUM for allowing me to use their facilities to complete my XRF data collection, and for being such humble hosts, especially Mrs. Vera Lukies and Dr. Ursula Röhl. Financial support from the IODP U.S. Science Support Program, a student research award from the Geological Society of America, a Vivian travel award from the department of Earth and Environmental Studies, and a graduate assistantship from Montclair State University, are greatly appreciated. Lastly, I would like to thank my family for their unconditional love and support.

Table of Contents **Page**

List of Figures **Page**

List of Tables **Page**

1. Introduction

The southwestern portion of the Baltic Sea is situated south of Sweden, north of Germany, and east of Denmark. Connected to the North Sea and the North Atlantic Ocean by the Danish straits of the Kattegat region, the modern Baltic Sea Basin is the largest brackish water body on Earth (Harff et al., 2011). In the past, the shape and depth of the Baltic Sea was largely influenced by glacial processes of the Scandinavian Ice Sheet (SIS), as the Baltic Sea was geomorphologically developed during the Quaternary (Harff et al., 2011). A large portion of the landmasses above 60° N latitude was covered in ice ~20 ka BP (Stroeven et al., 2015). The SIS's role and implications for climate change, relative sea level change, and influence on the North Atlantic, however, has been sparsely investigated in comparison to its western hemisphere counterpart, the Laurentide Ice Sheet (LIS) (Toucanne et al., 2015).

The southwest region of the Baltic Sea is important for understanding the glacial history of the SIS because it contains high-resolution sediment records of climate and relative sea level changes in the Late Pleistocene to the Holocene Epochs (Houmark-Nielsen, 2010). This region's significance also pertains to the Last Glacial Maximum (LGM, ~25 - 20 ka BP), and the deglaciation phase that followed (20 – 15 ka BP) (Houmark-Nielsen, 2010). A large ice-dammed lake, known as the Baltic Ice Lake (BIL) began to form ~ 20 ka BP as the SIS retreated to the north and the east in this subsequent deglaciation phase (Jakobsson et al, 2007; Larsen et al., 2009).

There is a general agreement on the timing and extent of the Scandinavian Ice Sheet glaciations throughout the Late Pleistocene (Houmark-Nielsen, 2010; Houmark-Nielsen and Kjaer, 2003; Jakobsson et al., 2007; Larsen et al., 2007) however, these events are poorly constrained in the southwestern Baltic Sea, the Baltic Sea Basin, and the Kattegat region (Andrén et al., 2011; Anjar et al., 2014). Due to the limited availability of reliable age constraints in the region, forming a well-constrained deglacial history for this area has proven to be a difficult task (Anjar et al., 2014). High-resolution archives such as varved lake sediments from the Baltic Ice

Lake (BIL) will hopefully shed light on the last deglaciation cycle, and other abrupt climate changes due to the collapse of the SIS.

The onset of the recession of the SIS has been thought to coincide with Heinrich Event I (~18.2 – 16.7 ka BP), the Bølling-Allerød warming (~14.7 – 12.7 ka BP), and the disturbance of the Atlantic Meridional Ocean Circulation (AMOC) (Jakobsson et al., 2007; Larsen et al., 2009; Toucanne, et al., 2015). Heinrich stadial events are classified as sudden releases of cold freshwater into the saline Atlantic Ocean, resulting from calving ice sheets that release and deposit coarse sediment (Jakobsson et al., 2007; Toucanne et al., 2015). According to Jakobsson et al. (2007), these large freshwater influxes into the oceans have been witnessed in geological records, and are a result of the intense drainages of ice-dammed lakes. An unstable ice-dammed lake such as the BIL could be a source of this catastrophic event, where lower terrain becomes exposed, and the hydrostatic pressure of the lake suddenly exceeds the pressure of the overburden ice, causing an ice-dam failure and abrupt water release (Stroeven et al., 2015). This catastrophic water release into the Atlantic Ocean has been thought to take place in only a matter of 1 – 2 years (Andrén et al., 2002; Andrén et al., 2011; Björck et al., 1996; Jakobsson et al., 2007).

Across western Europe, rapidly increased temperatures of 3 – 5 °C were witnessed at the onset of the Bølling-Allerød warming (Clark et al., 2012). Studies have suggested that SIS deglaciation and freshwater outbursts into the North Atlantic have disturbed, or possibly shut down the North Atlantic deep water formation, disrupting the Earth's climate system and causing cooling events, such as the Younger Dryas (YD) (~12.9 – 11.7 ka BP), during the last deglaciation period (Jakobsson et al., 2007, Toucanne et al., 2015, Larsen et al., 2009). The onset of the YD cooling period experienced a range of decreased temperatures in western Europe, from 5 – 10°C (Clark et al., 2012).

Between 17 and 14 ka BP, freshwater release into the Atlantic Ocean due to melting ice sheets contributed to eustatic sea level to rise four meters per century, accompanied by a dramatic

increase in greenhouse gases (Clark et al., 2012). However, a data gap is present in the sea level curve between 17 and 15 ka BP (Clark et al., 2012), and this glacial varve study will potentially shed light on this period of uncertainty. This period of rapid eustatic sea level rise and global warming is a valuable analog for understanding the Earth's current and projected climate.

Sedimentological analysis of detrital sediments during this time of rapid climate change and ice sheet retreat will yield evidence of SIS and BIL dynamics, and the paleoenvironmental processes that influenced these changes, using an Integrated Ocean Drilling Program (IODP) sediment core. Sediment particle size analysis will determine the late-glacial depositional environment, and if any color changes in the core are associated with changes in grain size. Provenance and Baltic bottom water redox conditions will also be investigated using particle size and geochemical methods to better understand the drainage of the BIL along with SIS retreat, and how these two dynamic processes interacted as a paleoenvironmental system. Combining multiple geochemical methods for high resolution results in varved lake sediments will yield further evidence of changing bottom water redox conditions in the BIL, and will test the hypothesis of dramatic color changes in the sediment core due to these chemical conditions at a high-resolution time scale.

1.1 Hanö Bay and IODP Exp. 347 Site M0064

In Fall 2013, the Integrated Oceanic Drilling Program (IODP) Expedition 347 retrieved sediment cores from nine varying sites within the Baltic Sea, encompassing glacial-interglacial cycles of the Scandinavian Ice Sheet (SIS). This expedition was designed to investigate climate fluctuations during MIS 5 (130 - 80 ka BP), changes during the last glacial cycle and MIS 4 through MIS 2 (74 - 24 ka BP), climate forcing throughout MIS 2 and MIS 1 (24 - 11.6 ka BP), and dynamics regarding the deep Baltic biosphere, and relative sea level changes (Andrén et al., 2013). The focus of this study is Site M0064, located in the southwest portion of the Baltic Sea, in Hanö Bay (Figure 1B). This site is significant to Exp. 347 because it rests in the location of

what once was the Baltic Ice Lake (BIL), a prime location for sediment deposits from MIS 2 and MIS 1 (24 - 11.6 ka BP). These sediments will help increase our understanding of SIS meltwater pulse fluctuations, changes in relative sea level, and climate forcing during this time period.

From October 22 to 24, 2013, IODP Expedition 347 underwent operations at Site M0064 within Hanö Bay, a shallow offshore basin of the Baltic Sea ~60m water depth (Figure 2A), and a bedrock region characterized by Cretaceous chalk and clayey carbonates (Figure 3). Exp. 347 recovered four holes (A-D) at Site M0064 to develop a complete stratigraphic recovery with at least three replicated sediment copies, drilling to a depth of 60.5 mbsf in Hole M0064A and 59.8 mbsf in Holes M0064B-D. This study focuses on Hole M0064D, but also uses correlating samples from Hole M0064A.

The seismic profile sediment sequence shows ~10m of mud and clay at the top, and a thick, transparent sediment sequence, with alternating p-wave velocities in Unit IVa (Figure 2B). The drilled sequence is divided into four major lithostratigraphic units (Units I - IV) based on their sedimentology (Figure 2B). Seafloor bathymetry shows relatively flat seafloor (Figure 2B). Units III and IV and their subdivisions are the main focus of this study (Figure 4). Unit III is a dark grayish brown laminated clay and silty clay with randomly distributed clasts, ~8.5m thick. Unit III is subdivided into two smaller units, where Unit IIIb (7.87 – 9.3 mbsf of M0064D) is gray in color and Unit IIIa (1.75 – 7.87 mbsf of M0064D) is red-brown, with a dark brown layer at its base (Figure 5). Unit IV is subdivided into three smaller units of moderately to poorly sorted, matrix-rich diamicton. Unit IVa is a stratified muddy diamicton with sandy gravel (9.3 – 25.4 mbsf of M0064D) while Unit IVb is a massive gray diamicton with possible shearing (25.4 – 41.2 mbsf of M0064D). Unit IVc, only recovered in Holes M0064A and C, is a stratified sandy clayey silt with dispersed diamicton and clasts ~7m thick.

1.2 Regional Geology of the Baltic Sea

The formation of the Baltic Sea is still not entirely understood, as the basin contains erosional structures that contributed to the development of a tectonic depression (Šliaupa and Hoth, 2011). The Baltic Sea basin is located on the Baltic Shield containing the oldest rocks of Europe. The Baltic Shield is composed of Archean and Proterozoic rocks of the Precambrian, situated in parts of Norway, Sweden, Finland, and northwest Russia (Lahtinen, 2012). Four major Archean provinces are located in the east and north of Fennoscandia, composed of plutonic and volcanic rocks, granitoids, and ophiolite rocks, ranging in age from 3.0 – 2.72 Ga (Lahtinen, 2012). The Archean rocks are covered by paleoproterozioc rocks, 2.50 – 1.95 Ga. Rifting of the Archean continent became more pronounce after plume-related igneous intrusions and dyke swarms occurred. Huronian glaciation and further rifting events, 2.4 – 2.1 Ga, are connected to mafic dyke and sill deposits, along with local fluvial, and shallow marine carbonate sedimentary rocks (Lahtinen, 2012). Deep marine turbidite deposits and oceanic crustal rocks were deposited 1.95 Ga ago in association with the rifting (Lahtinen, 2012). Paleoproterozoic orogenic rocks are found in the northeastern and central parts of the Baltic Shield, 1.94 – 1.79 Ga in age. The region is made up of island arc rocks and mostly felsic granulites (Lahtinen, 2012).

Rocks in southwest Fennoscandia are characterized by rapakivi granites (1.65 – 1.47 Ga) from repeated orogenies, and post orogenic magmatism, Meso- and Neoproterozoic in age (Lahtinen, 2012). The ending of orogenic events that directly affected the establishment of the Baltic Shield began with the opening of the Iapetus Ocean, ~600 Ma ago, consisting of Phanerozoic ophiolites and island-arc type rocks (Lahtinen, 2012). Lastly, further rift magnetism, as seen in the Oslo Rift of southeastern Norway, consists of Th- and U- rich granitoids (Bonin and Sorenson, 2003; Killeen and Heier, 1975).

The southwest portion of the Baltic Sea sedimentary basin is said to have originated from lithospheric reactivation of the East European craton during the Late Ediacaran – Early Cambrian, experiencing the sea's first wide transgression (Šliaupa and Hoth, 2011). However, the major

basin subsidence that formed this geomorphological feature occurred during the Late Ordovician – Middle Silurian, and was dominantly driven by regional tectonic divergence (Šliaupa and Hoth, 2011). This period was followed by numerous igneous intrusions, in addition to late Permian – early Carboniferous magmatism (Šliaupa and Hoth, 2011).

The first sea transgression deposited sandstones and conglomerates > 100 m thick in a floodplain paleoenvironment, and by the middle of the Early Cambrian, quartz sandstones, siltstones and shales were deposited, thicknesses ranging from 250 – 500 m in the central Baltic to the southwest, north central of Poland (Šliaupa and Hoth, 2011). Deposition of shaly carbonates continuously progressed in the Ordovician (~250 m thick), and sedimentation rate increased in the Silurian, with 3,500 m thicknesses of interbedded marlstones and limestones in the southwest (Šliaupa and Hoth, 2011).

Sedimentation of Devonian aged material occurred in the central region of the Baltic, recording shallow marine and shore environments with the deposition of interbedded sandstones and shales alternating with carbonates and marlstones, up to 1,050 m thickness (Šliaupa and Hoth, 2011). Sedimentation shifted southwest in the Permian, while the Mesozoic and Cenozoic time periods had non-depositional spells intermittently broken up by marine transgressions from the west (Šliaupa and Hoth, 2011).

The Upper Permian contains 350 m thick carbonate and evaporate deposits, and the Lower Triassic consists of 200 m thick lacustrine mudstones, red in color, that transition to deeper marine sediments- fine grained arkosic sandstones (Šliaupa and Hoth, 2011). The Jurassic contains fine-grained sandstones, siltstones and shales, transitioning from lacustrine to marine sediments, with occasional coaly beds (Nielsen, 2003, Šliaupa and Hoth, 2011). This material outcrops near the southern coast of the Baltic Sea, and trends NW-SE in southern Sweden, and south of Bornholm (Figure 3).

The Cretaceous aged material, 400 m thick, is composed of two facies. The older of the two consists of glauconitic sandstones and siltstones, and the younger is of Upper Cretaceous

chalk, marlstones, and siltstones (Šliaupa and Hoth, 2011). This region of the Baltic Sea sedimentary basin is of specific importance as it is where IODP Site M0064 resides (Figure 3). These rock types outcrop within Hanö Bay, along the coast of southern Sweden, as well as the Baltic Sea's southern coast.

1.3 Glacial History of the Southwestern Baltic Sea

The southwestern portion of the Baltic Sea region was particularly influenced by the waxing and waning of the SIS, and ultimately affected by the LGM in the Late Pleistocene and the Early Holocene, due to its prime location. Prior to the LGM, however, the southwestern Baltic may have experienced a major advance 50 ka BP, and another at 30 ka BP during MIS 3, including the deposition of brackish marine sediments (Andrén et al., 2011). This less known geologic time is followed by stratigraphically complex glacial diamicts, varved clay deposits and organic-rich material with radiocarbon dates greater than 35 ka BP in Hanö Bay, representing the largely variable glaciation leading up to the LGM (Andrén et al., 2011). Sediments with these ages were discovered northeast of Hanö Bay in southwest Skåne within a buried (60 m below present sea level) bedrock valley known as the Esrum/Alnarp valley, a sediment fill in MIS 3, and a possible route for Baltic Sea and Atlantic Ocean water flux ~33 ka BP (Andrén et al., 2011; Houmark-Nielsen and Kjaer, 2003). This paleovalley contains Late Triassic to Jurassic aged arkosic sandstones, mudstones, with occasional coaly beds and coal seams once deposited by fluvial channels and a shallow marine/swamp paleoenvironment (Figure 3) (Nielsen, 2003, Šliaupa and Hoth, 2011).

Following the LGM 20 ka BP, the retreat of the SIS western margin was progressing toward the east and to the north by 19 ka BP (Figure 6) (Houmark-Nielsen and Kjaer, 2003). By ~17 ka BP, the western margin had retreated to southwest Sweden, depositing the Halland coastal moraines, cosmogenically age dated to 16.8 ka BP (Anjar et al., 2014; Houmark-Nielsen and Kjaer, 2003). As deglaciation continued to the west, Bornholm Island was deglaciated at the same

time as central Skåne, 16.6 ± 0.9 ka BP, and a lobe of the SIS may have been present in Hanö Bay during this time (Figure 7) (Anjar et al., 2014). From ~16 ka BP on, the SIS continued its northern retreat, reaching Mt. Billingen in south central Sweden by ~11.7 ka BP (Jakobsson et al., 2007). This rapid deglaciation produced large volumes of meltwater, yielding high sedimentation rates in the southwestern Baltic (Björck et al., 1996). Accelerated sedimentation rates and isostatic uplift resulted in decreased relative water depth, and created a land bridge between Denmark and Sweden through the Öresund strait, blocking any water flux between the Baltic and the Atlantic (Björck et al., 1996). This deglacial process likely formed the BIL.

The end of a steady marginal stand still and possible SIS readvance at Mt. Billingen marked the termination of the Younger Dryas (YD). The SIS margin contact with Mt. Billingen withheld the ice-dammed lake (Figure 8) until approximately 12,867±66 cal. years BP (Muschitiello et al., 2016), when the margin retreated far enough north to open up a westward connection and drain the BIL, releasing cold freshwater (Andrén et al., 2002; Jakobsson et al., 2007; Stroeven et al., 2015). The BIL level catastrophically dropped 10 – 25 m, draining up to ~7800 km^3 of water in 1 – 2 years (Andrén et al., 2002; Anjar et al., 2002, Björck et al., 1996; Jakobsson et al., 2007; Muschitiello et al., 2016). The details of the BIL drainage are largely unknown, however, this water level regression has been based on lake isolation and modelling studies from shoreline displacement data (Andrén et al., 2002; Jakobsson et al., 2007).

Following this catastrophic drainage, the Baltic Sea transitioned into its next stage, the Yoldia Sea (YS), during the Preboreal warming at the onset of the Holocene Epoch (Andrén et al., 2002, Andrén et al., 2014, Björck et al., 1996). According to Björck et al., 1996, this shift from the YD to a Preboreal warming stage, 11,450 to 11,390 ± 80 years BP, is marked by a lithologic change in sediments from grey to brownish with an increased organic carbon content in southern Sweden. Björck et al. (1996) determined this age by combining high-resolution Greenland ice cores, German tree rings, and Scandinavian lacustrine records of the YD – Preboreal transition in the Yoldia Sea geologic time frame, dating the lithologic change with dense accelerator mass

spectrometry (AMS) ^{14}C measurements on plant remains (Björck et al., 1996).

The Yoldia Sea is characterized by rapid retreat of the SIS, freshwater and brackish phases of the Baltic, and rapid regressions and relative sea level changes influenced by isostatic rebound (Andrén et al., 2002, Andrén et al., 2014). The first 300 years of the YS constituted as a freshwater phase, where the YS was at level with the Atlantic, as meltwater was flowing out of the Baltic Basin (Andrén et al., 2002, Andrén et al., 2014). This freshwater phase is also a congruent with the Preboreal warming stage.

After this freshwater Preboreal stage, a brackish phase begun due to the influx of saline water through the lowlands of south-central Sweden, north of Mt. Billingen (Andrén et al., 2002, Andrén et al., 2014). This is inferred to have been the first time the Baltic Sea experienced a saline ingression, as no sedimentary indicators support a marine incursion prior to this brackish phase (Andrén et al., 2002). According to Andrén et al., 2002, the onset of this brackish stage is dated to 10,540 yr BP due to the occurrence of sulphide banding, distinct color peaks and increased silt fraction. This phase was likely a result of SIS meltwater decrease, following climate cooling (Andrén et al., 2002). After ~250-350 years, the brackish phase of the YS came to a halt, as isostatic rebound of south central Sweden progressed, causing the saline fluxing straits to uplift, and resulted in a rapid shallowing of the region, as recorded in the diatom record (Andrén et al., 2002). This led to the return of a freshwater basin, marking the end of the YS stage (Andrén et al., 2014). A timeline of the Baltic Sea stages including the BIL and the YS is represented in Table 1.

2. Methods and Materials

2.1 Laser Particle Size Distribution

Laser particle size analysis of marine sediment is particularly useful for accurately and precisely determining grain size distributions. Particle size distribution based on grain size, sorting, and changes throughout the core can give information regarding the late glacial depositional environment. Particle size percentages and sorting can determine if the project site

was in a subglacial or proglacial setting, where a subglacial paleoenvironment yields more poorly-sorted silty-sandy particles, and a proglacial paleoenvironment will have higher percentages of moderate-well sorted material. A glacial lacustrine setting can also be determined by grain size and sorting, where glacial varves are found in the sediment record (Ridge et al., 2012). Glacial varves are annually deposited sediments derived from the variation of seasonal glacial meltwater, resulting in high-resolution records of ice readvances and recessions during climate events (Ridge et al., 2012). Typically, the main melt season during the summer months deposits silts and fine sands, while the quieter winter season is exemplified by clay and very fine silts (Ridge et al., 2012).

Montclair State University's Malvern Mastersizer 2000 laser particle sizer was used to measure sediment particle size distributions of 53 samples from hole M0064A and M0064D, parts of Units IIIa, IIIb, IVa and IVb (Table 2). All M0064D samples available were measured, in addition to correlating M0064A samples. Seven additional samples were requested from the IODP core repository across the abrupt color transition exhibited from Unit IIIb to IIIa, and within the red varve sequence.

Laser Particle Size Sample Preparation

A portion of each sample was mixed with 50 mL of Millipore water in a 250 mL glass beaker to help disaggregate the grains. The sample was broken down with a rubber cork tool to help separate the grains in the mixture. If grains were not easily separated, the samples in solution were covered and left out overnight. When the sample had no consolidated clumps, the solution was then brought to a boil with a small amount (half scoop) of sodium pyrophosphate on a hot plate, and left to cool for 30 minutes before using the particle size analyzer. Measurements for these samples were only accepted if the laser obscuration was greater than 8% and less than 40%. A higher obscuration indicates a higher amount of suspended sediment in solution. If the laser obscuration was greater than 40%, more Millipore water was added to dilute the solution. If the

laser obscuration continued to exceed 40%, the sample was disregarded, and was re-prepared, and re-measured in the next batch of samples.

Laser Particle Size Instrumentation

Using a dual light-source, (a blue laser of shorter wavelength and a red laser of longer wavelength), grain sizes are measured using the angle created by the light refracting off each individual grain, and calculated using Mie optical theory, improving the accuracy of analysis in the finer sediment fraction (Sperazza et al., 2004). The particle size analyzer determines grain size distribution from 0.02 to 2000 μm, and grain size distribution follows the Udden-Wentworth scale, where clay ranges from 0.06 – 3.9 μm, silt is 4 – 63 μm, and sand ranges from 63 – 2000 μm.

The standard operating protocol used on the particle sizer was "marine sediments," which uses the refractive index of illite (1.6). The rotor speed on the dispersion unit of the instrument was set to 2000 rpm. The Mastersizer 2000 makes three measurements on each sample, and takes the average of the three measurements to result in frequency distributions of particle diameters.

2.2 Major and Trace Elements ICP-OES and ICP-MS

Inductively Coupled Plasma Optical Emissions Spectrometry (ICP-OES) and Inductively Coupled Plasma Mass Spectrometry (ICP-MS) geochemical analysis took place at Montclair State University to derive major and trace element abundance for 18 samples, which were chosen based on sediment color and compositional transitions. The ICP-MS trace element data for the sample from section depth 64D-18N-1W-58-60 at 28.98 mbsf in Unit IVb were discarded, therefore the results on 17 samples are used. The sample was omitted due to extremely low rare earth and trace element concentrations in the results for all three replicates, possibly due to an error in the sample dilution for ICP-MS. See Table 2 for sample descriptions.

- Unit IIIa samples (7.19, 7.2, 7.78, 7.83, 7.84, 7.85, 7.87 mbsf) were chosen based on the color transition from brown layer to red-brown varves. Two varve couplets were chosen, one couplet closest to the brown layer. All samples in brown layer were selected.
- Unit IIIb samples (8.22, 8.23, 8.4, 8.41 mbsf) were selected based on the defined grey varve couplets in the sequence.
- Unit IVa samples (10.2, 13.2, 13.7, 14.2, 14.7, 16.6, 25.7 mbsf) were selected based on the red colored diamict and coarse sand to pebble compositions.
- The sample in Unit IVb (32.83 mbsf) was selected for its mid-level position in the section.

ICP-OES sample preparation follows Murray (2000), and ICP-MS samples are diluted to 10,000X. The data will be used to determine the Al/Ti, Mn/Al and Zr/Al ratios and trace element abundances (Burdige, 1993, Calvert and Penderson, 1993, Young and Nesbitt, 1998). A potential source region of the selected sediments can be determined by analyzing the Al/Ti ratios, depositional redox conditions can be indicated by Mn/Al ratios, and Zr/Al ratios can indicate meltwater strengths. Trace element abundances and enrichment factors of specific rare earth elements (REE's) can have implications for felsic, mafic, and recycling source areas of sediments, determined by Th/Sc versus Zr/Sc ratios (McLennan et al., 1993). Enrichment factors of Ce relative to La and the heavy REE's may indicate higher salinity content, an interaction with seawater.

ICP-OES and ICP-MS Sample Preparation

Prior to ICP-OES geochemical analysis, samples in Units IVa and IVb were crushed to a powder using a mortar and pestle, using about ¼ of the original sample. Each sample was then placed in a plastic vile, labeled and closed. Samples in Units IIIa and IIIb were wet and soft, so ¼

of each sample was taken, placed in a ceramic bowl, and left to dry in the oven for three hours at 75°C. Once the samples were dried out, they were then crushed to a powder with a mortar and pestle, and placed in a plastic vile, labeled, and closed.

Approximately 0.0995 – 0.1005 grams of each sample was weighed and mixed with 0.3980 – 0.4010 grams of lithium metaborate flux. Each weight was recorded for all 18 samples, in addition to four blank samples that were prepared, one for each set of samples that were placed in the furnace. One blank sample was spilled, and was not used. Only three blank samples were used in total. Each sample and flux mixture was poured into a graphite crucible.

The samples were then placed in the furnace, set at 1050°C, for 30 minutes. During this time, a Teflon beaker and a stir rod for each sample was obtained, and placed on a balance. The weight of the beaker and stir rod was tared, and 50 mL of 7% nitric acid (HNO_3) solution was measured, added to the beaker, and recorded.

After 30 minutes of fusing the samples, the crucibles were taken out of the furnace, and the molten bead was carefully "popped" out of place by swirling the crucible in a quick, circular motion. Once the bead was disassembled from the crucible, it was dumped into the nitric acid solution, making hissing noise and shattering into pieces. The beakers with the stir rods were then placed on stirring plates to continue the bead dissolution process, taking anywhere from 5 – 30 minutes, depending on the sample. Once the samples were dissolved in solution, they were filtered using Whatman 540 filter paper, directly into a nalgene bottle. The circular filter paper was folded into a cone to create a funnel, and the solution was poured over it, being careful not to dump the stir rod in the filter.

A second dilution to 4000X is needed prior to measuring the samples on the ICP-OES. Two 6.5 mL aliquots of each sample solution were pipetted into a clean, empty 60 mL nalgene bottle using a 3250 µL pipette, and its weight was recorded. The mass of the bottle and sample solution was tared, and about 50 mL of 2% nitric acid was added to the sample solution and

weighed. The mass was recorded, and the samples were sealed and stored in a refrigerator to be sure no evaporation took place.

Major (Si, Ti, Al, Fe, Mn, Mg, Ca, Na, K, and P) and selected trace (Ba, Cr, Ni, Sc, Sr, V, Y, and Zr) element abundances were determined with the Jobin-Yvon Ultima ICP-OES. Rock standards determined by the USGS were prepared following the same methods and measured as unknowns (DNC-1, BHVO-2, W-2, AGV-2, MAG-1, SCO-1, BIR-1, GSP-2, G-2, BCR-2, QLO-1, RGM-1).

To prepare ICP-MS samples, a third dilution to 10,000X took place, using the original 500X sample solution. These samples were diluted directly into the ICP-MS tubes for measurement. A 60 mL nalgene bottle and an empty ICP-MS test tube was placed on the scale, and the mass was tared. The nalgene bottle was a convenient way of holding the test tube in place. 0.5 mL of the 500X solution was pipetted into the tube, and the mass was recorded. After taring the scale, 9.5 mL of 2% nitric acid is added to solution, and the mass was recorded. A separate pipette tip for every 500X sample bottle was used.

Major (Si, Ti, Al, Fe, Mn, Mg, Ca, Na, K, and P) and selected trace and rare earth element (REE) (Sc, V, Cr, Co, Ni, Ga, Rb, Sr, Y, Zr, Nb, Cs, Ba, La, Ce, Pr, Nd, Sm, Eu, Tb, Dy, Ho, Er, Tm, Yb, Lu, Hf, Ta, Pb, Th, and U) abundances were determined using the ICP-MS. Rock standards determined by the USGS that were prepared following the above procedure, including ppb standards, were also used and measured as unknowns (DNC-1, BHVO-2, W-2, AGV-2, MAG-1, SCO-1, BIR-1, GSP-2, G-2, BCR-2, QLO-1, RGM-1, Ba1ppb, Ce1ppb, Pr1ppb, Nd1ppb, and Sm1ppb).

Standard deviations of the elements used in this study were measured to determine if the ICP-OES element or ICP-MS element should be used. Based on the results, all major elements used in this study were taken from the ICP-OES measurements, and all trace and REE measurements were used from the ICP-MS data (Table 4).

ICP-OES and ICP-MS Instrumentation

The concentration for each element in a sample can be determined with the optical tools of the ICP-OES, and the mass filter of the ICP-MS. The ICP-OES and ICP-MS first convert the atoms into ions. Samples in their test tubes are placed in a sample rack, and a small portion of each sample is nebulized into an aerosol, then injected into the argon plasma through a narrow tube. The atoms reach an excited state when they encounter the argon plasma and also become ionized. In the ICP-OES, once the atoms return to the ground state, they emit photons at specific wavelengths characteristic to the element itself. The number of photons emitted at this specific wavelength is proportional to the concentration of the element within the sample. In the ICP-MS, the elements are brought to the mass spectrometer through the interface cones after ionization. The interface cones sample the central portion of the ion beam, and the ions are then separated by their mass-to-charge ratio through an electrostatic filter. The element is then identified by it's characteristic mass-to-charge ratio, where the counts are proportional to the elemental concentration.

The order of the sample measurements was placed in the sample rack at random for both the ICP-OES and ICP-MS, however the instrument was programmed to measure a drift solution after every fourth sample to measure for any fluctuations in the instrumentation. A deionized water rinse took place after every measurement to avoid contamination. The ICP-OES and ICP-MS measured each sample three times and calculated an average of the three. A total of four ICP-OES passes were completed, but only three were used because the argon tank unexpectedly ran out of gas on the first pass, and the changing of tanks in the middle of the run caused the drift to drastically plummet. Therefore, passes two, three, and four were used. Three ICP-MS runs were completed, where each sample was measured three times in one run, and the average of the three was calculated. Samples 7.2, 7.85, 8.22, 8.23, 10.2, 13.2, 14.2 and 25.7 mbsf were measured twice in each run due to the eight empty spaces in the sample rack, making these measurements twice as precise as the remaining nine samples.

The Excel spreadsheet used created a graph with intensity versus element concentration in solution for each measured element, which contained a calibration line that is obtained from the standard measurements. The initial masses of each sample were input to the ICP-OES Excel spreadsheet with the raw data, and corrected based off these measurements. The raw data was corrected for instrument drift and blank corrected. Elemental concentrations were determined using standard calibration equations. All three passes were then averaged and presented as weight percent (wt. %) oxides for the major elements and ppm for trace elements. The oxides were also mathematically removed in Excel, presenting the data in elemental wt. % so the data could also be compared to the XRF elemental counts, which are not presented in oxides.

2.3 XRF Core Scanning

XRF core scanning is a non-destructive method for rapid, high-resolution determination of chemical compositions and variations of split sediment cores composed of biogenic, terrigenous, and/or diagenetic mineral fractions. It is useful for determining paleoenvironmental conditions on a high resolution stratigraphic scale, and a high-resolution geologic time scale, specifically, the annual varve deposits in Units IIIa and IIIb. Using Al/Ti, Zr/Al and Mn/Al ratios, XRF scanning at 1-cm intervals can provide insight on changing provenance, meltwater, and bottom water oxygenation at a higher resolution than ICP-OES and ICP-MS methods. Elemental variations are measured as counts per unit area, as opposed to wt. % or ppm.

XRF Sample Preparation

XRF core scanning of eleven M0064D core sections (2.21 – 13.59 mbsf) took place at the MARUM-University of Bremen, Germany, where cores are stored in the IODP core repository (Table 3). Section 3H-CC is not used in the results, as it is a core catcher section containing overlapping data points from the section below (4H-1) that do not have matching or near-similar elemental counts.

XRF scanning methods and sample preparation followed Bahr et al. (2014), using the Avaatech XRF Core Scanner III (super slit). Archived half core section preparation began by removing the sections to be scanned that day from the core repository, so the sediment would soften at room temperature. Core sections were scanned in order from the upper most part of the core, down core. The archived core section was removed from its storage tube, and the end caps of the section were cut using pliers, so the plastic did not interfere with the sediment and the instrument. Then, the split-core surface was laterally smoothed over using a glass slide to remove any pore spaces, as the instrument is sensitive to variations in porosity, water content, and sediment density (Bahr et al. 2014). The glass slide was cleaned off after each use to avoid contamination. The surface was then covered with a 4 μm thin SPEXCerti Prep Ultralene1 foil to avoid instrument and sediment contamination, and was smoothed over using a kimwipe, removing any air bubbles between the foil and the sediment. The core section was carefully placed in the XRF core scanner, and scanning began. While this section was being scanned, the next core section was being prepared, following the same procedure.

XRF Instrumentation

The XRF scanner consists of the X-ray source, the detector, a Multi-Channel Analyzer, and the processing PC. X-ray radiation transferred from the instrument source to the core section results in an elemental characteristic wavelength emitted as electromagnetic radiation. Incoming X-ray radiation from the instrument ejects an inner shell electron. This electron vacancy is filled by an outer shell electron from a higher energy level. The energy difference between the outer and inner shell electron determines the wavelength of the emitted radiation, which is characteristic to each element. The peak amplitude in the XRF spectrum is proportional to the concentration of the corresponding elements in the sediment's analyzed square area.

Avaatech XRF Core Scanner III (super slit) measures the suite of elements between Magnesium (Mg) and Barium (Ba). Major and selected trace element data points were collected

every 1 cm down-core with a down-core slit size of 10 by 12 mm using generator settings 10 kV (Mg, Al, Si, P, S, Cl, K, Ca, Ti, Cr, Mn, Fe, and Rh), 30 kV (Ni, Cu, Zn, Ga, Br, Rb, Sr, Zr, Nb, Mo, Ru, Rh, Pb, and Bi), and 50 kV (Br, Rb, Sr, Zr, Mo, Ag, Cd, Sn, Te, Ba, and Pb). The tube currents were set to 50, 200, and 200 μA, with no filter for 10 kV, the Pd – Thick filter, and the 5 – Cu filter, respectively. Sampling time was set to 5 seconds for 10 kV and 10 seconds for 30 kV and 50 kV, and took place on the archived half of the core sections. 10 kV standards were used at a 50 mm step size, 220 mm in length, and run at the start and end of each lab day. Raw data was exported directly to Excel using WinAxelBatch, and processed using Excel, where the meters below sea floor depth was manually inputted into the sheet to correlate with the cm-interval data points.

Excel was used to sort and correct sample counts determined by the XRF core scanning methods with the M0064D depth from the IODP Expedition 347 report (Andrén et al., 2013). The counts at the ends of each core section were compared to the count concentrations above to see if there was an abrupt drop in elemental counts. If the counts were not within range of the last mode of the data, then the data point was omitted, as the instrument likely took a measurement of air. Coarse grained material and ice-rafted detritus was skipped or omitted due to the scanner's inability to accurately measure air space from porous and/or poorly sorted material.

2.4 Laminae Counts

Varve counting is useful for understanding the annual time scale and deglaciation speed within a proglacial lake setting, where more thin laminae originate from a distal source, and thicker varves have a more proximal provenance. Manual varve counting took place with four graduate students using high-resolution core images printed on poster-size paper. The Corelyzer software program is a visualization tool that enables high-resolution, scaled viewing of sediment cores. This program was also used to manually count the laminae in the varve sequence. Varve deposit counts add to the understanding of deglaciation speed at a higher resolution.

3. Results

3.1 Particle Size Results

Particle sizes were determined by the laser particle size analyzer, and then classified by size, sorting, and distribution using GRADISTAT (Blott and Pye, 2001) and Excel. Samples were differentiated and plotted by Unit and IODP Expedition 347 Hole M0064D depth, and by silt and clay couplets within the red and grey varve sequences. Using Excel, sand, silt and clay percentages were also plotted down core to show changing paleoenvironmental glacial settings, and followed the Udden-Wentworth scale.

Grain size distributions of all 53 samples plotted on the Folk-Ward sand-silt-clay ternary diagram (Figure 9) show that sediments were mostly sandy silt, with some silts and muds, and few silty sands. Sandy silts and silty sands were typical of diamictite matrix, while silts and muds were from alternating rhythmites in the varve sequence.

Unit IIIa (1.75 – 7.87mbsf), represented by 12 samples, is composed of mud and very fine to coarse silt, with few grains (< 2 vol. % frequency) in the fine sand fraction (7.78 and 7.85 mbsf) and is poorly sorted (Figure 10). 7.2 mbsf contained the highest frequency of grains (17 vol %) as coarse clay (3.9 μm), and 7.78 mbsf has the highest frequency (16.9 vol. %) of the finest grains, 0.98 μm, even with the small frequency (1.5 vol. %) of coarse silt (44.2 μm) particles in the sample, which is near the bottom of the unit. Another low frequency (1.9 vol. %) mode in the coarser silt fraction at 7.85 mbsf is visible (Figure 10).

Unit IIIb (7.87 – 9.3 mbsf), comprised of 11 samples, consists of mud and very fine to coarse silt, and a very low frequency (< 1 vol. %) of very fine sand grains (Figure 11). This unit is poorly sorted, and demonstrates a bimodal distribution, samples 7.91, 8.12, 8.22, and 8.41 mbsf are in the mud fraction, and samples 7.92, 8.13, 8.22, 8.42, and 9.2 mbsf contain very fine to fine silt (Figure 11). Samples 8.91 and 9.2 mbsf are more bulk samples, where 8.91 mbsf is platykurtic, and has the highest frequency (13.2 vol. %) of the silt material (7.8 μm). 9.2 mbsf

bulk sample is more silty, with 2.7 μm being the highest grain frequency (13.7 vol. %) (Figure 11).

Unit IVa, 9.3 – 25.4 mbsf, contains 23 samples measured by particle size, is very poorly sorted, ranging in mud, silt, and sand size fractions (Figure 12). It is predominately silty-sands and sandy-silts, and widely distributed. This unit is trimodal as it has a small mode in fine-medium sand (250 μm), between two larger modes around the fine silt (8 μm) and coarse sand (1000 μm) fractions (Figure 12). The fine silt mode varies in frequency from 5.9 vol. % (Sample 13.39) to 10 vol. % (Sample 17). The frequency range is much larger in the coarse sand mode, from 0.77 vol. % to 11.8 vol. %, respectively (Figure 12). A sandy mud with very coarse sandy medium silt (Sample 9.41) exhibits an outlier trend more towards the top of the unit, cutting across the data and having the least silt frequency (3.9 vol. %), and the greatest grain frequency (4.5 vol. %) in the fine-medium sand bin.

Unit IVb, 25.4 – 41.2 mbsf, 7 samples, is predominantly a silty-sand, sandy-silt unit that is very poorly sorted (Figure 13). This trimodal unit has modes in fine silt, fine-medium sand, and coarse sand. Frequency in the fine silt mode (8 μm) ranges from 4.9 vol. % (Sample 33.78) and 7.88 vol. % (Sample 25.7), where 33.78 is closer to the bottom of the unit, and 25.7 is at the uppermost part of unit IVb. The frequencies decrease in the more coarsely skewed material, except for sample 33.78, where the coarse sand grains (1000 μm) have a 9.9 vol. % frequency, the highest in the unit (Figure 13).

Sand, silt and clay percentages down core are shown in Figure 14, where Unit IVb consists of 30% – 50% sand (orange), and 30% - 50% silt (blue), opposing one another, and clay (green) sits around 20% abundance. Unit IVa, 25.4 mbsf, only contains samples further up section, between 18 and 9.41 mbsf. The start of this data trend is visible halfway through Unit IVa, where there's an increase in silt and clay, and a decrease in sand at 17.64 mbsf (Figure 14). Sand content steadily fluctuates with silt and clay, as silt and clay follow similar trends, synchronously increasing and decreasing. Unit IIIb transitions to a near zero percent sand, and jumps in clay

abundance, a core maximum of 89.5% at 8.41 mbsf. Unit IIIa contains high clay abundances with alternating high silt abundances, and < 1% sand abundance. Clay ranges from 52% - 88% abundance, and silt 10% - 46% abundance (Figure 14).

Particle size distributions of the Unit IIIa and Unit IIIb varve sections and the brown layer at the base of Unit IIIa (7.84 – 7.87 mbsf) are shown in Figure 15. Red varves in Unit IIIa alternate in layers of silt and clay/mud; a bimodal distribution. Coarse clay is the highest frequency grain (3.9 μm) at 17.3 vol. % abundance. Other fine silts sizes have 14.3 and 13.7 vol. % frequencies, respectively, while clays in this unit float around 15 vol. % frequency (Figure 15). The brown layer at the base of Unit IIIa is clay-rich, samples ranging from 12.3 – 13.9 vol. % frequency. Unit IIIb's grey varve sequence exemplified a bimodal grain size distribution, with a fine silt mode and a clay mode. Fine silt peaks at 17.6 vol. % frequency, and the clay mode peaks at 16.2 vol. % frequency (Figure 15).

Unit IIIa and IIIb were found to have a rhythmically laminated varve sequence based on the grain size percentages of alternating silt, and very fine silt to mud. Units IVa and IVb had results typical of a diamict matrix, with increased frequency of coarser grains, within the realm of sandy-silt and silty-sand.

3.2 ICP-OES and ICP-MS Results

Raw data was corrected and sorted using Excel. Using the normalized weight percent values, Manganese, Zirconium, and Titanium were normalized with Aluminum to account for the detrital fraction within the sediments, and remove any grain size biases that may occur with the geochemistry of the material (McLennan et al., 1993). Al_2O_3/TiO_2 ratios were plotted to determine if there was a change in provenance up core (Young and Nesbitt, 1998). Mn/Al ratios were plotted to show any changes in redox conditions of the bottom-water, and if chemical changes occurred across color transitions (Calvert and Penderson, 1993), especially between Unit

IIIa and Unit IIIb. Meltwater flux changes were plotted using Zr/Al ratios (Martinez-Ruiz et al., 2015).

The method and data used for each element is indicated in Table 4. Total Organic Carbon (TOC) in wt. % is also plotted using the shipboard data (Andrén et al., 2013). The spider diagram using ICP-MS rare earth element data and Upper Crust (McLennan, 2001) was plotted to check for elemental enrichments and/or depletions, and for provenance areas. Felsic, mafic, and recycling source areas of sediments are determined by Th/Sc versus Zr/Sc ratios (McLennan et al., 1993).

Enrichments factors of Rare Earth Elements (REEs) in ppm compared to the Earth's upper crustal values from McLennan (2001) are graphed in Figure 16, where any element with a ratio value greater than one is enriched, and an enrichment factor less than one is depleted. REEs are listed in order from left to right by atomic number, starting with La and ending with Yb. Gd is included in the data, but is not analyzed. Results show all samples in Unit IIIa (orange) and Unit IIIb (blue) are enriched in all REEs, and Unit IVa (yellow) and IVb (purple) follow a similar trend, but are mostly depleted in the REEs (Figure 16). This depth dependent enrichment factors pattern is largely driven by grain size. Sample 16.6 in Unit IVa rides the sample ppm/ppm upper crust ratio of one, where it's less depleted in the REEs at the atomic number boundaries, but enriched in Sm, Eu, Tb, and Dy. A slight decrease in the Ce enrichment is seen in the red varves of Unit IIIa, and the muds of Unit IIIb.

Th/Sc and Zr/Sc ratios (ppm) of Unit IIIa, Unit IIIb, Unit IVa and Unit IVb are graphed in Figure 17 along with the upper crust ratio from McLennan (2001). Zirconium is useful because it's found to be more abundant in felsic rocks. Thorium and Scandium are reliable source rock indicators because they are largely insoluble and are transported in the detrital fraction of terrigenous material (McLennan, 1993; Potter et al., 2005). Therefore, using Th/Sc and Zr/Sc ratios can yield mafic to felsic source rock variations, and show recycled sediment with added Zr (Potter et al., 2005). Units IIIa, IVa, and IVb all plot around the average upper crust, clustered

near 10 ppm Zr/Sc, and 1 ppm of Th/Sc (Figure 17). Unit IIIb, however, plots one order of magnitude larger on the Th/Sc ratio, and one order of magnitude smaller on the Zr/Sc ratio (Figure 17). Unit IIIb is therefore enriched in Th, and Zr depleted.

Al_2O_3/TiO_2 ratios, Mn/Al ratios, Zr/Al ratios and TOC (wt. %), are graphed down core (Figure 18) for all 18 samples using ICP-OES data. Al/Ti ratios of higher values are typically associated with felsic source material, while lower Al/Ti ratios, due to the increase in Ti, are indicators of a mafic source (Young and Nesbitt, 1998). The only sample in Unit IVb at 32.83 mbsf sits at 20.46 Al/Ti, and the seven samples in Unit IVa have an average Al/Ti ratio of 21.13, with the highest standard deviation of 0.85 at 10.2 mbsf (Figure 18). Samples in Unit IVa steadily float around the 21 value. Units IIIa and IIIb consist of larger Al/Ti value variations, where Unit IIIb ranges from 20.28 to 23.62 and Unit IIIa ranges from 19.92 to 25.72 (Figure 18).

Mn/Al ratios steadily increase up core to a maximum of 0.0151 at 14.2 mbsf, then decrease to an average of 0.00635 in Units IIIa and IIIb (Figure 18). Unit IVb Mn/Al ratio at 32.83 mbsf is 0.0066, while the average of Unit IVa is 0.0115 Mn/Al. Unit IIIb has a range of 0.0060 to 0.0079, and Unit IIIa ranges from 0.0054 to 0.0069 Mn/Al (Figure 18). Zr/Al ratios in Unit IVb is 0.0033, compared to Unit IVa's 0.0031 average wt. %. Zr/Al ratios decrease in Units IIIb and IIIa, falling to an average 0.0014 Zr/Al (Figure 13). TOC levels are between 0 and 0.5 wt. % throughout the core, however a 1.75 wt. % spike in TOC is present at the base of Unit IIIa within the brown layer, at 7.85 mbsf (Figure 18).

A zoom-in of the shaded region in Figure 18 (8.5 – 7.0 mbsf) is shown in Figure 19 across the Unit IIIb and Unit IIIa color transition. Al/Ti ratios tend to fluctuate with the silt and clay couplets, but peak in the brown layer. The silt layer has the lower ratio, while the mud layer in the couplet has the higher ratio. Mn/Al ratios also fluctuate with the silt and clay couplets, but decrease in the brown layer. Silt samples have a higher Mn/Al ratio and mud samples exhibit a lower ratio. Zr/Al ratios tend to be lowest in the mud fraction, but do not trend with the varve

couplets as well as the Al/Ti and Mn/Al ratios. The Zr/Al ratio however, abruptly decreases in the brown layer. The drastic increase in TOC (1.75 wt. %) is also exhibited in Figure 19.

3.3 XRF Core Scanning Results

A total of 9.65 meters of core was scanned from sections 64D-2H-1 to 64D-5H-1, consisting of Units IIIa, IIIb, and the top of Unit IVa. An overview of significant measured elements, Fe, Ca, Mn, and S are recorded here. Ratio counts of Al/Ti, Mn/Al, and Zr/Al are plotted 13.59 – 2.21 mbsf, and across section 10 – 8.8 mbsf, and 8.4 - 7 mbsf. The interval between 10 and 8.8 mbsf is examined more closely due to the dramatic increase in Zr, and 8.4 – 7 mbsf is focused on at 1 cm intervals due to the transition from grey thinly laminated rhythmites (Unit IIIb), to the dramatic dark-brown clay-rich layer and it's abrupt transition to red-brown varves (Unit IIIa).

Up core in Unit IVa, Fe ranges in counts from ~25,000 – 44,000, 13.59 – 9.42 mbsf, and then jumps up to 65,881 at the Unit IVa and Unit IIIb transition, 9.31 mbsf (Figure 20). Counts stay at this increased point, fluctuating in Unit IIIb between ~40,000 and 80,000. Ca opposes the Fe trend, where it makes a slightly more stepwise decrease in counts around the Unit IVa and Unit IIIb boundary, 9.31 mbsf, and is more variable (Figure 20). Mn shows a notable increase at this Unit transition in the core, where below 9.32 mbsf, the counts hover around 700, then spike up to 1069 (Figure 21). Mn shows more elevated count levels in the reddish-brown mud of Unit IIIa, exhibiting a more spiky appearance. Sulfur additionally has a change in trend at the top of Unit IVa, 9.41 mbsf, where counts decrease to below 1,000. Sulfur counts stay relatively low in Units IIIb and IIIa, besides a single spike in the brown layer and at the base of Unit IIIa (7.8 mbsf) of 1518 counts (Figure 21).

Al/Ti ratios show the largest variation at the lithological transition from silty sands and IRD to more silts and clays in Unit IVa and into Unit IIIb, between 13.59 - 8.81 mbsf, with count values between 0.326 and 0.984. The Al/Ti trend increases in the grey rhythmites of Unit IIIb,

and becomes more concentrated in the middle and uppermost parts of the Unit, between 9 and 8 mbsf. In the reddish-brown mud of Unit IIIa Al/Ti ratios begin to decrease in counts with little variation, jumping to a lower and more narrow range of 0.624 and 0.945 between 8.61 and 3.74 mbsf. The uppermost part of Unit IIIa (3.68 – 2.21 mbsf) has a stepped decrease in Al/Ti ratio values from 0.465 - 0.783 (Figure 22). ICP-OES data in the 8.5 – 7.0 mbsf across the Unit IIIb and Unit IIIa transition has a wider range than the XRF data exhibits.

Mn/Al ratios are relatively low in Unit IVa (between 0.164 and 0.339), until they spike in the top of the unit, from 0.557 counts to 0.666 from 11.39 - 9.7 mbsf. Mn/Al tends to steadily decrease in the grey rhythmites of Unit IIIb, and becomes progressively more spiky into the reddish-brown mud of Unit IIIa (Figure 23). ICP-OES data points plotted with XRF matches the high-resolution data relatively well, where 16 of the 19 data points fall on the straight-marked scatter plot.

Zr/Al ratios range from 0.599 to 1.29, in Unit IVa, and exhibit a sharp increase of 1.62 in Unit IVa at 11.41 mbsf (Figure 24). In the uppermost part of Unit IVa, Zr/Al begins to increase, and steps up to 3.30 from 9.84 to 9.44 mbsf. The Zr/Al ratio decreases abruptly at the lithological boundary of the diamict and the overlying grey rhythmites in the Unit IVa to Unit IIIb transition, and in the reddish-brown mud of Unit IIIa the ratio stays relatively low, ranging from 0.294 to 0.539. The trend becomes more variable up core in Unit IIIa. All but one ICP-OES data point falls on the XRF data series plot of Zr/Al. This abrupt increase in Zr/Al, along with the Mn/Al and Al/Ti ratios are compared to the grain size distribution 6 – 10 mbsf in Figure 25, where sand decreases from ~24.5 – 15 vol. %, 9.91 – 9.41 mbsf, and increases from ~15 % to 67 %, 9.41 to 9.2 mbsf.

A closer look at the greater Zr/Al ratio count values up core in Unit IVa along with a correlating core image is shown in Figure 20. This core section contains a range of silt to sand grain sizes, as well as grey, red and brown sediment color changes. Skipped XRF sections due to porous material, holes or IRD include: 10 – 9.96 mbsf, 9.87 – 9.82 mbsf, 9.71 – 9.67 mbsf, and

9.60 – 9.53 mbsf. Zr/Al ratios and Al/Ti ratios mirror one another, where Zr/Al increases in counts and Al/Ti decreases, and vice versa (Figure 26). Mn/Al ratios tend to increase when Zr/Al increases, and decrease as well, also doing the opposite of Al/Ti. The second largest spike in Zr/Al in Unit IVa at 9.69 mbsf corresponds to the small grey sediment lens above the white IRD (Figure 26). The largest Zr/Al peak in Unit IVa at 9.41 mbsf corresponds to the dark grey sandy sediment between the two IRD in the middle of the section image. Unit IIIb ceases to have these Zr/Al spikes, but the Al/Ti and Mn/Al ratios continue to be on the same magnitude of counts (Figure 26).

These ratios were also plotted across the color change and Unit IIIb - IIIa transition, 8.4 – 7 mbsf (Figure 27). Results show the Al/Ti, Mn/Al, and Zr/Al counts were spiky across the section, and across the color change. Al/Ti and Mn/Al ratio counts decreased in the brown later (7.87 – 7.85 mbsf), while Zr/Al ratio counts increased. A noticeable increase in Mn/Al ratio counts is exhibited in Unit IIIa around 7.1 mbsf, where counts double (Figure 27). It seem that the color change is not being strongly driven by these chemical scenarios.

Sulfur counts notably increased in at the base of Unit IIIa, as explained above, and are plotted across the transition from Unit IIIb to Unit IIIa in Figure 28. Results show a spiky sulfur count, with almost a 4-fold increase in Sulfur counts in the brown layer (Figure 28). Two points extend to 1517 and 1518 total counts at 7.87 and 7.86 mbsf, respectively. These increased sulfur counts at the base of Unit IIIa correlate to the brown layer containing >1.5 wt. % TOC, and further support the existing organic content within the sediment.

3.4 Laminae Counts

Varve counting on poster-size paper by four graduate students revealed an average of 72 varve couplets from the start to the end of the visible varve sequence, 8.8 – 6 mbsf in M0064D, yielding an average sedimentation rate of 3.89 cm/yr. These varve counts start within the uppermost portion of Unit IIIb, at the start of the grey varve sequence, and continue through the

color transition into Unit IIIa, where faint red-brown varves were also counted until they were no longer visible.

4. Discussion

4.1 Diamicton Provenance

Two differing glacial till units in the sedimentary sequence have been identified, and their potential source rock and timing of deposition is still largely under investigation. Unit IVa consists of a more stratified, muddy diamicton that is grey at the base and red-lensed in the upper portion. Unit IVb is a more matrix-supported and clast-poor sandy diamicton, likely representing a subglacial paleoenvironment with occasional alignment shear fabrics. Based on literature discussing the origin of differing glacial tills in the southwestern Baltic Sea region, Kattegat, southern Skåne, and Denmark, lithological provenance interpretations can be made about these two diamictons, and their potential subglacial depositional timing.

Average Al/Ti ratios of these two units are relatively close to the upper crustal value of 19.61 (McLennan, 2001), where Unit IVa sustains an average value of 21.22 and Unit IVb has a 20.85 Al/Ti ratio, indicating a more felsic source for both. Figure 31 shows how these two Units are represented in a source rock variation trendline, where Unit IVa and IVb both lie in the recycled source category. Due to the poorly sorted, consolidated nature of these sediments, their deposition in a subglacial paleoenvironment is further supported by Figure 31.

The Late Weichselian glacial history of the SIS is not well constrained in the southwestern Baltic, and in parts of southernmost Sweden, like it is in Denmark (Anjar et al., 2014). Correlating diamicton stratigraphy in this region has also proven difficult, as there is limited availability of reliable age constraining proxies, leaving many speculative results (Anjar et al., 2014). Five Weichselian advances of the SIS have been identified in eastern Denmark that may potentially correlate to the two diamictons present in this study, contingent upon the age constraints and compositions of these tills (Sorensen et al., 2015, Houmark-Nielsen and Kjaer,

2003). In this case, an open-ended scenario is suggested here to explain the differences in glacial till at Site M0064. This scenario that explains subglacial till deposition and deformation suggests at least three different ice sheet advances.

The southwestern Baltic is said to have experienced a major SIS advance around 30 ka BP (Houmark-Nielsen and Kjaer, 2003, Andrén et al., 2011), which may correlate to the Unit IVb till seen in the core. In southernmost Skåne, sedimentary sequences at this age are recognized as the Klintholm advance, followed by a much smaller and shorter Allarp advance ~26 ka BP, then the LGM/Young Baltic advance, which experienced smaller readvances 19 - 18 ka BP and 17 – 18 ka BP (Anjar et al., 2014). Northern Denmark advances in the nearby region are known as the Kattegat advance, 29 -27 ka BP, and the Main advance, which is the LGM equivalent, ~20 ka BP (Anjar et al., 2014; Larsen et al., 2009). It's possible the Kattegat advance, reaching northern Denmark, also extended to Hanö Bay, but did not reach as far as southern Skåne (Figure 29), depositing the Kattegat Till in the Kattegat region, the till described in Unit IVb, ~29 – 27 ka BP. The Kattegat Till to the west demonstrates glaciotectonic deformation (Larsen et al., 2009), where these shear fabrics may be present due to the deposition of the lowermost portion of Unit IVa, a massive, poorly sorted grey diamicton.

The 20 ka BP Main advance, LGM, or Young Baltic advance, as it is regionally called, may correlate to the lower portion of Unit IVa, and could have caused the shear fabrics present in Unit IVb. The Kattegat Till is overlain by a till characterized by central and southern Swedish erratics and material of Fennoscandian province (Houmark-Nielsen, 2003). At the base of the unit it contains glaciotectonic structures, indicating the ice deformation from the northeast (Houmark-Nielsen, 1987). This northeast advance spread across Skåne and to Denmark, depositing material classified as the Mid Danish Till, age constrained to 23 – 21 ka BP (Larsen at al., 2009). It's possible this Mid Danish Till in northern Denmark may correlate to the lowermost part of Unit IVa at Hanö Bay ~ 20 ka BP, where this late Weichselian advance likely caused the shear fabrics present in Unit IVb.

Following the phase of the LGM ~20 ka BP, the SIS began its retreat, and Bornholm was exposed 16.6 ± 0.9 ka BP, along with parts of southwestern Sweden (Anjar, et al. 2014). A lobe within the Hanö Bay continued to override Site M0064 during a young Weichselian readvance, depositing the upper portion of Unit IVa, a red diamict with ice-contact outwash plain features, and glacial erratics of Baltic provenance (Van der Wateren, 1999). This red-lensed upper till was the last to be deposited in a subglacial environment in Hanö Bay, and thereafter the SIS rapidly retreated during the Bølling-Allerød interstadial period (~14.7 – 12.7 ka BP).

This scenario suggests the massive grey diamict with sheared fabric, Unit IVb, is part of the Kattegat advance, ~29 ka BP, and the lower portion of Unit IVa, a massive grey diamict, was deposited during the LGM, ~ 20 ka BP. A smaller readvance anywhere from 19 – 17 ka BP, possibly related to the SIS marginal lobe in Hanö Bay, deposited the red diamict.

Further research needs to be completed on the till sections of this core to better understand their compositions and potential source rock, and to determine their specific Baltic provenance. Little is known about the differences in these core sections, as data ~17 – 25 mbsf was not investigated due to no available samples in the lowermost parts of Unit IVa. Suggested further investigation includes identifying the fine gravel clasts within samples of each differing diamicton to determine their lithology and classify them into according lithological groups, e.g., crystalline rocks, quartz, limestone, chalk, fine sandstones and shales, etc. Determining these clast lithologies would adhere to identifying the source rock of the glacial till, and may allow for better correlation with tills in the surrounding SW Baltic Sea region.

4.2 Origin of Varve Color Transition

The grey varve sequence exhibited in the uppermost portion of Unit IIIb is truncated by a dark chocolate brown >1.5 wt. % TOC-rich clay layer, radiocarbon dated to 45,700 ± 1,500 cal yr BP (Andrén et al., 2015), marking the lower boundary of reddish-brown Unit IIIa and the dramatic color transition at 7.87 mbsf in Hole M0064D. Only ~2.5 cm thick, this dark brown

layer transitions upward into a faint reddish brown varve sequence. Based on physical and geochemical data from this research, and literature discussing the deglacial timeline of the SW Baltic Sea region, using numerous dating methods of glacial moraines and organic-rich deposits, an origin of this varve color transition can be investigated. A few possibilities may explain the color change in the sedimentary sequence. The color transition could be driven by grain size changes in the varve sequence, a saline ingression from the Atlantic Ocean, which altered the redox environment at the time of deposition, or a change in sediment provenance.

The low TOC content in the dark brown layer makes the radiocarbon age for this unit suspicious. Radiocarbon dating is limited to ~50,000 years BP, suggesting this layer consists of near-dead carbon. The glacial diamict in Unit IVa, indicative of a subglacial paleoenvironment, lies below the brown layer and the grey varves in Unit IIIb. This is the uppermost subglacial signature seen in M0064, as proglacial sediment, ice-rafted debris (IRD), and glaciolacustrine varves rest on top of this sequence in Units IIIb and IIIa, representing an ice marginal retreat, as the SIS was not present at the project site after this time. This subglacial diamicton to sedimentary sequence transition likely represents the deglacial process of the LGM, ~20 ka BP and younger. Therefore, the radiocarbon age of the brown layer up section is incompatible with the known deglaciation chronology. It is likely the carbon is recycled from older sediments, yielding the conflicting age. This explanation and the minor TOC content in the layer may support this hypothesis.

Particle size analysis across the color transition showed no change in grain size (Figure 15). The clay mineralogy recorded above and below the color change from grey to red varves demonstrate only slightly higher clay content up section, in Unit IIIa. The grey varves in Unit IIIb demonstrate two modes of clay and silt, representing the alternating silt and clay layers in an annual varve sequence. This sedimentary sequence represents a glaciolacustrine depositional paleoenvironment, where meltwater fluxes and more turbid lake waters in the summer bring silt to Hanö Bay, and much lower energy lake environments, where ice may be frozen over the lake

surface, allow for clay particle deposition in the winter. The brown layer exhibits a more clay-rich particle size, indicating a lower energy, deep lacustrine environment. The red varves in Unit IIIa also contains two particle size modes, one at clay and another at very fine silt. The varves in this section are fainter in comparison to the grey varves in Unit IIIb, and have a finer silt fraction in the summer months. Typically, thinner and finer varves indicate a more distal glacial margin. It's possible the glacial margin had retreated farther north during this time, over the course of the 72-year varve sequence.

Enrichment factors of the REE in Unit IIIa and IIIb show a drop in the Cerium enrichment across the color change (Figure 16). The clay layers of the grey varve couplets, as well as all of the red varve couplets demonstrate this drop in Ce by an average of 18.5% using upper crustal values from McLennan, 2001. Typically, Cerium is found in the 3+ valence state in river suspended load, and is oxidized to an insoluble 4+ valence state, which travels to the ocean and is present in seawater as a dissolved fraction (Piper and Bau, 2013). Seawater is presented as a negative anomaly in REE enrichment factors, which tends to become more negative with depth, representing suboxic to oxic redox conditions, and seawater alkalinity from which the 3+ to 4+ valence state accumulated (Piper and Bau, 2013). Heavier REE possess an increase in concentrations following the Ce anomaly, as they're less readily removed (Piper and Bau, 2013). Cerium concentrations in a study presented by Piper and Bau, 2013, show REE seawater curves from the Sargasso Sea of the Atlantic drop ~60% between 60 and 105 m depth using the World Shale Average (WSA). This drop in Ce is three times greater than the drop exhibited at Site M0064.

When applying the WSA (Piper and Bau, 2013) to the M0064 REE in ppm, a Cerium depletion is not present, and heavier REE demonstrate a decreasing trend as opposed to an increasing trend (Figure 30). This enrichment trend with no drop in Cerium indicates there was no saline influx into the Baltic Sea basin across the color change, and within Units IIIb and IIIa. Therefore, a marine incursion into the southwestern Baltic likely did not occur until sometime

after the deposition of the reddish-brown mud, and this color transition must be older than the first brackish phase of the Yoldia Sea, 10,540 years BP. There is no evidence of brackish water present in the BIL at this time.

The change in color must then result from a change in the chemical composition in the sediment due to a redox change in the water column, denoted by Mn/Al ratios, or a provenance change, seen with Al/Ti ratios. The physical particle size measurements, as stated above, do not correlate the color transition to any major grain size change in the sedimentary sequence, and there is not a Ce depletion indicative of a marine incursion across the color change. Al/Ti, Mn/Al, and Zr/Al ratios show relatively minor changes in the data in comparison to the dramatic color change seen in the core at ~7.85 mbsf.

Manganese behaves differently under oxic and anoxic bottom water conditions, where the valence state changes upon the redox potential across a water column or sea-floor redox boundary (Calvert and Penderson, 2007). Mn becomes a highly insoluble oxide under oxic marine conditions, while under anoxic conditions, Mn accumulates in the dissolved load of the bottom water due to Mn(IV) oxide reduction (Calvert and Penderson, 2007, Calvert and Penderson, 1993). Mn reduction in anoxic to sub-oxic conditions is defined as Mn (II) while Mn oxidation is the Mn (IV) state (Burdige, 1993). There is no direct role of biota affecting the potential reducing/oxidizing conditions at the time of deposition at Site M0064 due to the detrital make-up of the sediments. It's likely that manganese oxides are coatings on the detrital sediments in this scenario. Mn will become mobile in the water column under anoxic bottom water conditions, causing a depletion of Mn in sediments (Calvert and Penderson, 1993).

Across the color transition, Mn/Al ratios experience minor changes that likely do not indicate a remarkable redox change within the water column. The average Mn/Al value of Unit IIIb is 0.0069 dropping to 0.0061 in the brown layer, followed by a further decrease to 0.0060 average Mn/Al in the red varves of Unit IIIa (Figure 19). Compared to McLennan, 2001's upper crustal value of 0.0075, the lower Mn/Al ratios likely suggest reducing conditions in the water

column at the time of deposition. It's possible that the average decrease from 0.0069 to 0.0061 across the grey varve to brown layer transition may indicate a slightly less oxic paleoenvironment, and the conditions in Hanö Bay are still reducing.

Mn spikes however, are seen further up section in Unit IIIa, above around 6.5 mbsf (Figure 23). These spikes may potentially correlate to a marine incursion of the brackish phase mentioned by Andrén et al., 2002, 10,450 yr BP, as suggested that Mn spikes correspond to prevailing oxic bottom water conditions. A marine ingression would bring highly saline, oxic waters to the Baltic bottom water, causing Mn to become highly insoluble. If this is true, then the color transition in the varve sequence must be older than the first brackish phase of the Baltic. It's possible this color change may correspond to the lithologic color change described in southern Sweden by Björck et al., 1996, which marks the transition from the YD phase to the Preboreal warming of the Yoldia Sea, ~11,450 to 11,390 ± 80 yr BP.

Zirconium mirrors quartz in that is highly chemically resistant, surviving recycling and accumulating in soils, and has a similar hardness (Calvert and Penderson, 2007). With a specific gravity of 6.5 g/cm^3, Zr is transported in the coarser terrigenous fraction, with fine-medium quartz grains (Calvert and Penderson, 2007), heavy minerals, and medium to coarse silts (Muschitiello et al., 2016) and therefore can be representative of higher energy depositional environments. Average Zr/Al ratios in ppm across the color transition show minor changes. Grey varves have an average Zr/Al ratio of 0.074 ppm, a decrease to 0.068 ppm in the brown layer, and an increase to 0.073 ppm in the red varves. It's possible the lower Zr/Al ratio is a result of the lesser silt content in the brown layer, as Zr is more readily transported in the silts and fine sands, as stated above. This minor change across the color transition is likely not pronounced enough to denote the color change to a change in meltwater discharge, as the brown layer consists of lower Zr/Al values and as is expected for a clay-rich interval.

Although no large spikes in Zr/Al ratios are seen across the color change, there is a drastic increase in Zr/Al 9.8 – 9.3 mbsf, at the uppermost part of diamicton Unit IVa (Figure 24,

25 and 26). These sandy silt sediments with few IRD likely represent an ice-proximal, proglacial environment, where the SIS was largely influencing the project site with meltwater pulses. This distinct spike in Zr/Al ~9.41 mbsf may be grain size driven, as a 50 vol. % increase in sand is exhibited across this interval (Figure 25). It's possible, however, these meltwater pulses could be a representation of the the Bølling-Allerød warming (~14.7 – 12.7 ka BP), where the SIS was rapidly retreating to the north and releasing meltwater surges that deposited coarse material in Hanö Bay. Another scenario to consider, is if these large Zr/Al spikes correlate to the drainage of the once-dammed BIL, however there are no varves present in the sedimentary sequence below the Zr/Al spikes that correlate to the fine-medium sands and coarse IRD.

The Al/Ti signature across the color change does not show a dramatic shift that evidently proves a provenance change in the sediment. However, Th-enrichment in Unit IIIb's grey varves may support a source change in the sediment that explains the shift in color at ~7.85 mbsf. The Al/Ti ratio experiences its largest jump in ICP data across the color change, from 20.50 to 25.72 (Figure 19). This wider range is not seen in the XRF data, where ratio counts across the color change in fact decrease (Figure 27). The average Al/Ti upper crustal value from McLennan, 2001 is 19.61, which is relatively close to the average Al/Ti ratio in Unit IIIb, 21.98. The brown layer holds an average Al/Ti ratio value of 23.02, and the red varves in Unit IIIa have an average value of 22.67. Based on the average values, there does not seem to be an intense source change between deposition of the grey varves and the reddish-brown mud.

Individual varve couplets vary in ratio value, with clay ratios ~23 and silt ratios having a lower Al/Ti value, at ~19 - 20. The abrupt jump to ~26 for the Al/Ti ratio in the brown layer suggests a slightly more felsic source change within the brown layer, the highest Al/Ti ratio in the sedimentary sequence. Again, the Al/Ti values decrease within the red varves deposited above the brown layer, down to 19.92 at the bottom most silt layer, and 23.83 in the clay layer. It's possible that the silt layers of the varve couplets have lower Al/Ti values due to grain-size effects (Young and Nesbitt, 1998).

The grey varve sequence below the color change exhibits a Th-enrichment and Zr-depletion that plots unusually out of character for mafic, felsic, and recycled rocks (Figure 31). The source rock variation trendline from McLennan et al. (1993) shows the category where each unit resides. Figure 31 indicates material at Site M0064 is not of mafic source, but Unit IIIa, the red varves, reveal a sediment recycling and/or felsic variation. The average upper crustal value represents more recycled sediment, and the Unit IVb and IVa diamicts reside in the sediment recycling section due to the greater Zr abundance.

The grey varved clay of Unit IIIb, however, is notably higher in Thorium than the reddish-brown mud of Unit IIIa, and lower in Zr, both by a factor of ten. This highly unrecycled and Th-rich grey varve sediment is thought to have originated from a differing source than the red varves further up core. A Scandinavian locality known as the Oslo igneous province in southeastern Norway is known to be enriched in Thorium (Bonin and Sorensen, 2003, Killeen and Heier, 1975). Fairly high Thorium values are also found in the overburden till of central and south central Sweden, made up of the underlying bedrock (Thunholm et al., 2005). Th-rich material is also found in plutonic rocks (1850 – 1660 Ma) in southernmost Sweden, off the coast of Hanö Bay (Lahtinen, 2012; Thunholm et al., 2005). These regions could be a potential source of the grey varves, and a possible explanation to the color change from grey to red in the varve sequence. The red varves did not originate from this source, as there is no Th-enrichment, but potentially the Esrum/Alnarp valley arkosic sandstones, mudstones, and coal basin deposits from the Late Triassic – Jurassic, which have been notably reworked, as mentioned by Ahlberg et al., 2002. This paleovalley is also known to have older radiocarbon dated sediments of organic-rich materal >35 ka BP (Andrén et al., 2011; Houmark-Nielsen and Kjaer, 2003). The coal seams present in the Esrum/Alnarp paleovalley may be the tapped source that yields the older organics in the brown layer, and the red beds may be the source of the red varves. The reworking of this sediment may also explain why this unit plots in the felsic/recycled signature in Figure 31, and why the Al/Ti ratio does not dramatically change across the color transition. It's possible the

Esrum/Alnarp valley is also a source to the Zr/Al spike seen below the varve sequence, where Zr is linked to coarser material, and may have deposited the red lensed material in the Hanö Bay.

The dramatic color transition from grey, to brown, to red in the varve sequence yields no link to grain size shifts (Figure 15), and changes in redox sensitive elements (Figure 27). Zr/Al ratios in XRF and ICP data do not show a relative spike in the data to indicate a meltwater pulse, and Mn/Al ratios are not altering to support changing redox conditions in the water column at the stratigraphic level of the color transition from grey to reddish brown (Figure 27). There are no indicators in the sedimentary record at the color change transition that support a saline water ingression, as there is no Ce anomaly and the redox conditions were reducing, therefore, a marine incursion is unlikely to be the cause of the color change (Figure 30). Al/Ti ratios are not drastically changing in the XRF data, however ICP data yields a wider Al/Ti range, which may support a change in provenance. The possibility of a provenance shift from a Th-enriched province of southeastern Norway or central Swedish terranes to sandstones, red beds, mudstones and coal seams, may not be evidently shown in the Al/Ti ratios because Al/Ti ratio variability is best exhibited in igneous rocks (Young and Nesbitt, 1998). This may be the explanation for little change in the Al/Ti signature in the chemical data, while the sediment source is changing, and is supported by the Th-enrichment in Unit IIIb's grey varves, it is not changing from two igneous sources.

It's possible a sedimentary signature from the catastrophic BIL drainage is not seen at Site M0064, since the main drainage passage was in south central Sweden, north of Mt. Billingen, ~800 km away. A 10 - 25 m drop in lake level may not have affected the redox conditions in Hanö Bay, as the environment was still reducing across the color change, however the BIL level drop 12,867 ± 66 cal. years BP (Muschitiello et al., 2016) could have caused SIS meltwater to alter its course, causing the provenance change seen in the data, matching with the color change. Therefore, it's plausible to consider that the color change is exhibited by a source shifting of material due to the draining of the BIL. Another scenario to potentially associate with the color

variation is the transition from the YD to the Preboreal freshwater phase in the Yoldia Sea. The sedimentary signature is a source change from Th-rich material of southeastern Norway or south central Sweden, to Jurassic sedimentary red beds and coal seams of southern Sweden. Nonetheless, we would expect to find varve deposition during the BIL phase of the Baltic Sea, which is why retrieving a reliable age within the core is essential.

5. Conclusions

By completing particle size and high resolution geochemical analysis of IODP Core M0064D, located in the southwestern Baltic Sea, and pairing these analyses with previous literature on the Baltic Sea basin, conclusions can be made about the relative timing of SIS deglaciation, and the drainage of the BIL (Figure 32). First, Hanö Bay experienced at least two to three glacial advances to deposit the diamicts within the core. Unit IVb's grey glacial till with glaciotectonites was deposited ~29-27 ka BP, and the lowermost portion of Unit IVa is a remnant of the LGM ~20 ka BP, where this advance caused the tectonic fabric seen in Unit IVb. A SIS lobe within Hanö Bay between ~18-16 ka BP, possibly related to the Heinrich I stadial period, could have deposited the uppermost red-lensed till in Unit IVa, and implemented shear fabrics in the lower portion of Unit IVa. By ~16 ka BP, Hanö Bay transitioned to an ice-proximal, proglacial paleoenvironment, where diamicton is no longer present in the core, ~9.3 mbsf, as denoted by the decrease in sand and poorly sorted, consolidated material.

The rapid retreat of the SIS may be exhibited in the sediment core by the Zr/Al spike (Figure 24, 25, and 26), as Zirconium tends to be concentrated in fine-medium sands. The red lensed sediment in the sequence may correlate to the same source of the red varves, the Esrum/Alnarp valley's Jurassic arkosic sandstones in southern Sweden. Color changes in the sedimentary sequence do not coincide with grain size shifts, indicating the dramatic color change is not associated with a change in depositional environment. The > 1.5 wt. % TOC increase within the brown layer may explain a shift in color, suggesting a provenance change from a Th-rich source in the Norwegian Oslo province or in south central Sweden, to a Jurassic-aged tapped

source of the Esrum/Alnarp paleovalley, which contains reworked sandstone and mudstone red beds with coal seams. It's possible this color transition correlates to the same transition discussed by Björck et al., 1996, where the YD transitions to the Yoldia Sea Preboreal warming phase, ~11,450 to 11,390 ± 80 yr BP, and the onset of the brackish stage, 10,540 yr BP, correlates to Mn/Al spikes up core in the XRF data. Andrén et al., 2002 suggests a color change is exhibited prior to an influx of saline waters, which matches accordingly with the sedimentary sequence at M0064.

The highly complex southwestern Baltic Sea has proven to be a dynamic paleoenvironment, at least 20 – 11 ka BP. The paleoenvironmental conditions in Hanö Bay are influenced by the waxing and waning of the SIS, meltwater pulses, and isostatic rebound in the southwestern Baltic. These factors cause relative sea level to be variable, and have allowed for freshwater to be released into the Atlantic with potential effects on the Atlantic Meridional Ocean Circulation (Toucanne, et al., 2015, Jakobsson et al., 2007, Larsen et al., 2009, Clark et al., 2012).

References:

Ahlberg A., Olsson, I., Šimkevicius, P. (2002). Triassic – Jurassic weathering and clay mineral dispersal in basement areas and sedimentary basins of southern Sweden. *Sedimentary Geology:* 161, 15-29.

Andrén et al., (2015). IODP expedition 347: Baltic Sea basin paleoenvironment and biosphere. *Sci. Dril.*: 20, 1-12.

Andrén, T., Jørgensen, B.B., Cotterill, C., Green, S., and the Expedition 347 Scientists (2013). *Proceedings of the Integrated Ocean Drilling Program,* vol 347.

Andrén, T., Lindeberg, G. & Andre´n, E. (2002). Evidence of the final drainage of the Baltic Ice Lake and the brackish phase of the Yoldia Sea in glacial varves from the Baltic Sea. *Boreas*: 31, 226-238.

Andrén, T., Björck, S., Andrén, E., Conley, D., Zillén, L., and Anjar, J. (2011). Chapter 4: The Development of the Baltic Sea Basin During the Last 130 ka. *The Baltic Sea Basin*, 75-97.

Anjar, J., Larsen, N. K., Håkansson, L., Möller, P., Linge, H., Fabel, D. & Xu, S. (2014). A ^{10}Be-based reconstruction of the last deglaciation in southern Sweden. *Boreas*, 43: 132–148.

Anjar, J., Adrielsson, L., Larsen, N. K., Möller, P. and Barth, K. (2014): Weichselian history of the Fennoscandian ice sheet in southern Sweden and the southwestern Baltic Basin. *Boreas*: 43, 608–626.

Bahr, A., F. J. Jiménez-Espejo, N. Kolasinac, P. Grunert, F. J. Hern andez- Molina, U. Ro€hl, A. H. L. Voelker, C. Escutia, D. A. V. Stow, D. Hodell, and C. A. Alvarez-Zarikian (2014). Deciphering bottom current velocity and paleoclimate signals from contourite deposits in the Gulf of Cádiz during the last 140 kyr: An inorganic geochemical approach, *Geochem. Geophys. Geosyst.,* pp. 1-16.

Björck, S. (1995). A Review of the History of the Baltic Sea, 13.0-8.0 ka BP. *Quaternary International:* 27, 19-40.

Björck, S., Kromer, B., Johnsen, S., Bennike, O., Hammarlund, D., Lemdahl, G., Possnert, G., Rasmussen, T.L., Wohlfarth, B., Hammer, C.U., and Spurk, M. (1996). Synchronized Terrestrial Atmospheric Deglacial Records Around the North Atlantic. *Science:* 274, 1155-1160.

Blott, S.J. and Pye, K. (2001) GRADISTAT: a grain size distribution and statistics package for the analysis of unconsolidated sediments. *Earth Surface Processes and Landforms:* 26, 1237-1248.

Bonin B. and Sorensen H. (2003). The granites of the Mykle region in the southern part of the Oslo igneous province, Norway. *Norges qeoloqiske undersekelse Bulletin:* 441, 17-24.

Burdige, D. (1993). The biogeochemistry of manganese and iron reduction in marine sediments. *Earth-Science Reviews*, 35 pp. 249-284.

Calvert S.E., and Penderson T.F. (2007). Elemental Proxies for Palaeoclimatic and

Palaeoceanographic Variability in Marine Sediments: Interpretation and Application. *Developments in Marine Geology*, 1: 567-644.

Calvert S.E., and Penderson T.F. (1993). Geochemistry of Recent oxic and anoxic marine sediments: Implications for the geological record. *Marine Geology*, 113: 67-88.

Clark, P., Shakun, J., Baker, P., Bartlein, P., Brewer, S., Brook, E., Carlson, A., Cheng, H., Kaufman, D., Liu, Z., Marchitto, T., Mix, A., Morrill, C., Otto-Bliesner, B., Pahnke, K., Russell, J., Whitlock, C., Adkins, J., Blois, J., Clark, J., Colman, S., Curry, W., Flower, B., He, F., Johnson, T., Lynch-Stieglitz, J., Markgaf, V., McManus, J., Mitrovica, J., Moreno, P., Williams, J. (2012). Global climate evolution during the last deglaciation. *PNAS Plus.* pp. 1-9.

Harff, J., Björck, S., and Hoth, P. (2011). Chapter 1: The Baltic Sea Basin: Introduction. *The Baltic Sea Basin:* 3-9.

Houmark-Nielsen, M. (2010) Extent, age and dynamics of Marine Isotope Stage 3 glaciations in the southwestern Baltic Basin. *Boreas*, 39: 343–359.

Houmark-Nielsen, M. and Kjær, K. H. (2003). Southwest Scandinavia, 40–15 ka BP: palaeogeography and environmental change. *Journal of Quaternary Science*, 18: 769–786.

Jakobsson, M., Svante, B., Alm, G., Andrén, T., Lindeberg, G., Svensson, N. (2007). Reconstructing the Younger Dryas ice dammed lake in the Baltic Basin: Bathymetry, area and volume. *Global and Planetary Change*, 57: 355-370.

Killeen P., and Heier, K. (1975). A uranium and thorium enriched province of the Fennoscandian shield in southern Norway*. *Geochimica et Cosmochimica Acta,* 39: 1515-1524.

Lahtinen, R. (2012). Main geological features of Fennoscandia. *Geological Survey of Finland, Special Paper: 53*, 13–18.

Larsen, N.K., Knudsen, K. L., Krohn, C. F., Kronborg, C., Murray, A. S. and Nielsen, O. B. (2009). Late Quaternary ice sheet, lake and sea history of southwest Scandinavia – a synthesis. *Boreas*, 38: 732–761.

Lenz, C., Behrends, T., Jilbert, T., Silveira, M., Slomp, C. (2014). Redox-dependent changes in manganese speciation in Baltic Sea sediments from the Holocene Thermal Maxiumum: An EXAFS, XANES, and LA-ICP-MS study. *Chemical Geology,* 370*:* 49-57.

McLennan, S. (2001). Relationships between the trace element composition of sedimentary rocks and upper continental crust, *Geochem. Geophys. Geosyst.,* 2: Paper number 2000FC000109.

McLennan, S. M., Hemming, S., McDaniel, D. K., and Hanson, G. N. (1993). Geochemical approaches to sedimentation, provenance, and tectonics, in Johnsson, M. J., and Basu, A., eds., Processes Controlling the Composition of Clastic Sediments. *Geological Society of America,* Special Paper 284.

Murray, R., Miller, D., and Kryc, K., (2000) Analysis of major and trace elements in rocks,

sediments, and interstitial waters by inductively coupled plasma–atomic emission spectrometry (ICP-AES)[1,2]. *ODP Technical Note,* 29: 1-27.

Muschitiello, F., Lea, J. M., Greenwood, S. L., Nick, F. M., Brunnberg, L., MacLeod, A. & Wohlfarth, B. 2016 (April): Timing of the first drainage of the Baltic Ice Lake synchronous with the onset of Greenland Stadial 1. *Boreas*, Vol. 45, pp. 322–334.

Nielsen, L.H. (2003). Late Triassic – Jurassic development of the Danish Basin and the Fennoscandian Border Zone, southern Scandinavia. Geological Survey of Denmark and Greenland Bulletin: 1, 459-526.

Potter, P.E., Maynard, J.B., and Depetris, P.J. (2005). Provenance of Mudstones. *Mud and Mudstones*, 157-174.

Pattan, J.N., Mir, I.A., Parthiban, G., Karapurkar, S.G., Matta, V.M., Naidu, P.D., Naqvi, S.W.A. (2013). Coupling between suboxic condition and southwest monsoon intensification in the western Bay of Bengal sediment core: a geochemical study. *Chemical Geology:* 343, 55-66.

Piper, D., and Bau, M. (2013). Normalized Rare Earth Elements in Water, Sediments, and Wine: Identifying Sources and Environmental Redox Conditions. *American Journal of Analytical Chemistry,* 4: 69-83.

Ridge, J.C., Balco, G., Bayless, R.L., Beck, C.C., Carter, L.B., Dean, J.L., Voytek, E.B., Wei, J.H. (2012). The New North American Varve Chronology: A Precise Record of Southeastern Laurentide Ice Sheet Deglaciation and Climate, 18.2-12.5 kyr BP, and Correlations with Greenland Ice Core Records. *American Journal of Science*: 312, 685-722.

Martinez-Ruiz, F., Kastner, M., Gallego-Torres, D., Rodrigo-Gámiz, M., Nieto-Moreno, V., Ortega-Huertas, M. (2015). Paleoclimate and paleoceanography over the past 20,000 yr in the Mediterranean Sea Basins as indicated by sediment elemental proxies. *Quaternary Science Reviews:* 107, 25-46,

Šliaupa, S., and Hoth., P. (2011). Chapter 2: Geological Evolution and Resources of the Baltic Sea Area from the Precambrian to the Quaternary. *The Baltic Sea Basin*, 13-45.

Sperazza, M., Moore J.N., Hendrix M.S. (2004). High-resolution particle size analysis of naturally occurring very fine-grained sediment through laser diffractometry. *Journal of Sedimentary Research,* 74: 736-743

Stroeven, A., et al. (2015) Deglaciation of Fennoscandia. *Quaternary Science Reviews*, pp. 1-31.

Thunholm, B., Lindén, A.H., Gustafsson, B. (2005). Concentrations of Uranium, Thorium and Potassium in Sweden. *SSI Rapport,* 4: 1-54.

Toucanne, S., et al. (2015) Millennial-scale fluctuations of the European Ice Sheet at the end of the last glacial, and their potential impact on global climate. *Quaternary Science Reviews,* vol. 123, pp. 113-133.

Van Der Wateren, F. (1999) Structural geology and sedimentology of the Heiligenhafen till section. *Northern Germany Quaternary Science Reviews,* vol. 18 pp. 1625-1639.

Young, G.M., and Nesbitt, H.W. (1998). Processes Controlling the Distribution of Ti and Al in Weathering Profiles, Siliciclastic Sediments and Sedimentary Rocks. *Journal of Sedimentary Research*: 68, 448-455.

Appendix

A. Figures

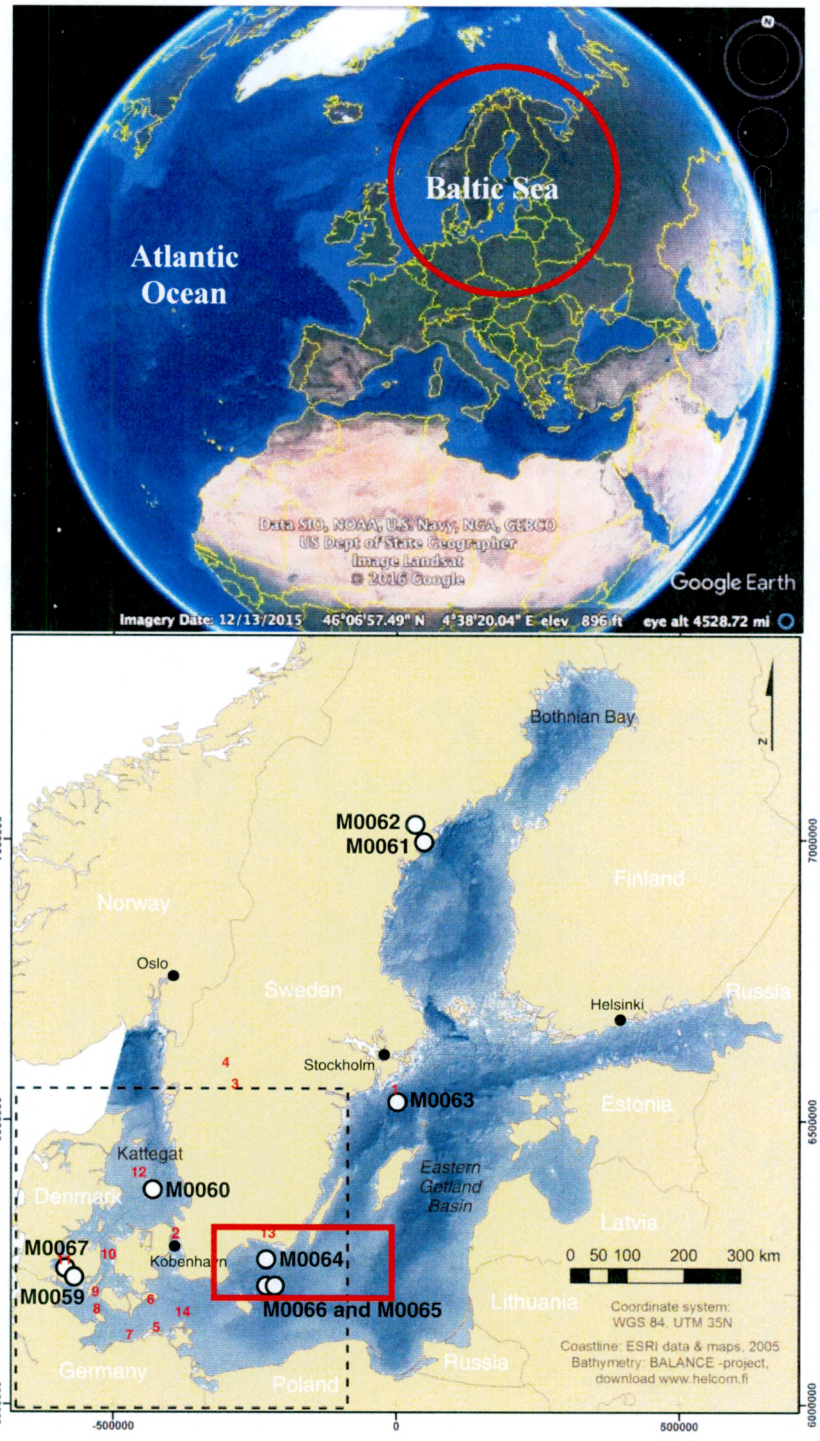

Figure 1. (A) Portion of Western Hemisphere with Baltic Sea study area circled in red (Google Earth); (B) IODP Expedition 347 map of the Baltic Sea, with site M0064 boxed in red, located in Hanö Bay (Andrén et al., 2013)

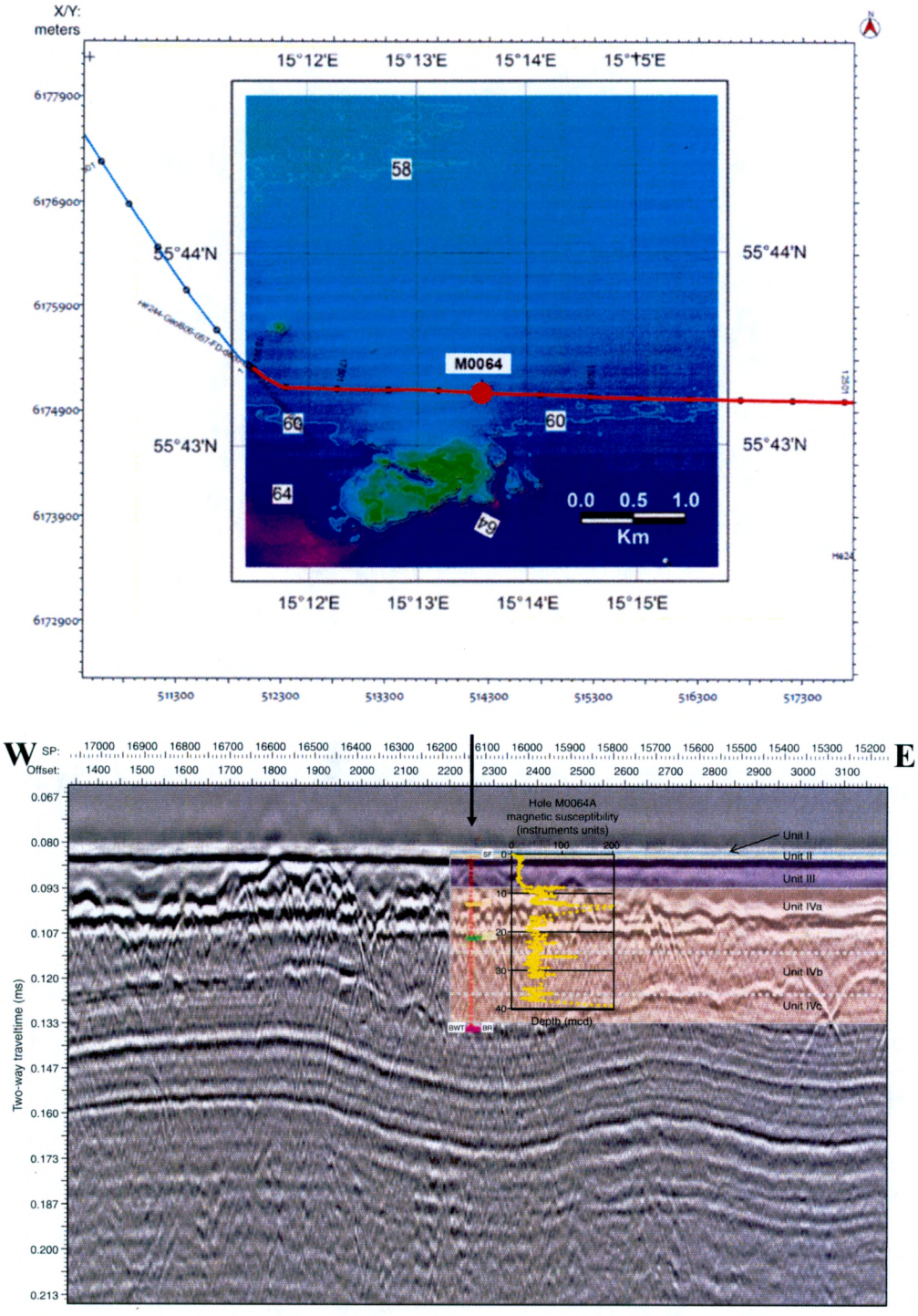

Figure 2. (A) Bathymetry map showing ship transect for Site M0064 (Andrén et al., 2013); (B) Seismic profile containing corresponding lithostratigraphic boundaries and multisensory core logger magnetic susceptibility data of Hole M0064A. SF = Seafloor, BWT = Bottom of Weichselian till, BR = Bedrock M0064 (Andrén et al., 2013).

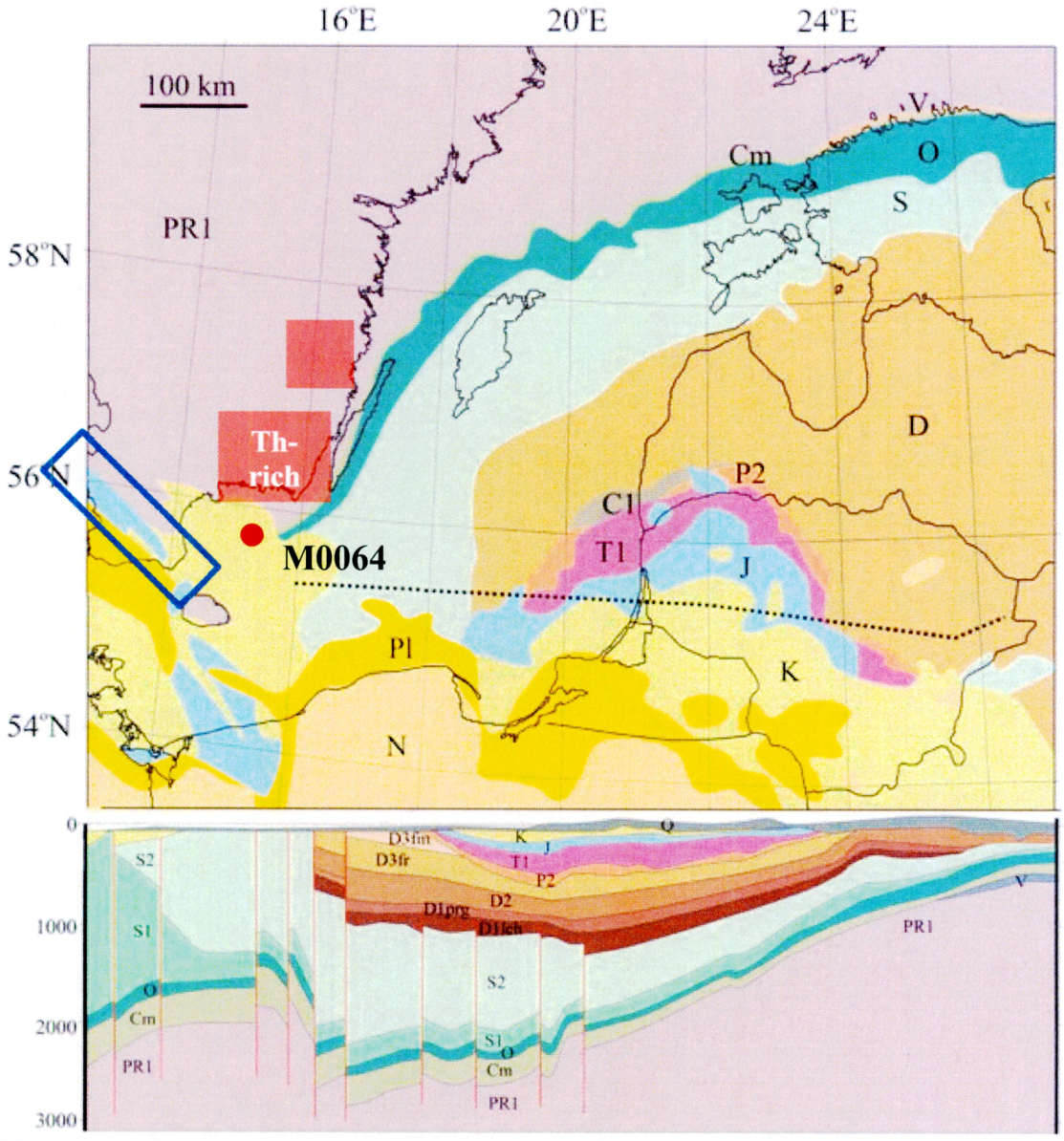

Figure 3. Regional geologic map of Hanö Bay, where project Site IODP M0064 (red dot) resides within the Cretaceous chalk (K), denoted in light yellow. Jurassic (J) sandstones, mudstones and coal seams are denoted in blue. The Esrum/Alnarp valley is boxed in dark blue (Harff et al., 2011). Precambrain (PR1) granulites make up parts of south central Sweden with occasional Thorium-rich provinces, shaded in red. Cambrian (Cm) quartz siltstones, sandstones and shales are represented by the medium green color. Ordovician (O) shaly carbonates are dark green, and Silurian (S) marlstones and limestones are light green. Devonian (D) shallow marine carbonates and sandstones and shales reside in the brown region, and Carboniferous (C1) sandstones and carbonaceous shales are a pinch of grey. Permian (P2) in salmon-orange consists of carbonates and evaporates. Triassic (T1) sediments in pink are made up of red lacustrine mudstones and arkosic sandstones. Paleogene (P1) and Neogene (N) are composed of marine sediments.

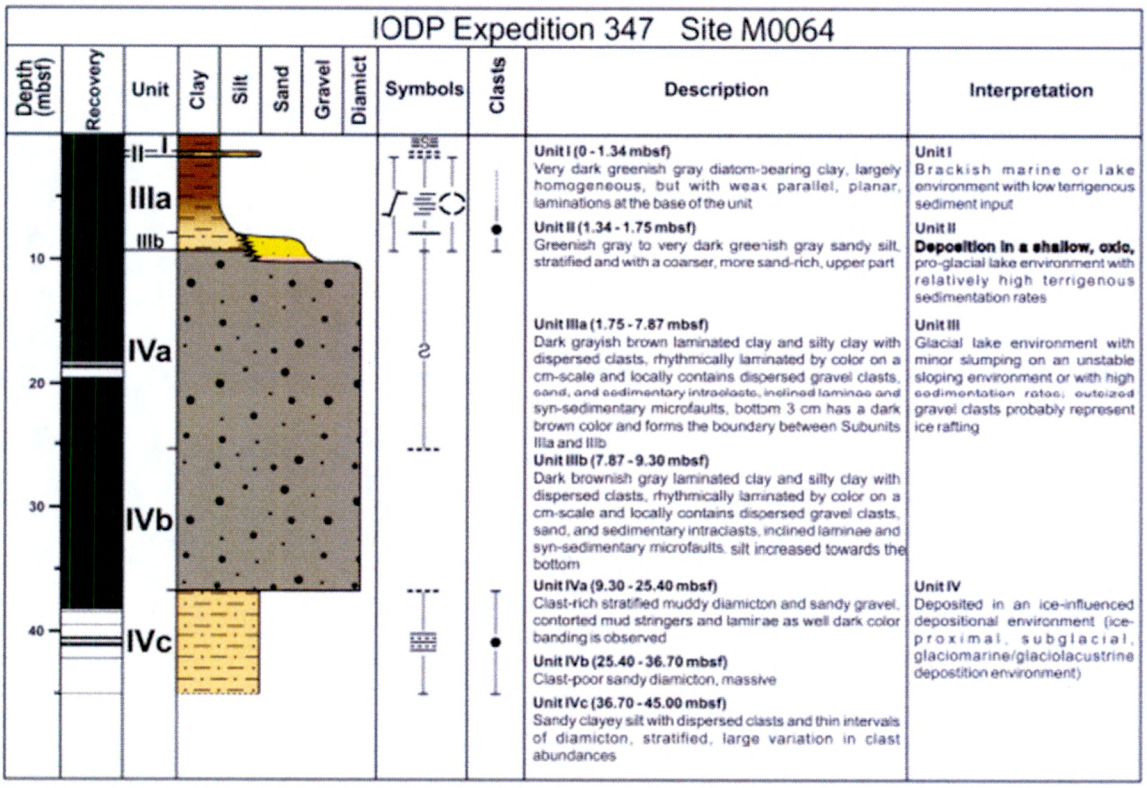

Figure 4. Lithological core log of Site M0064, with Units IIIa, IIIb, IVa, and IVb the main focus of this research, and Site M0064D (Andrén et al., 2013).

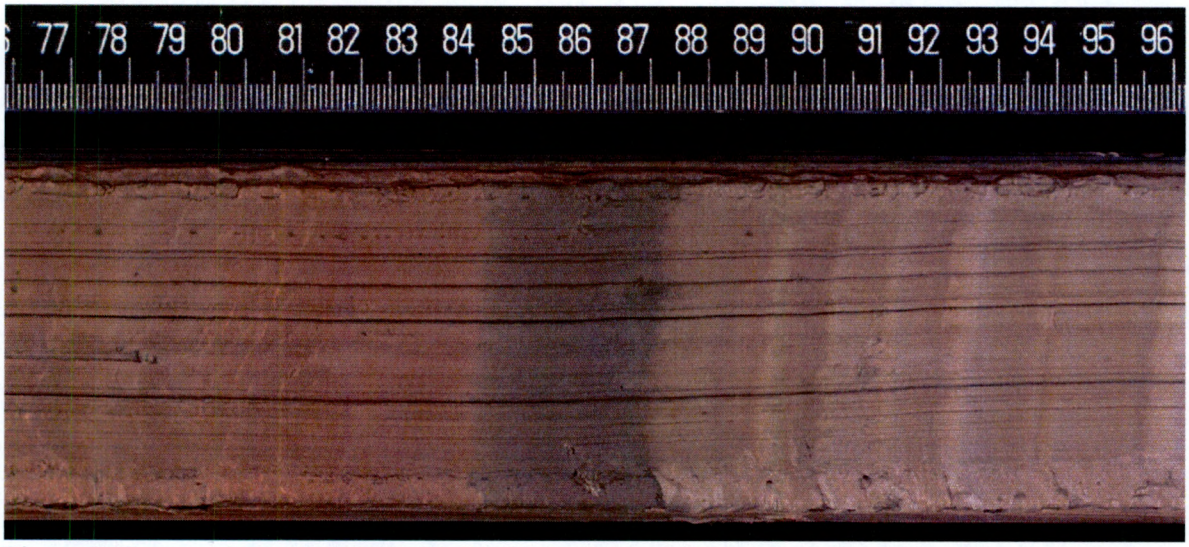

Figure 5. Core section 347-3H-2W-76-96, 7.76 – 7.96 mbsf, showing dramatic color transition at Unit IIIb (grey) to Unit IIIa (brown-red) at 87 cm (7.87 mbsf).

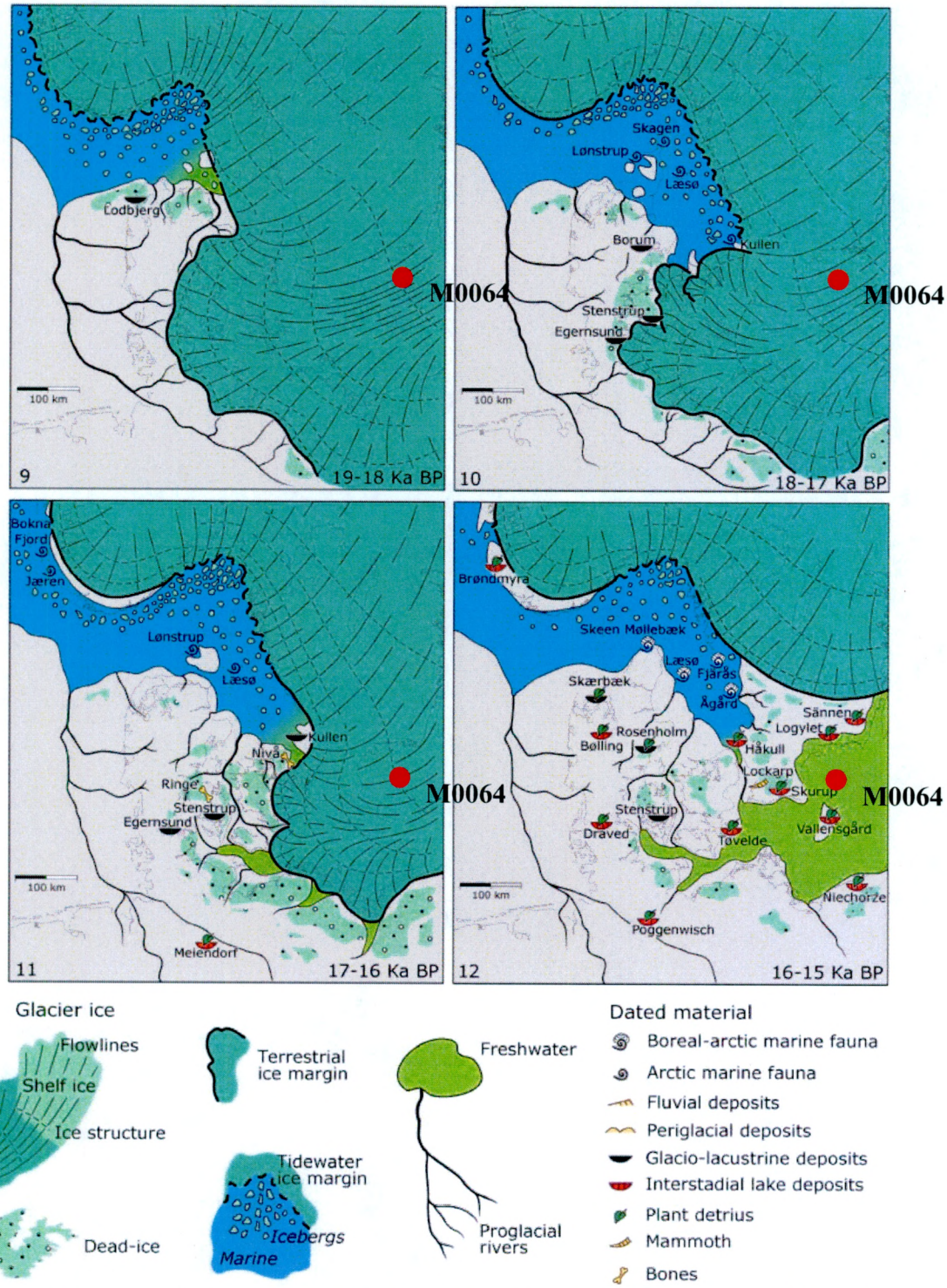

Figure 6. Deglaciation of the SIS from 19 – 15 kyr BP, relative to IODP Site M0064 (Houmark-Nielsen and Kjaer, 2003).

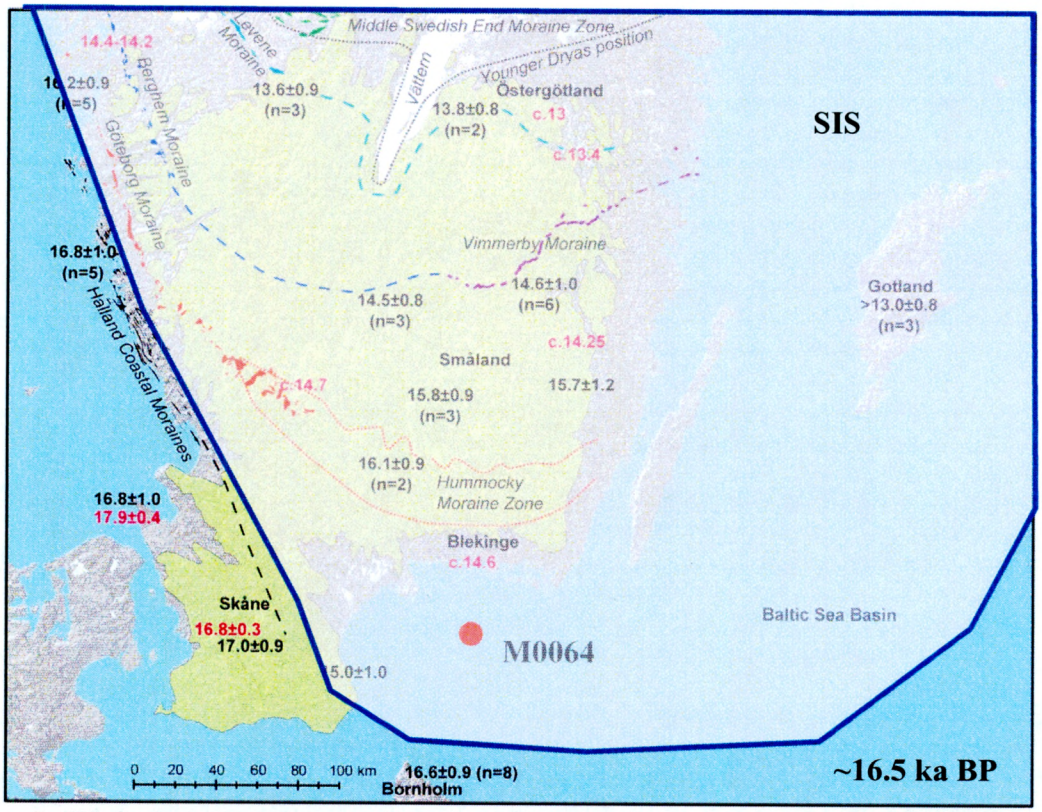

Figure 7. SIS deglaciation reconstruction of southern Sweden and Bornholm Island relative to IODP Site M0064 (red dot). Using mean cosmogenic exposure ages (black), Bornholm Island was deglaciated at about the same time as central Skane, 16.6 ± 0.9 ka BP, and a lobe of the SIS may have been present in Hanö Bay during this time (Anjar et al., 2014).

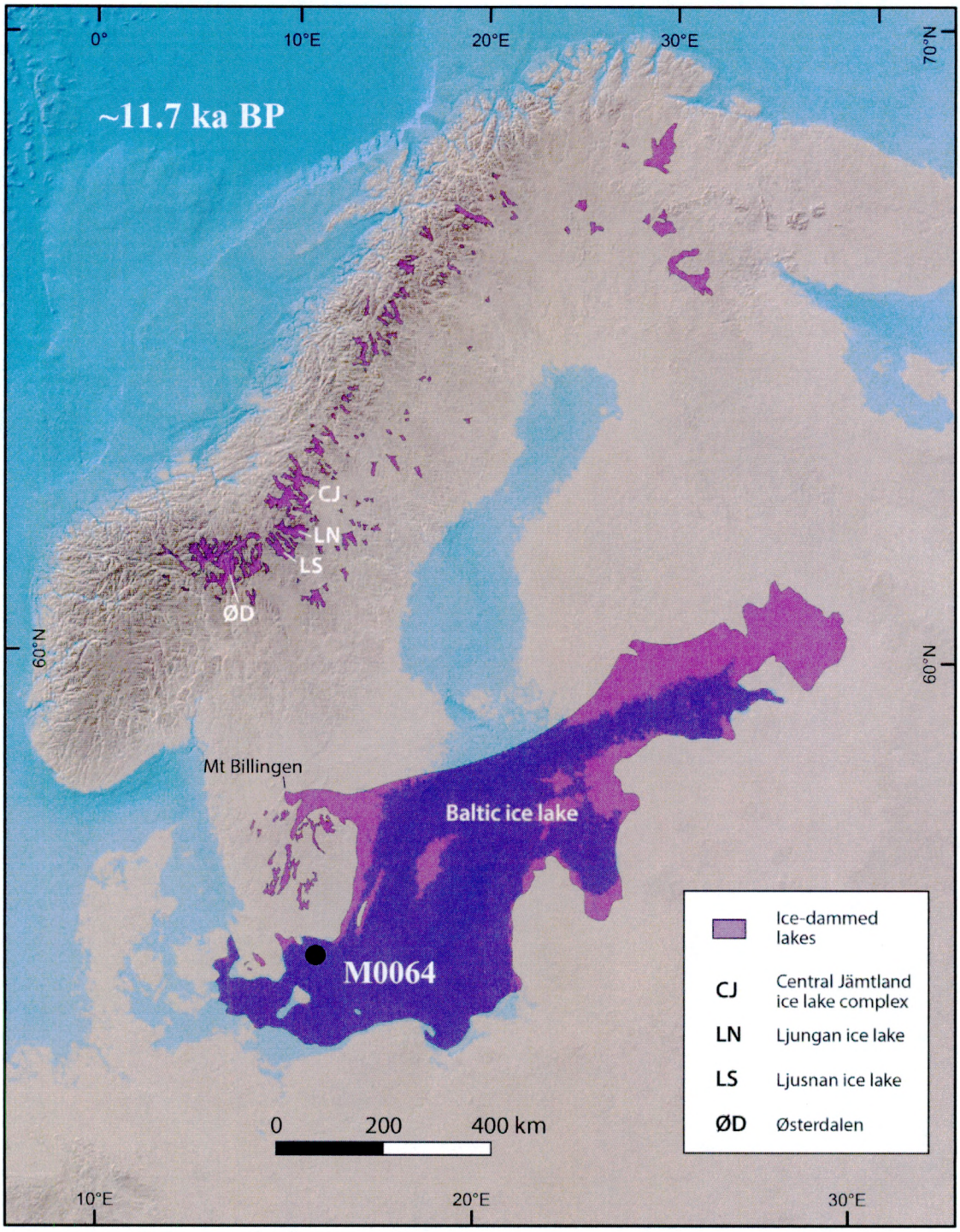

Figure 8. Scandinavian glacial lakes, and the ice-dammed BIL (purple), existing during the Younger Dryas, 11.7 ka BP, when the ice margin reached Mt. Billingen. IODP Site M0064 denoted by black dot (Stroeven et al., 2015).

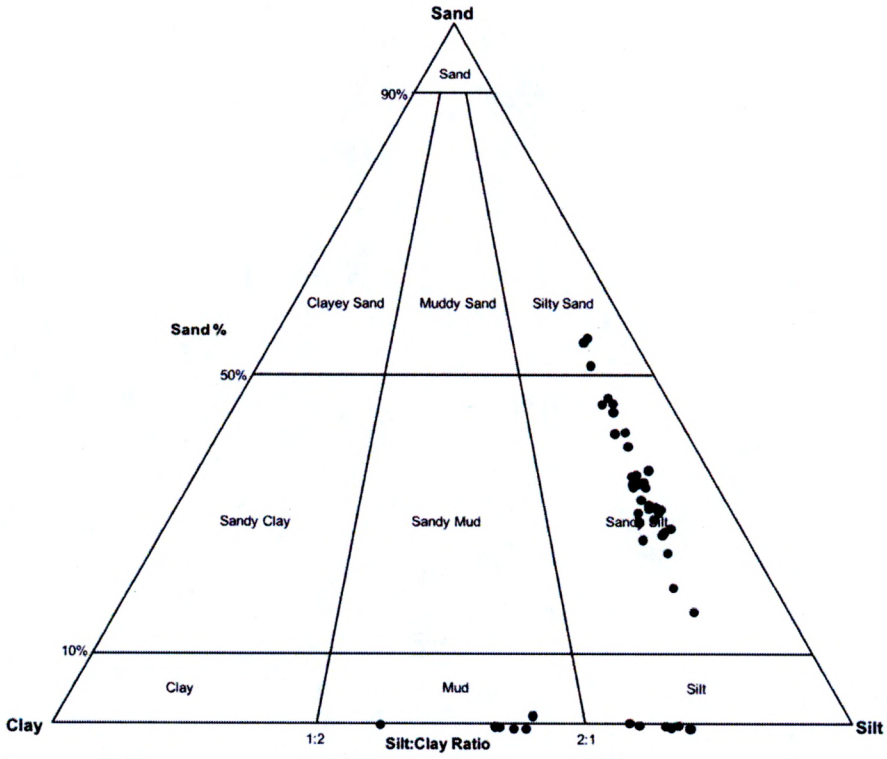

Figure 9. Sand Silt Clay diagram generated by GRADISTAT of all measured M0064 samples using laser particle size Samples plotting below the line represent 0% sand. Sandy silts and silty sands are indicative of diamicton samples, and muds and silts are the lacustrine rhythmites.

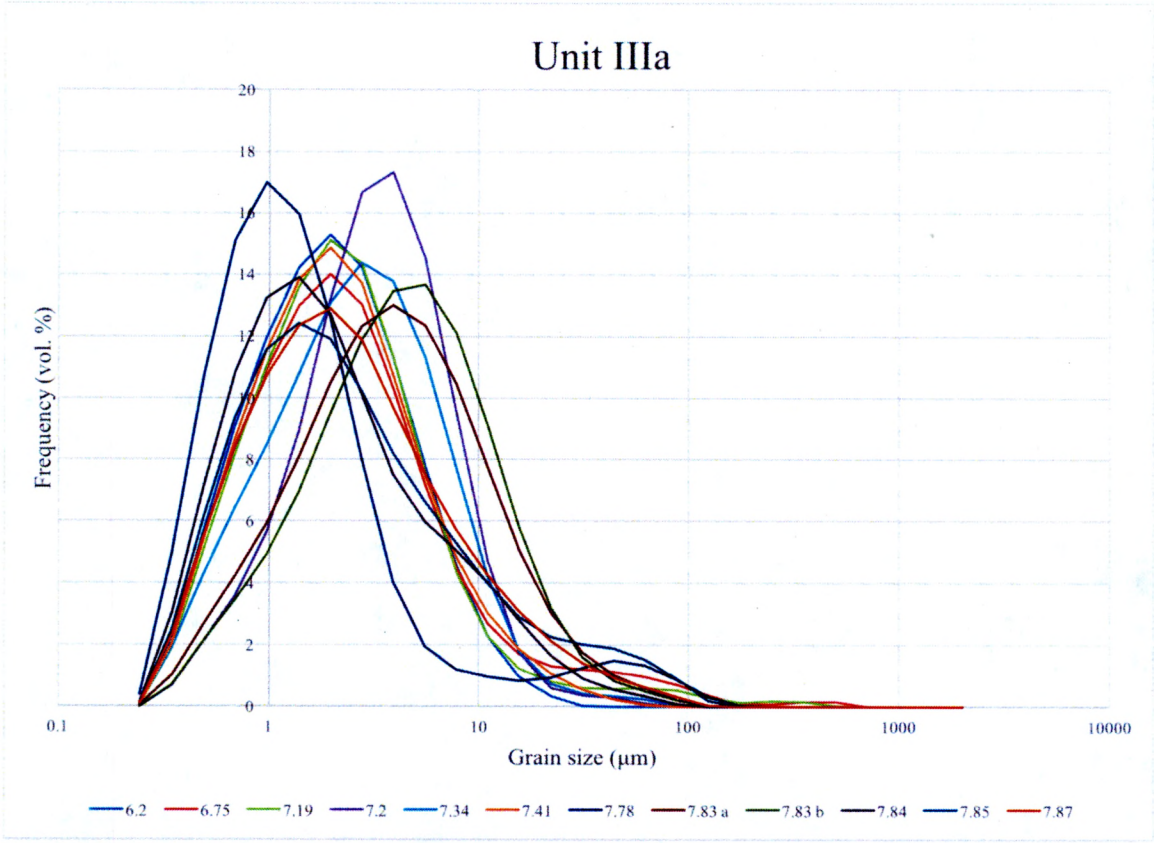

Figure 10. Unit IIIa grain size (µm) distribution with frequency (vol. %) at specified depths (mbsf).

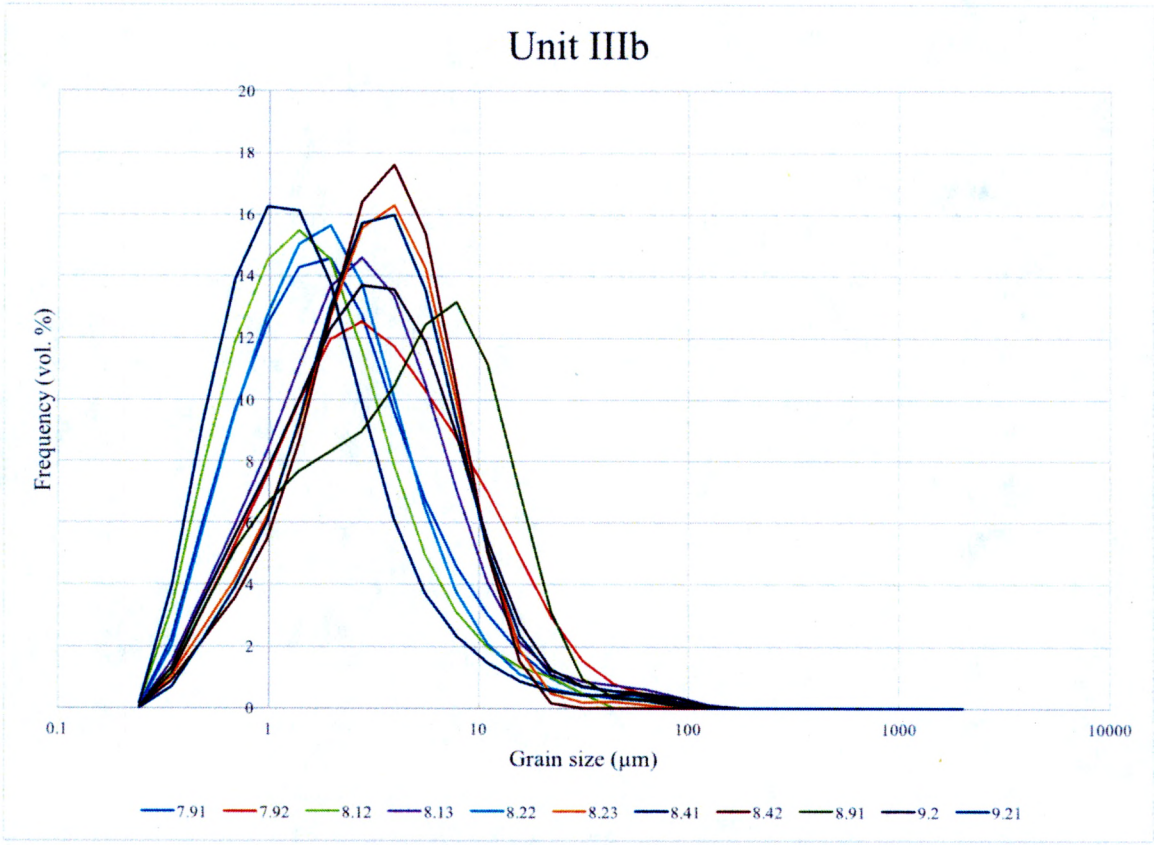

Figure 11. Unit IIIb grain size (µm) distribution with frequency (vol. %) at specified depths (mbsf).

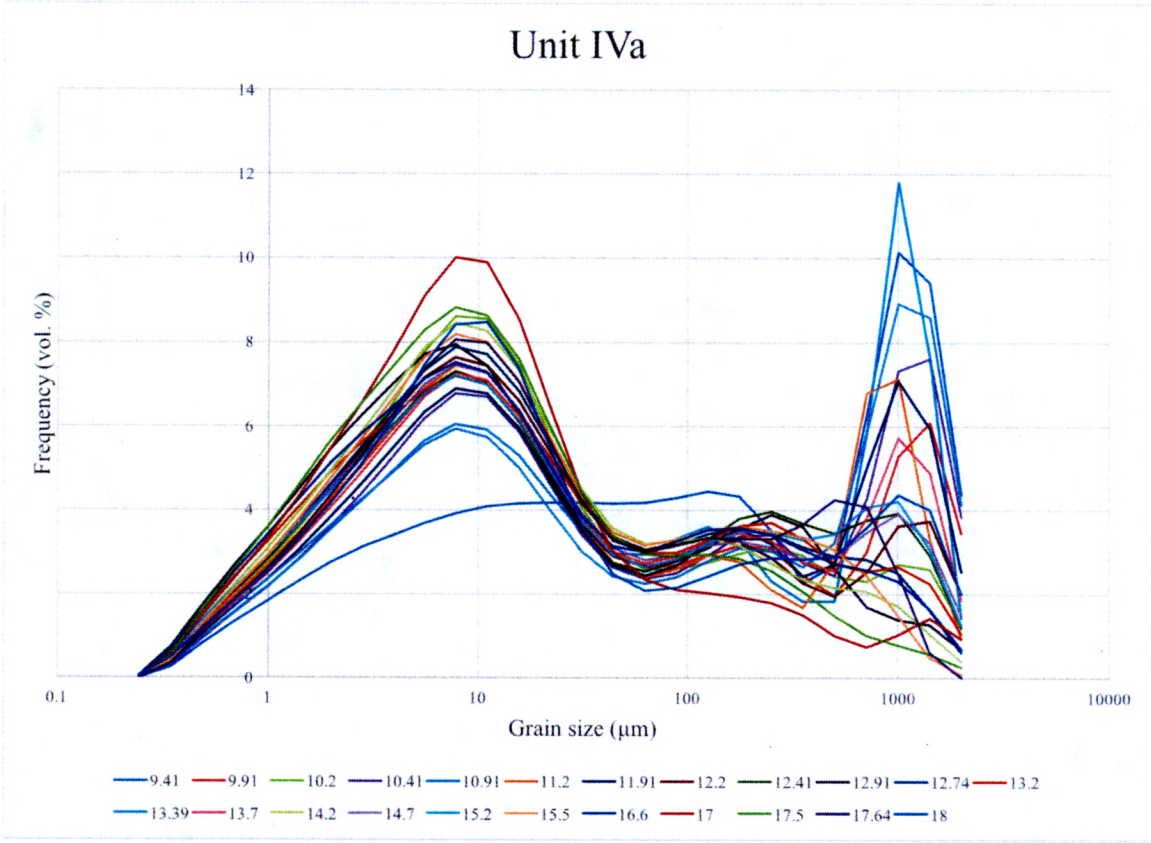

Figure 12. Unit IVa grain size (µm) distribution with frequency (vol. %) at specified depths (mbsf).

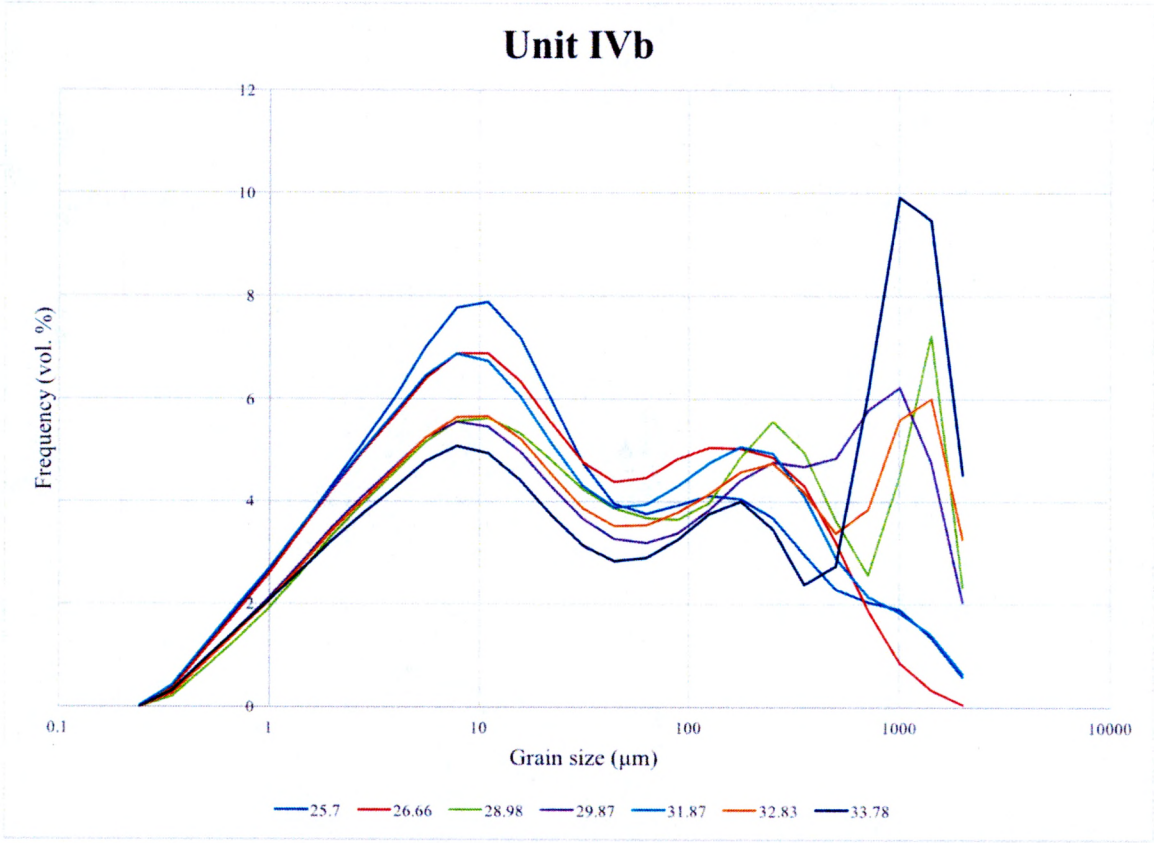

Figure 13. Unit IVb grain size (µm) distribution with frequency (vol. %) at specified depths (mbsf).

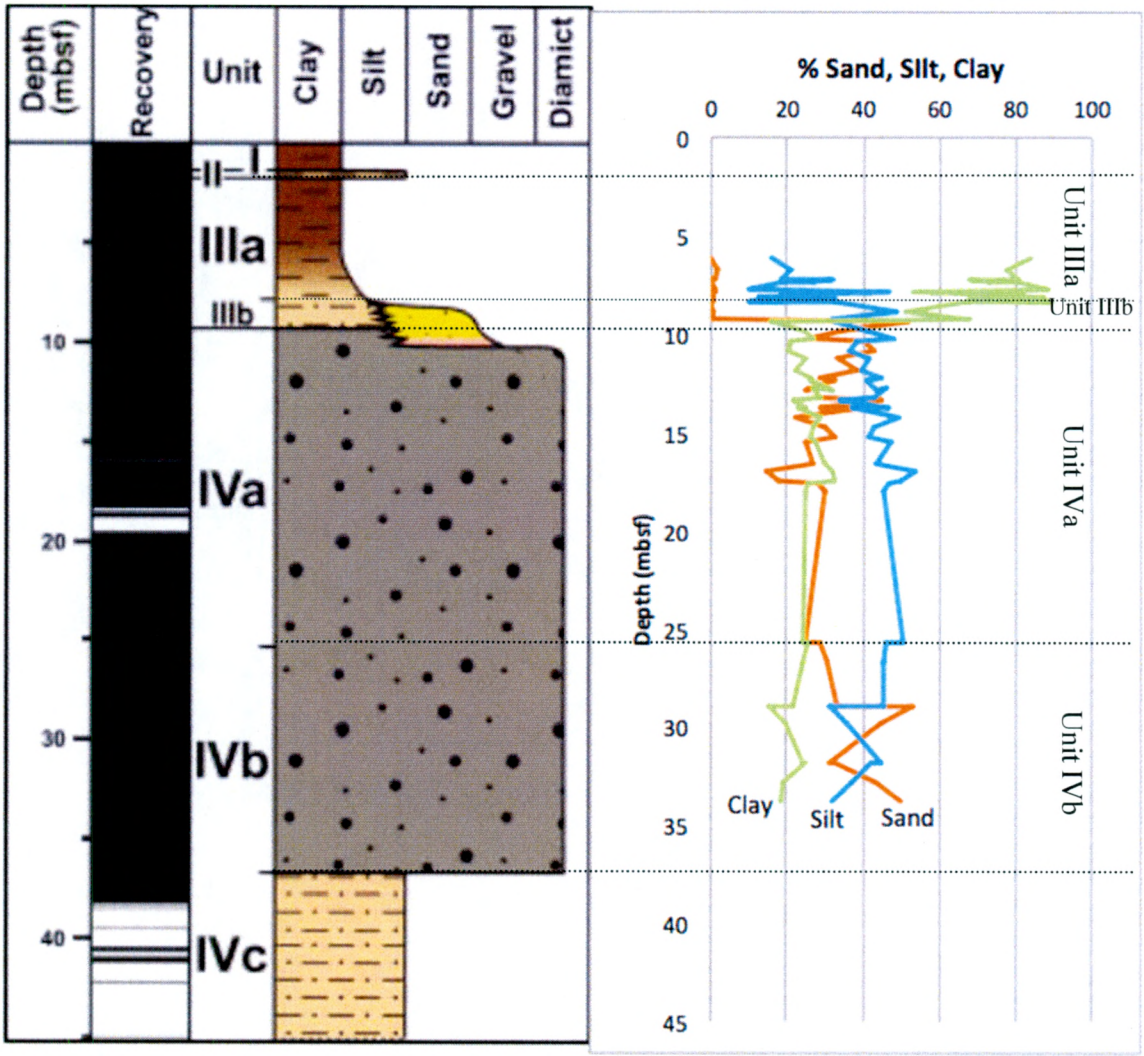

Figure 14. Sand (orange), silt (blue), and clay (green) percentages down core (mbsf). Dotted black lines separate individual units.

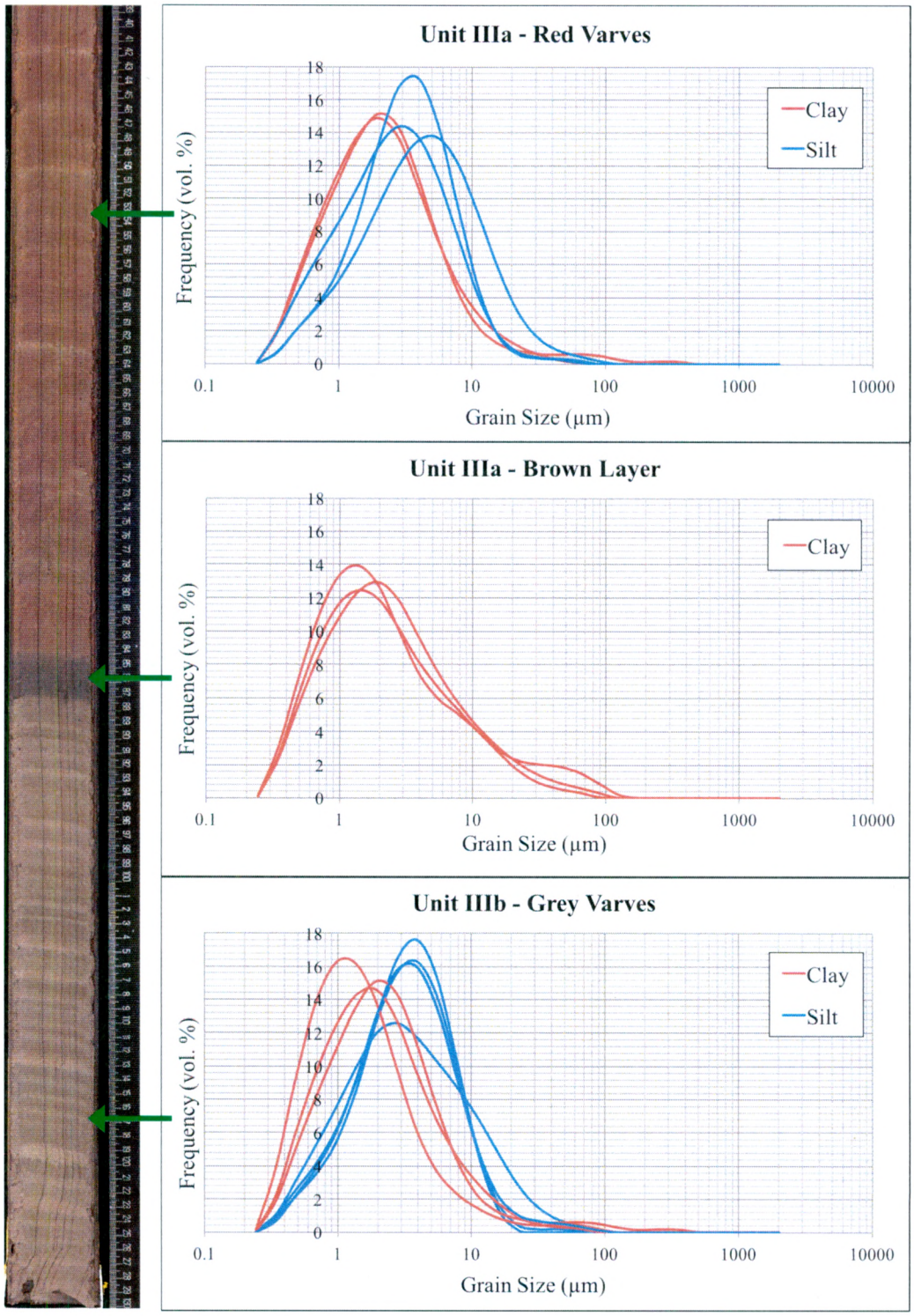

Figure 15. Left: Core section 347-64D-3H-2W-39-130 (7.39 – 8.3 mbsf), with transition from Unit IIIb to Unit IIIa at 7.87 mbsf. Right: Grain size (µm) distribution and frequency (vol. %) of silt-clay couplets in red varves of Unit IIIa, grey varves of Unit IIIb, and samples in brown layer of Unit IIIa. Green arrows denote according lithology at left laterally matches particle size graphs at right.

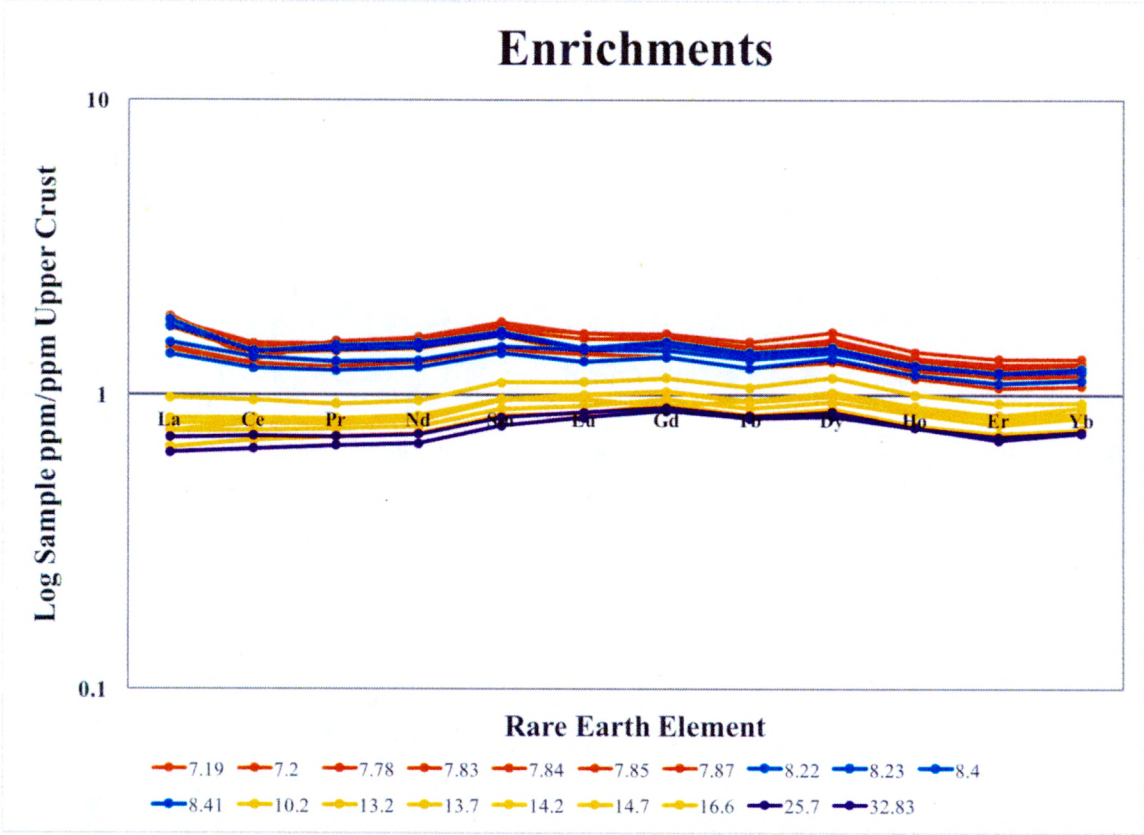

Figure 16. Enrichment factors of Rare Earth Elements ppm/ppm Upper Crustal values (McLennan, 2001) for M0064 at according depths in mbsf. Depth values are separated by colors and units, where orange is Unit IIIa, blue is Unit IIIb, yellow is Unit IVa and purple is Unit IVb.

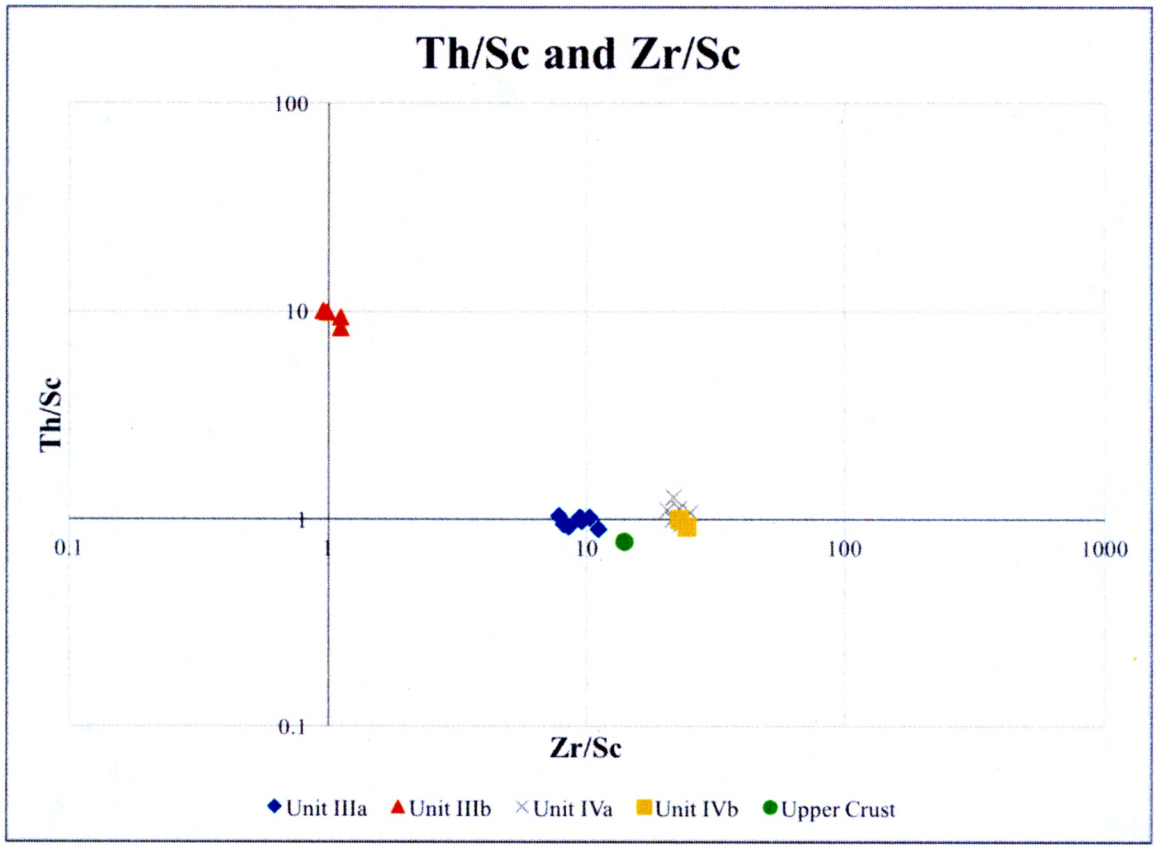

Figure 17. Th/Sc and Zr/Sc ratios (ppm) plotted by Unit, and with Upper Crust (McLennan, 2001). Blue diamonds represent Unit IIIa, orange triangles indicate Unit IIIb, grey X's are Unit IVa, and yellow squares represent Unit IVb. Upper Crust is indicated by a green circle.

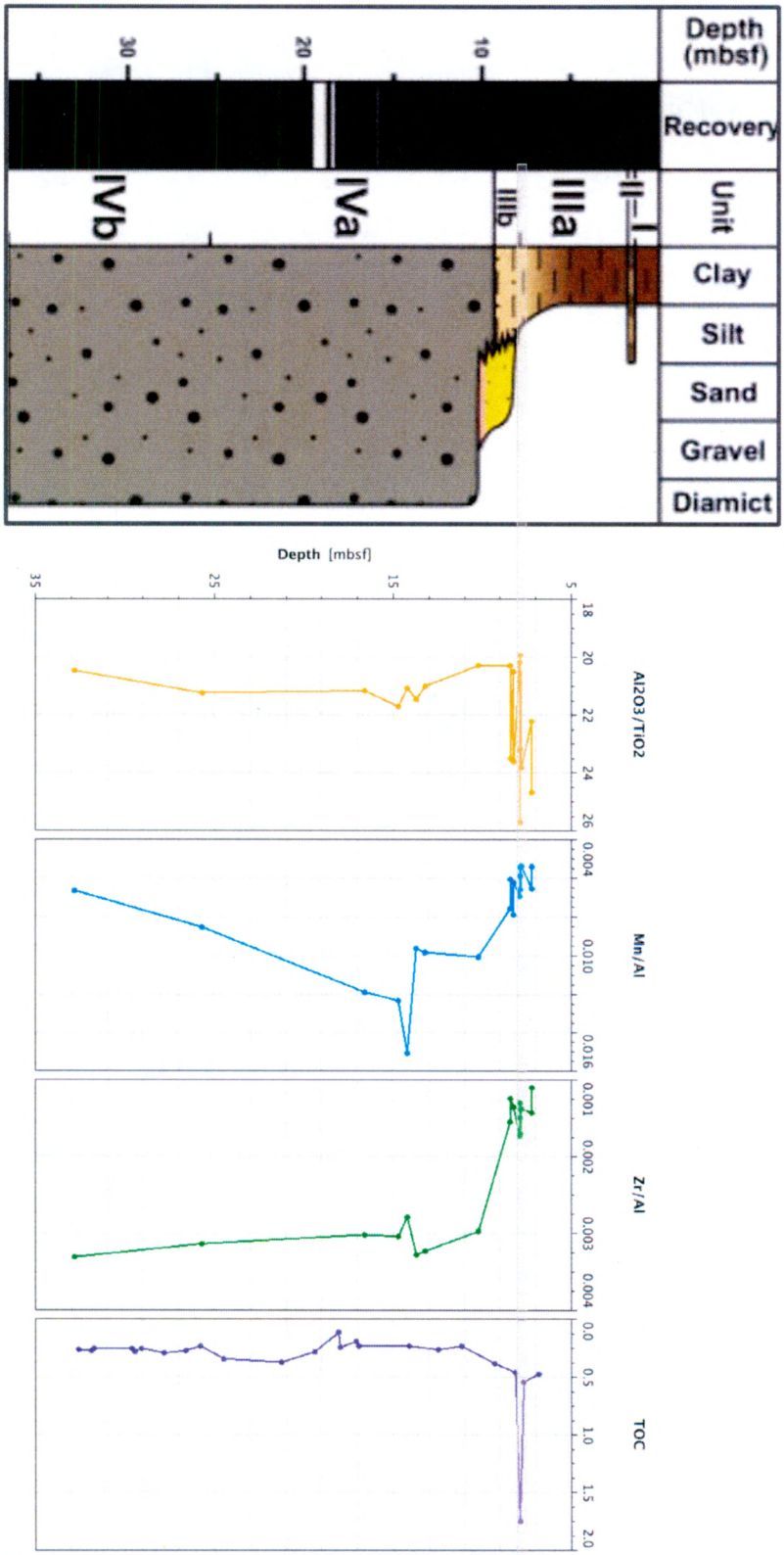

Figure 18. Al_2O_3/TiO_2, Mn/Al, and Zr/Al ratios (wt. %) of M0064 plotted down core (mbsf) using ICP-OES data. TOC (wt. %) data taken from shipboard data. Shaded region is of 8.5 – 7 mbsf, with transition from Unit IIIb to Unit IIIa, shown in Figure 14.

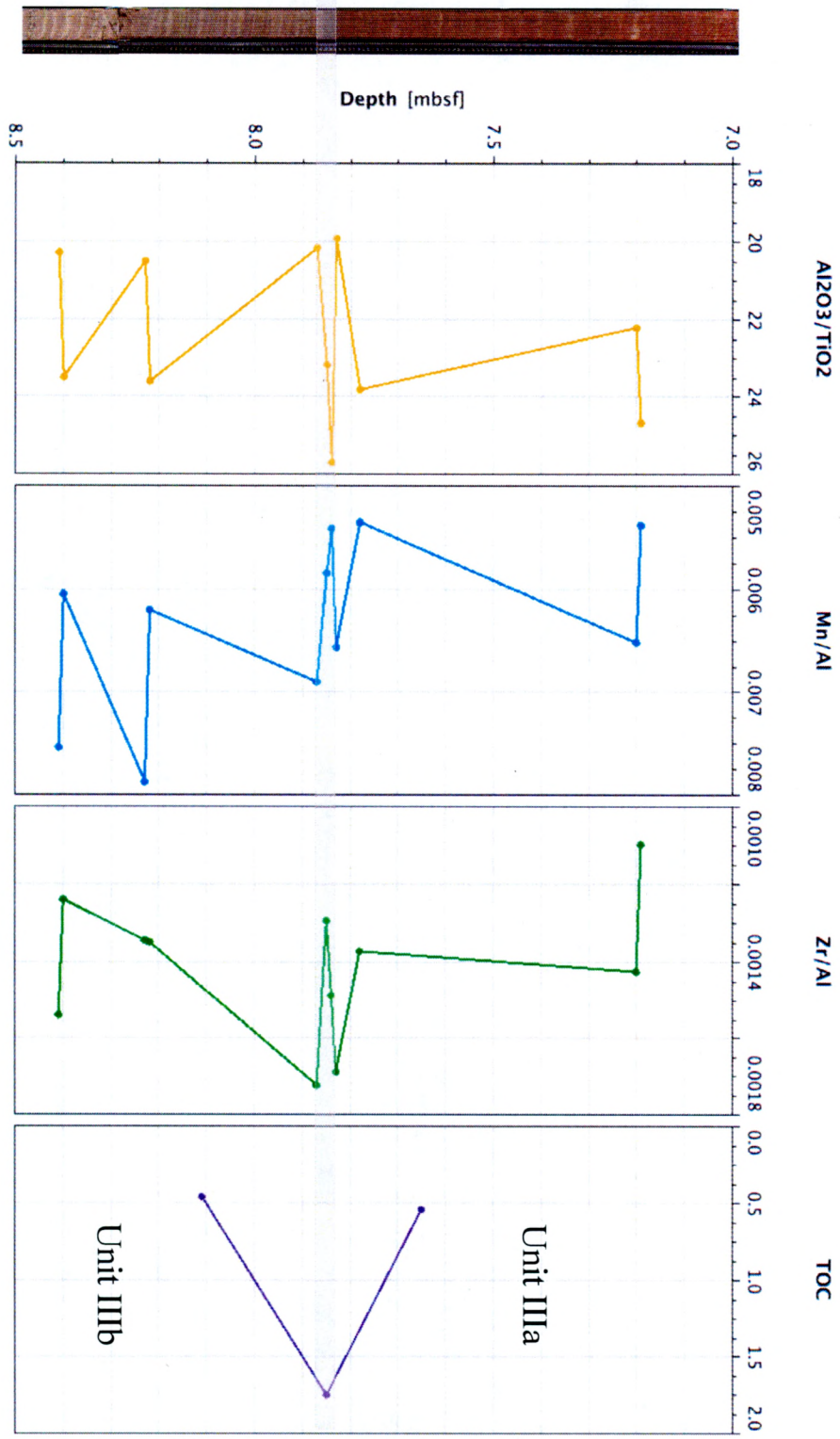

Figure 19. Zoom in on Figure 13, 8.5 – 7 mbsf, with brown layer shaded in grey (7.87 – 7.85 mbsf), showing color transition from Unit IIIb to Unit IIIa. Al_2O_3/TiO_2, Mn/Al, and Zr/Al ratios (wt. %) of M0064 plotted using ICP-OES data. TOC (wt. %) data taken from shipboard data.

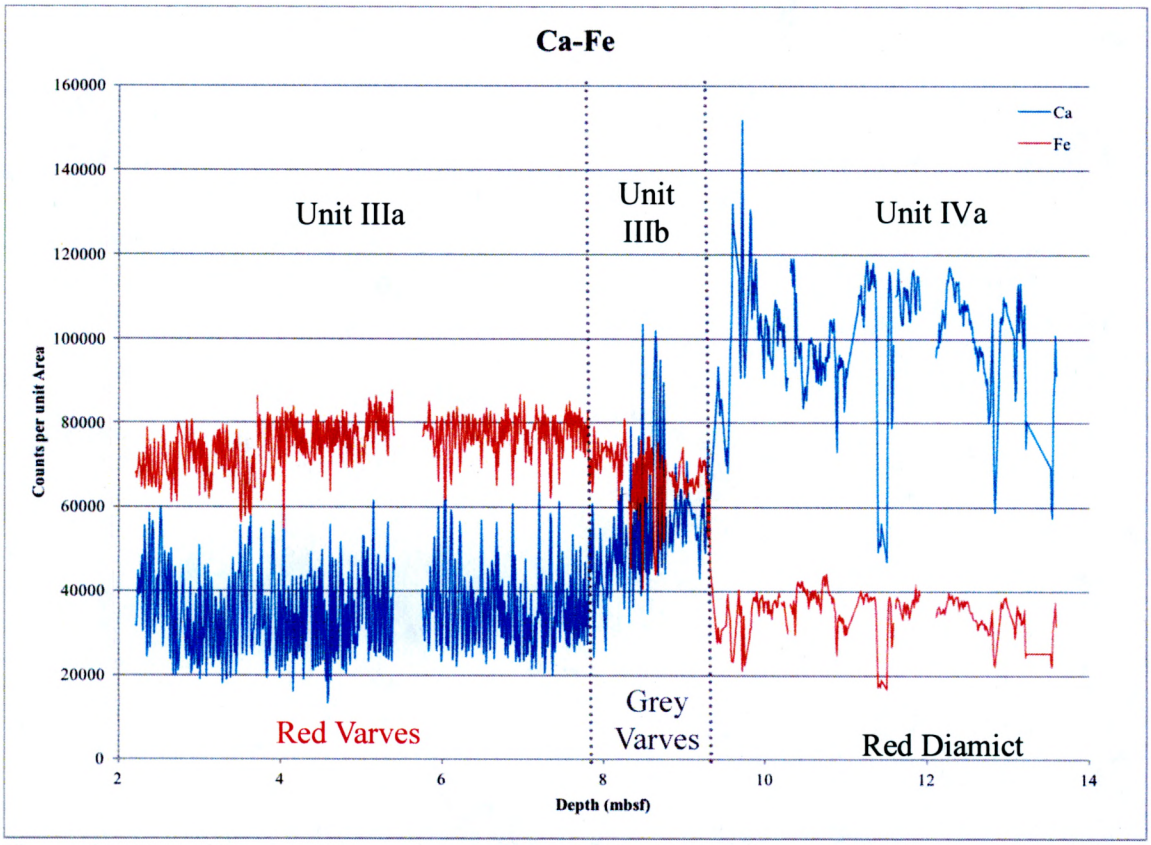

Figure 20. Ca and Fe counts per unit area across M0064D core depth (mbsf). Unit IIIa and IIIb and Unit IIIb and Unit IVa boundaries are denoted by dotted lines at 7.87 mbsf and 9.3 mbsf, respectively.

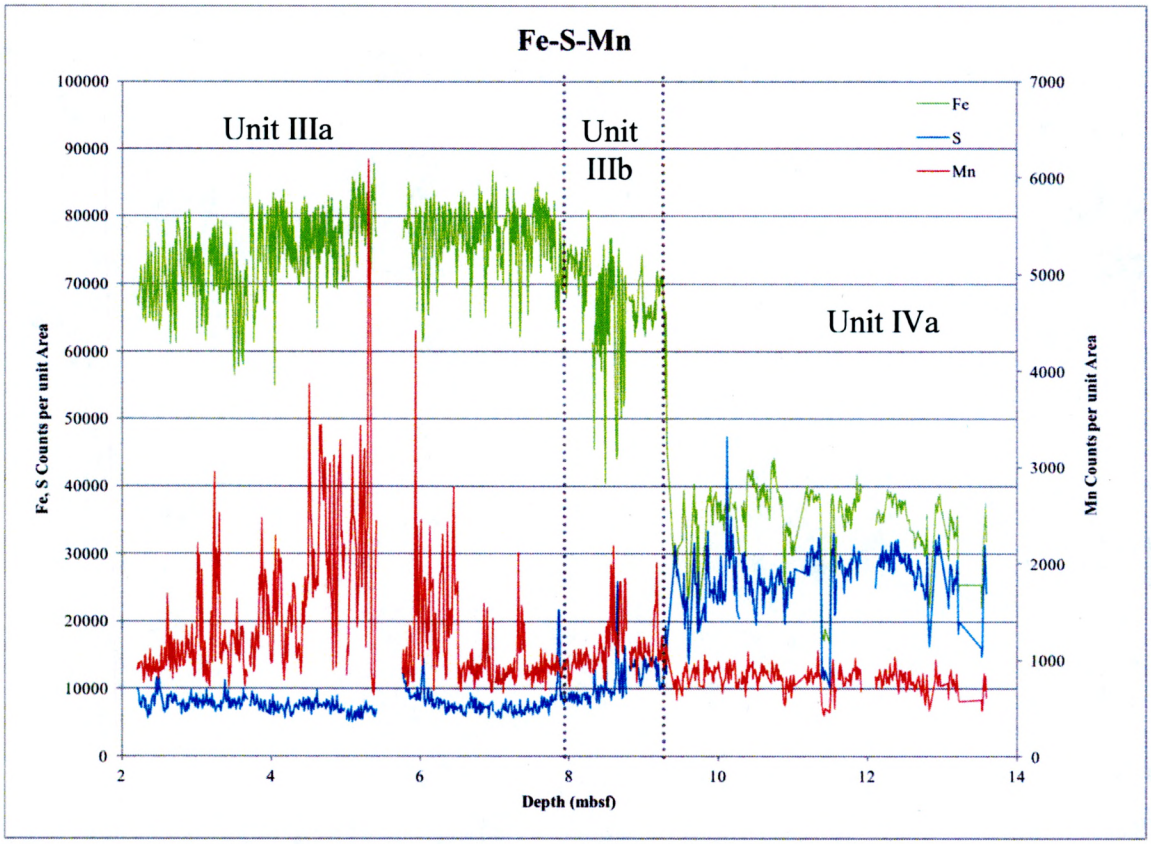

Figure 21. Fe, S, and Mn counts per unit area across M0064D core depth (mbsf). Unit IIIa and IIIb and Unit IIIb and Unit IVa boundaries are denoted by dotted lines at 7.87 mbsf and 9.3 mbsf, respectively.

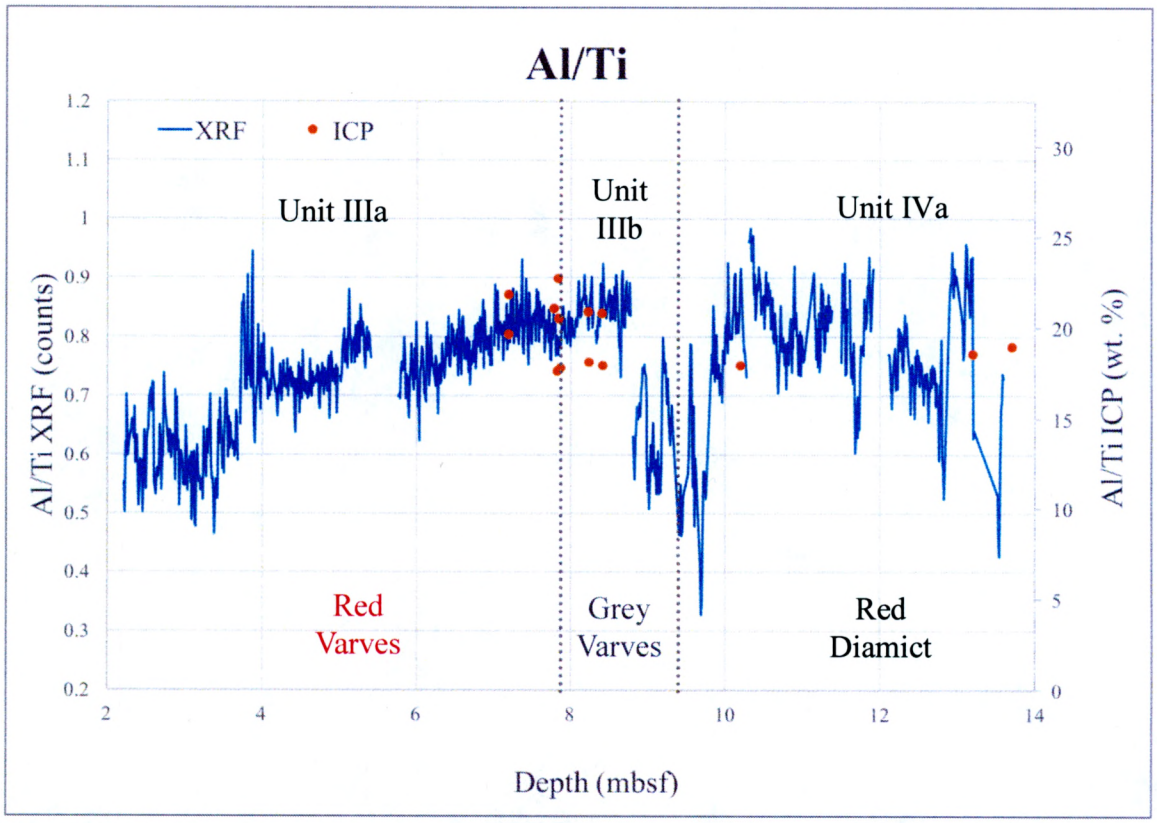

Figure 22. Al/Ti counts per unit area from XRF data (blue) across M0064D core depth (mbsf) with according ICP-OES data points in wt. % (orange). Unit IIIa and IIIb and Unit IIIb and Unit IVa boundaries are denoted by dotted lines at 7.87 mbsf and 9.3 mbsf, respectively.

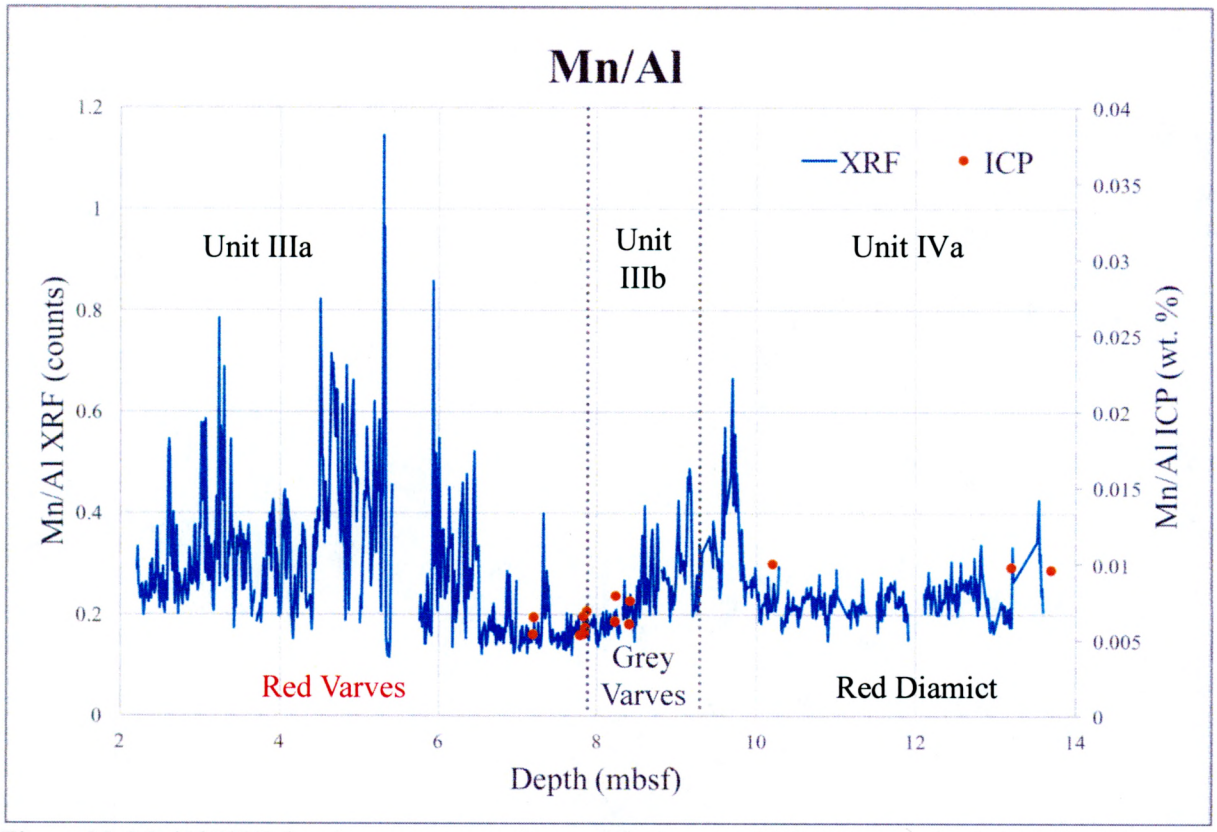

Figure 23. Mn/Al XRF data in counts per unit area (blue) across M0064D core depth (mbsf) with according ICP data points in wt. % (orange). Unit IIIa and IIIb and Unit IIIb and Unit IVa boundaries are denoted by dotted lines at 7.87 mbsf and 9.3 mbsf, respectively.

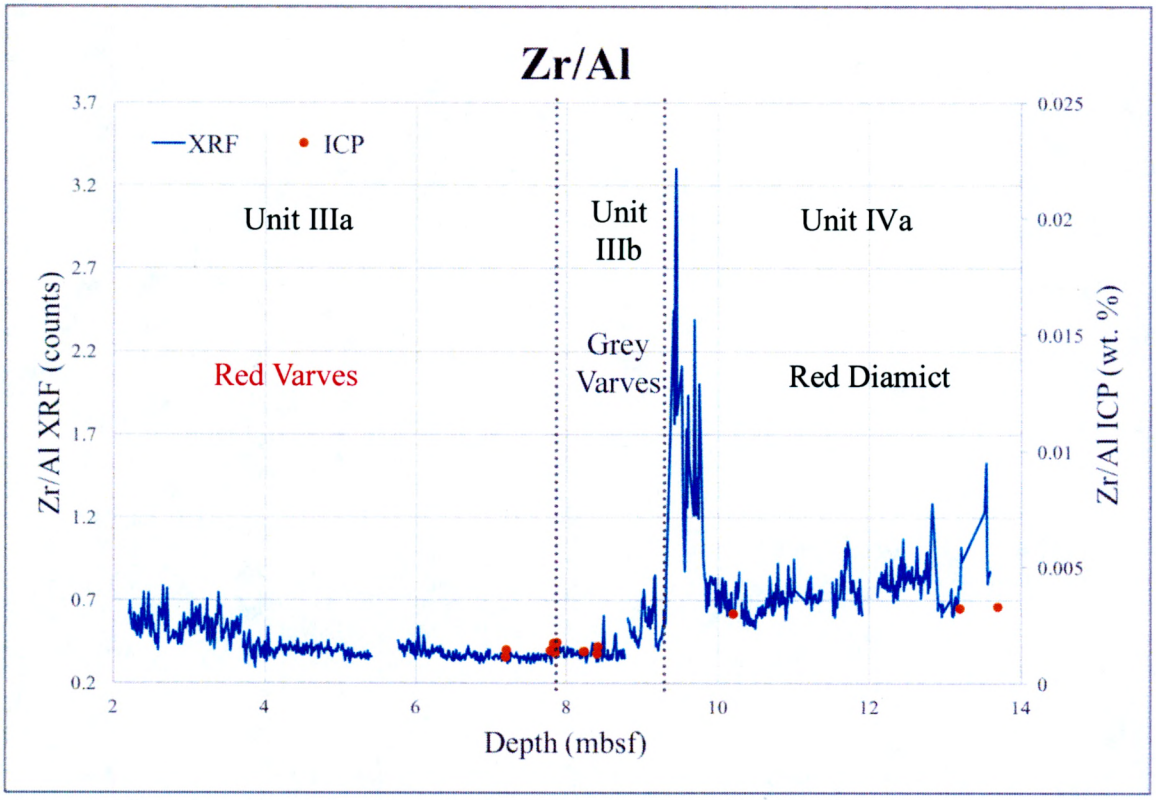

Figure 24. Zr/Al XRF counts per unit area (blue) across M0064D core depth (mbsf) with according ICP data points in wt. % (orange). Boundaries between Unit IIIa and IIIb and Unit IIIb and Unit IVa boundaries are denoted by dotted lines at 7.87 mbsf and 9.3 mbsf, respectively.

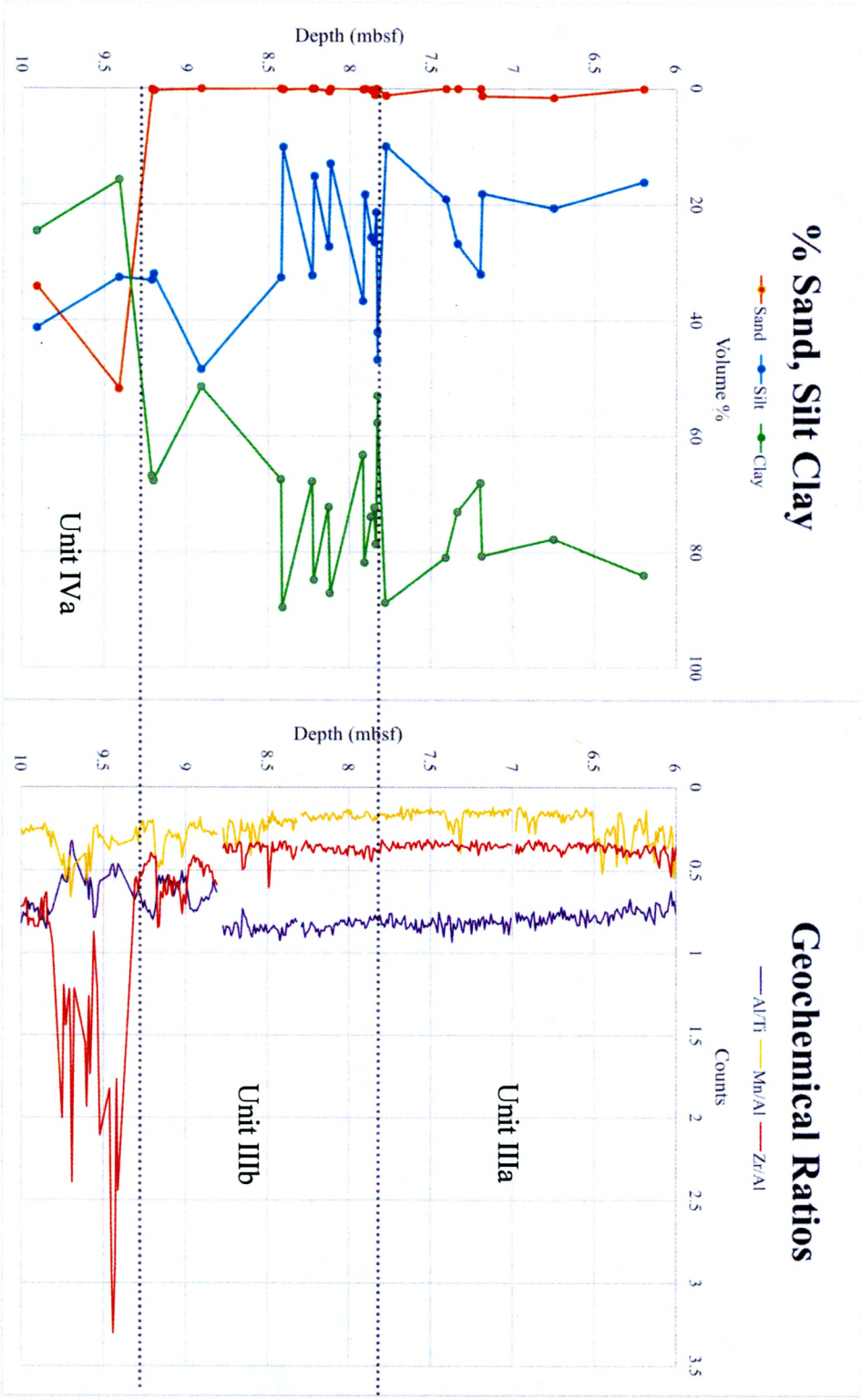

Figure 25. Grain size distribution 6 – 10 mbsf. Sand (orange), silt (blue), and clay (green) plotted next to Al/Ti (purple), Mn/Al (yellow) and Zr/Al (red). Dotted black lines separate individual units.

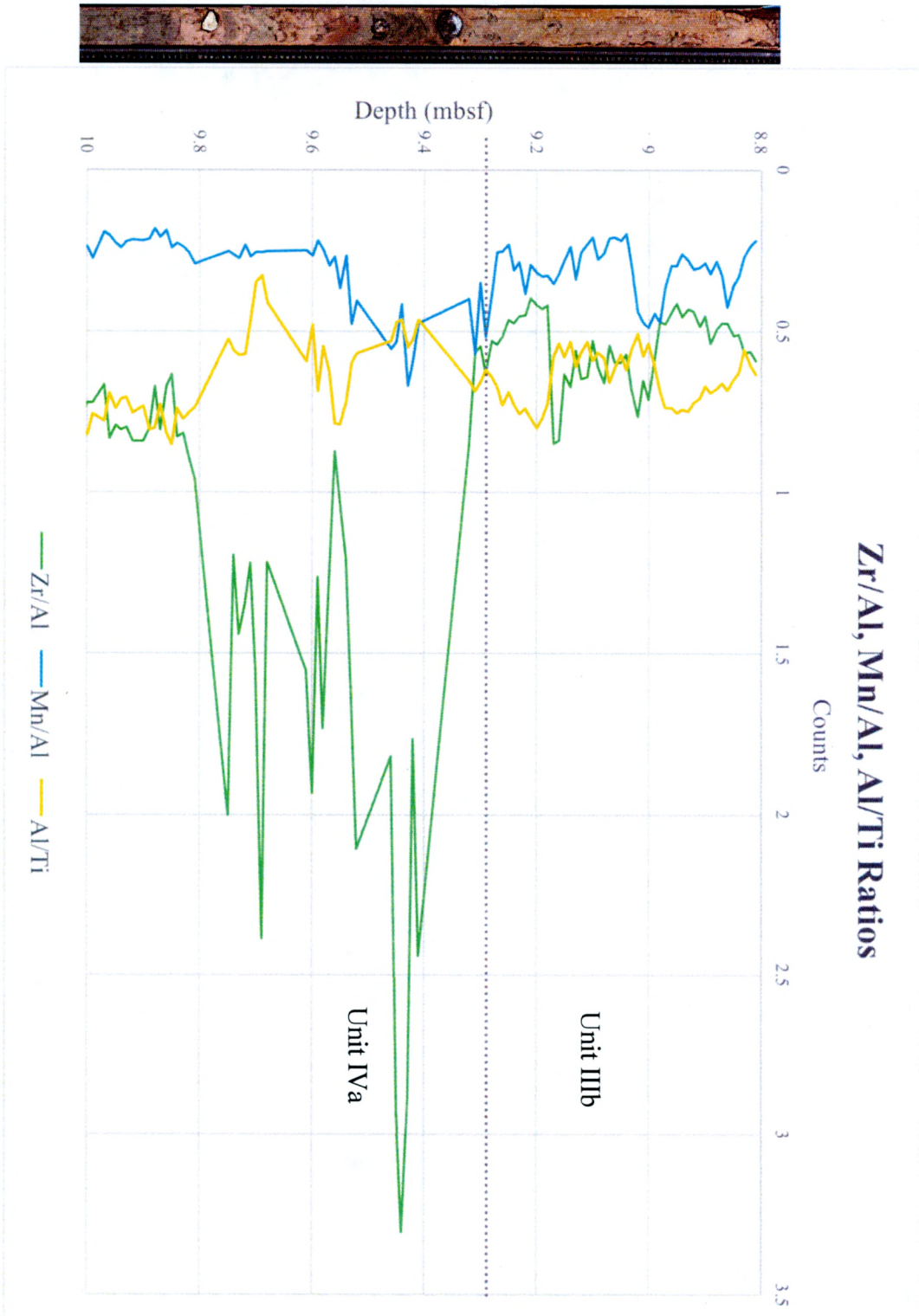

Figure 26. XRF counts per unit area of Zr/Al (green), Mn/Al (blue) and Al/Ti (yellow) across 10 – 8.8 mbsf M0064D core depth. Transition from Unit IVa to Unit IIIb denoted by grey dotted line at 9.3 mbsf.

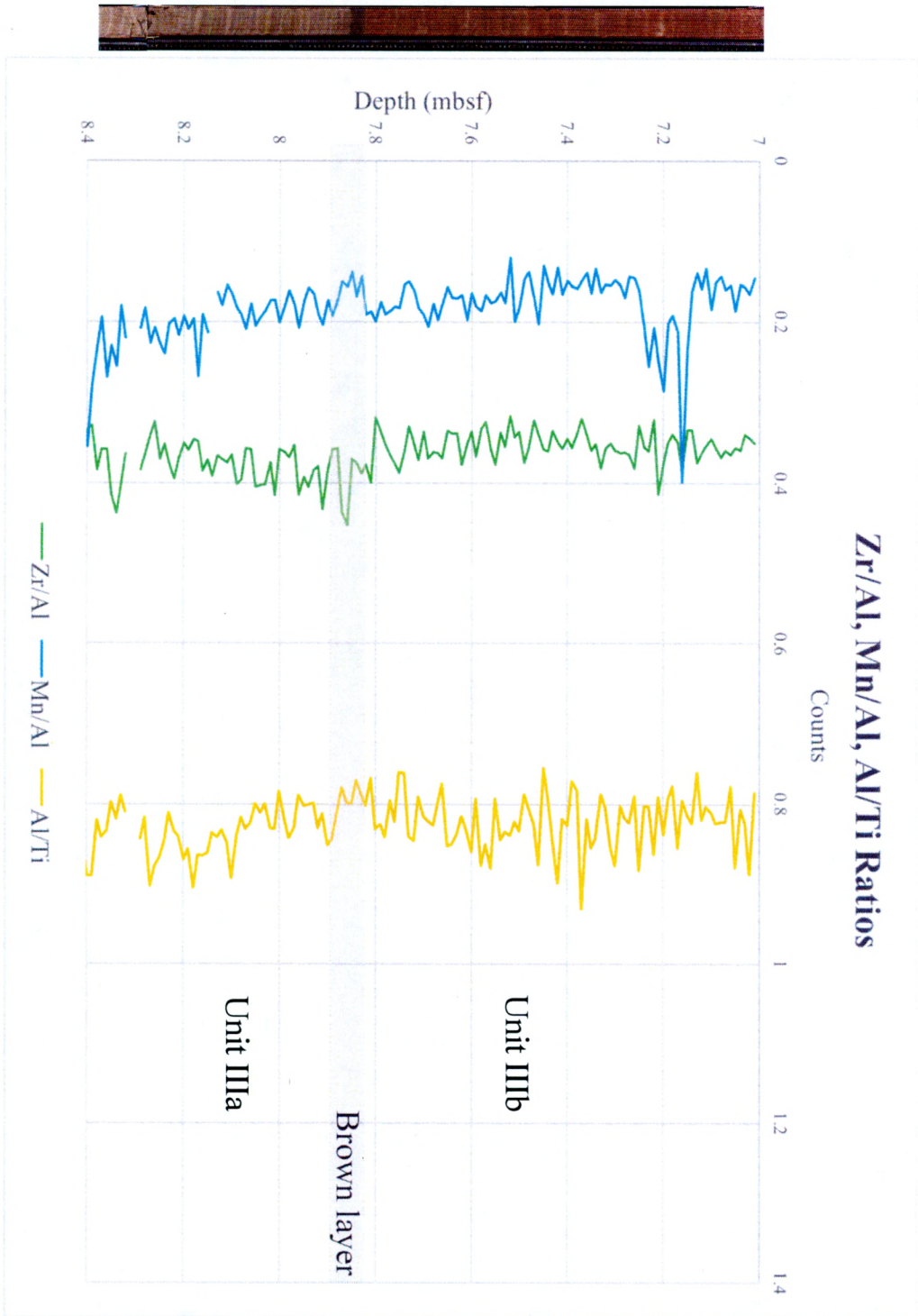

Figure 27. XRF counts per unit area of Zr/Al (green), Mn/Al (blue) and Al/Ti (yellow) across 8.4 – 7 mbsf M0064D core depth, with core image at left. Brown layer is denoted by shaded region (7.87 – 7.85 mbsf) with Unit IIIb as the lower boundary, and Unit IIIa 7.87 mbsf and above.

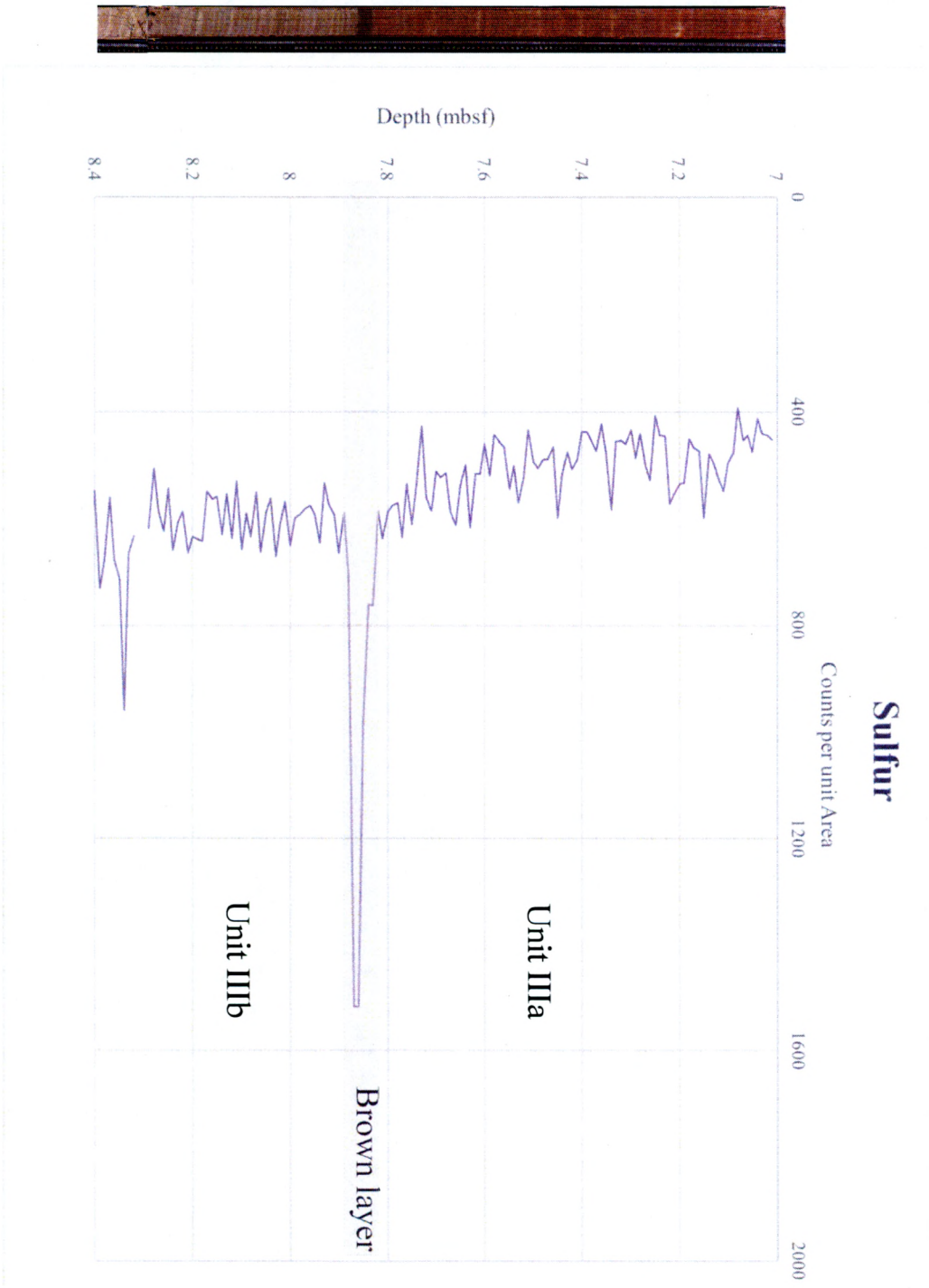

Figure 28. XRF sulfur counts across 8.4 – 7 mbsf M0064D core depth, with core image at left. Brown layer is denoted by shaded region (7.87 – 7.85 mbsf) with Unit IIIb as the lower boundary, and Unit IIIa 7.87 mbsf and above.

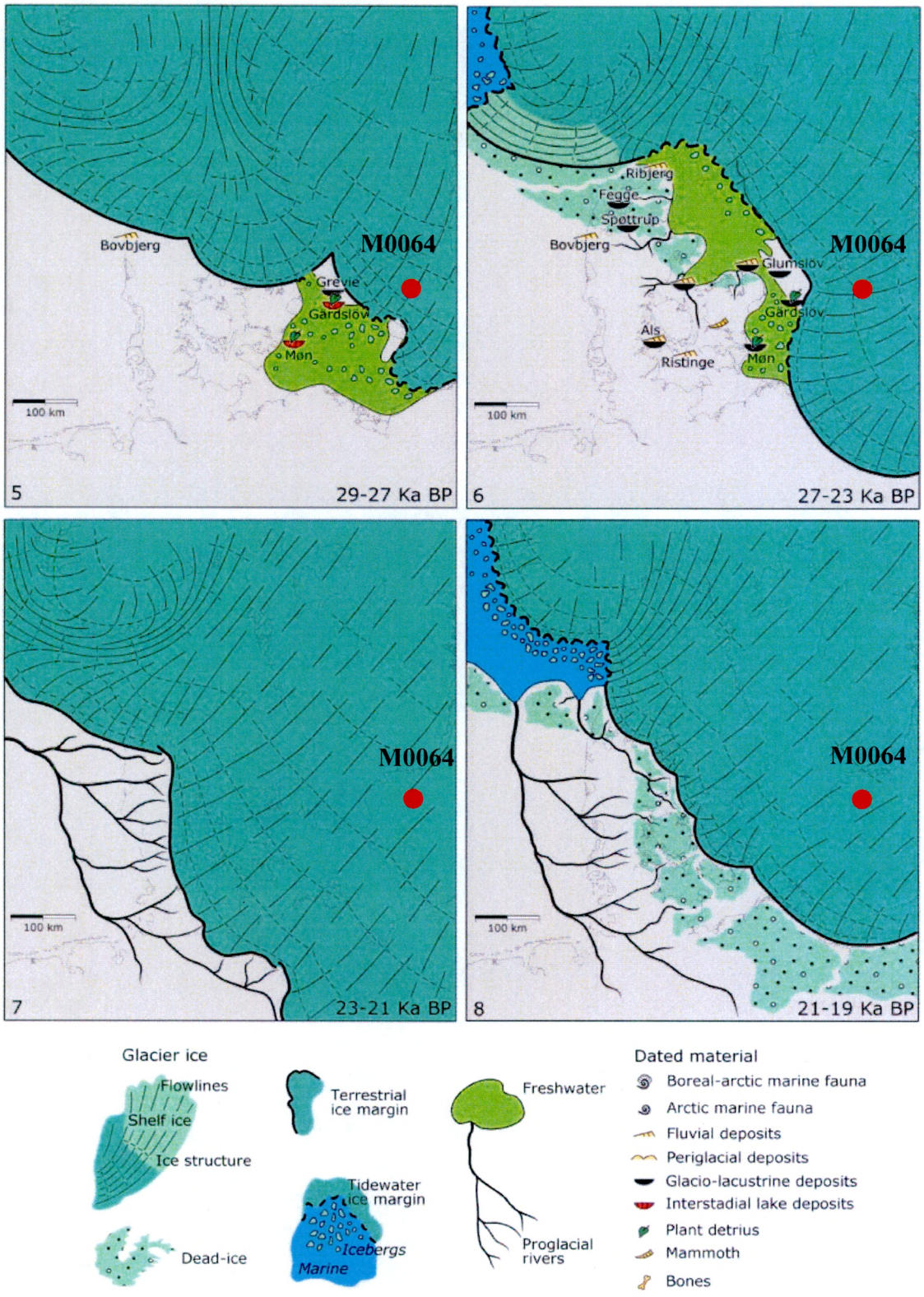

Figure 29. Kattegat advance (Box 5), which reached northern Denmark, but not southern Skåne and the SIS progression leading to the LGM (Box 8) (Houmark-Nielsen and Kjaer, 2003).

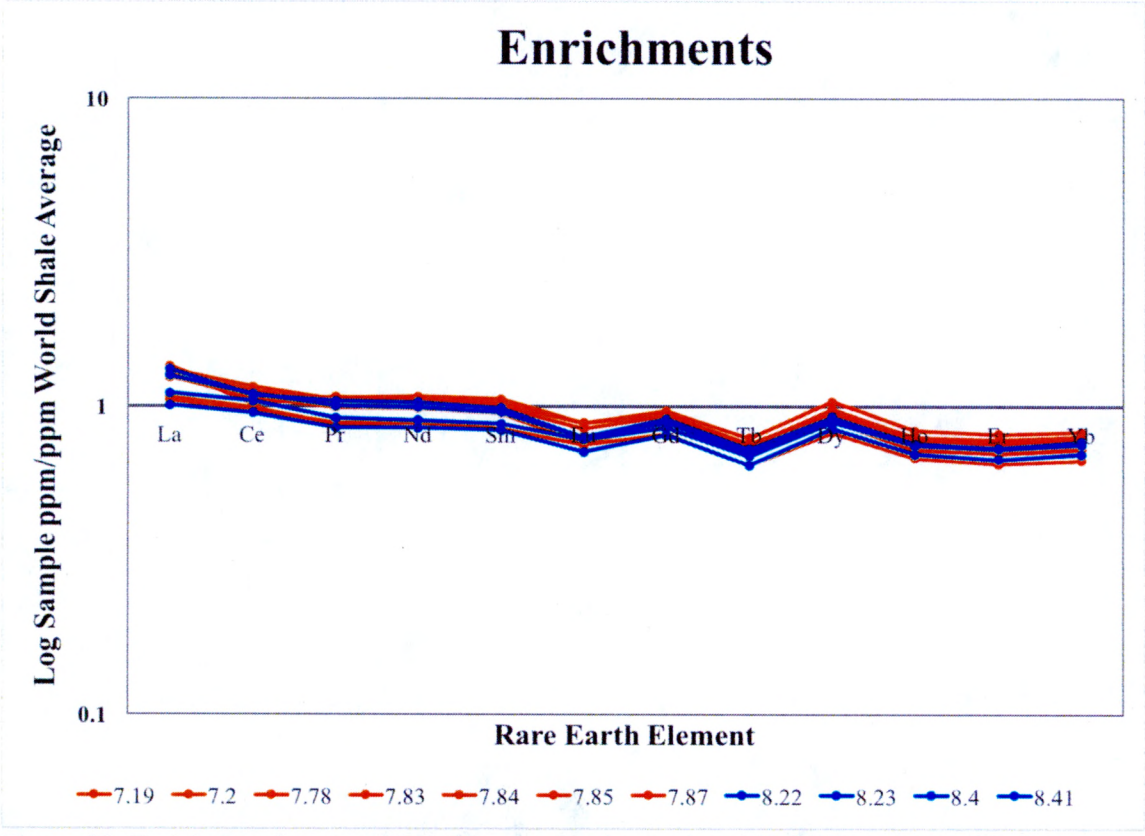

Figure 30. Enrichment factors of Unit IIIa samples (orange) and Unit IIIb samples (blue) in meters below sea floor, normalized with the World Shale Average (WSA) values taken from Piper and Bau, 2003.

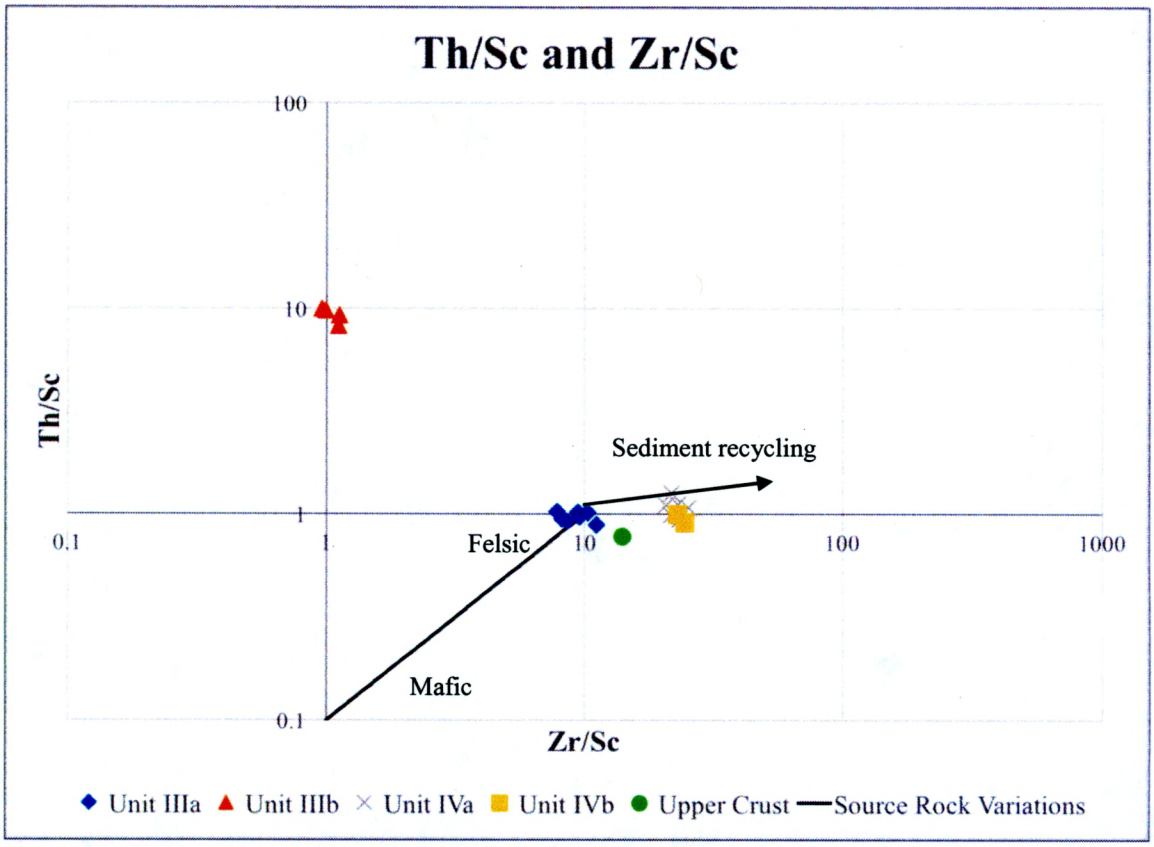

Figure 31. Th/Sc and Zr/Sc ratios (ppm) plotted by Unit with Upper Crust (McLennan, 2001), and source rock variations (Potter et al., 2005). Blue diamonds represent Unit IIIa, orange triangles indicate Unit IIIb, grey X's are Unit IVa, and yellow squares represent Unit IVb. Upper Crust is indicated by a green circle.

Figure 32. Timeline of recent SIS deglaciation, BIL development, and BIL drainage relative to Site M0064.

B. Tables

Table 1. Baltic Sea Stages. YS = Yoldia Sea. YD = Younger Dryas.

Baltic Sea Stage	Age	Description
Stage 3: Brackish Phase of YS	10,540 yr BP	Saline ingression north of Mt. Billingen, lasting ~300 years.
Stage 2: Freshwater Phase of YS	11,450 to 11,390 ± 80 years BP	Isostatic rebound causing basin shallowing. YD - Preboreal warming transition.
Stage 1: BIL drainage	12,867 ± 66 cal. years BP	Freshwater release north of Mt. Billingen. ~10 – 25 m lake level drop in 1 – 2 years.

Table 2. Sample and method distribution throughout core M0064A and M0064D. Shaded boxes indicate which methods were used on each listed sample. XRF scanning took place at 1 cm intervals from sections 2H-1 to 5H-1 (2.21 mbsf - 13.59 mbsf) and is represented Table 2.

Depth (mbsf)	IODP Sample Name	Unit	Particle Size	ICP-OES	ICP-MS	Sample Notes
6.2	64D-3H-1W-70-72-B	IIIa				Mixed mud-silt lense
6.75	64D-3H-1W-125-127-M	IIIa				Brown-red mud
7.19	64D-3H-2W-20-22-M	IIIa				Indistinct brown-red laminae
7.2	64D-3H-2W-20-22-S	IIIa				Indistinct brown-red laminae
7.34	64D-3H-2W-34-36-M	IIIa				Brown-red mud
7.41	64A-3H-1W-40-42-M	IIIa				Red mud
7.78	64D-3H-2W-78-80-M	IIIa				Brown-red mud
7.83a	64D-3H-2W-83-85-S	IIIa				Brown-red silt
7.83b	64A-3H-1W-81-83-S	IIIa				Brown-red silt
7.84	64A-3H-1W-81-83-BROWN	IIIa				Dark brown mud
7.85	64D-3H-2W-83-85-BROWN	IIIa				Dark brown mud
7.87	64D-3H-2W-87-89-BROWN	IIIa				Dark brown mud
7.91	64A-3H-1W-90-92-M	IIIb				Grey-red mud
7.92	64A-3H-1W-90-92-S	IIIb				Grey-red silt
8.12	64D-3H-2W-112-114-M	IIIb				Grey mud
8.13	64D-3H-2W-112-114-S	IIIb				Grey silt
8.22	64D-3H-2W-122-124-M	IIIb				Brown mud
8.23	64D-3H-2W-122-124-S	IIIb				Light tan silt
8.41	64A-3H-1W-140-142-M	IIIb				Brown mud
8.42	64A-3H-1W-140-142-S	IIIb				Brown silt
8.91	64A-3H-2W-40-42-B	IIIb				Light tan disturbed mud-silt laminae
9.2	64D-4H-1W-40-42-B	IIIb				Disturbed mud-silt laminae
9.21	64D-4H-1W-40-42-S	IIIb				Disturbed silt laminae
9.41	64A-3H-2W-90-92	IVa				Grey-red diamict
9.91	64A-3H-3W-10-12	IVa				Grey diamict
10.2	64D-4H-1W-140-142	IVa				Silty red glacial powder
10.41	64A-4H-1W-10-12	IVa				Grey diamict
10.91	64A-4H-1W-60-62	IVa				Grey diamict
11.2	64D-4H-2W-90-92	IVa				Silty red glacial powder
11.91	64A-4H-2W-10-12	IVa				Grey diamict
12.2	64D-5H-1W-10-12	IVa				Grey-red diamict
12.41	64A-4H-2W-60-62	IVa				Grey diamict
12.74	64D-5H-1W-64-66	IVa				Grey-red-brown diamict
12.91	64A-4H-2W-110-112	IVa				Grey-red muddy diamict
13.2	64D-5H-1W-110-112	IVa				Red-brown diamict
13.39	64A-4H-3W-39-41	IVa				Grey-red muddy diamict
13.7	64D-5H-2W-10-12	IVa				Red diamict
14.2	64D-5H-2W-60-62	IVa				Red diamict
14.7	64D-5H-2W-110-112	IVa				Red diamict
15.2	64D-5H-3W-30-32	IVa				Red diamict
15.5	64D-5H-3W-60-62	IVa				Red diamict
16.6	64D-7N-1W-20-22	IVa				Grey diamict
17	64D-7N-1W-60-62	IVa				Grey diamict
17.5	64D-7N-1W-110-112	IVa				Grey diamict
17.64	64D-8N-1W-24-26	IVa				Grey diamict
18	64D-8N-1W-60-62	IVa				Grey diamict
25.7	64D-15N-1W-30-32	IVb				Grey diamict, shell
26.66	64D-16N-1W-26-28	IVb				Grey diamict
28.98	64D-18N-1W-58-60	IVb				Grey diamict, grain supported
29.87	64D-19N-1W-47-49	IVb				Grey diamict
31.87	64D-21N-1W-47-49	IVb				Grey diamict
32.83	64D-22N-1W-43-45	IVb				Grey diamict
33.78	64D-23N-1W-38-40	IVb				Grey diamict

Table 3. List of core sections scanned at 1-cm intervals using XRF methodology, with according depths (mbsf) and Unit(s).

Core Section	Depths Scanned (mbsf)	Unit
347-64D-2H-1	2.21-3.69	IIIa
347-64D-2H-2	3.71-4.98	IIIa
347-64D-2H-3	5.01-5.42	IIIa
347-64D-3H-1	5.76-6.99	IIIa
347-64D-3H-2	7.01-8.29	IIIa and IIIb
347-64D-3H-3	8.32-8.78	IIIb
347-64D-3H-CC	8.86-9.09	IIIb
347-64D-4H-1	8.81-10.29	IIIb and IVa
347-64D-4H-2	10.31-11.59	IVa
347-64D-4H-3	11.61-11.95	IVa
347-64D-5H-1	12.11-13.59	IVa

Table 4. Listed elements used and accordingly methodology, shaded in grey.

Element	ICP-OES	ICP-MS	XRF
Al			
Ti			
Mn			
Zr			
La			
Ce			
Pr			
Nd			
Sm			
Eu			
Gd			
Tb			
Dy			
Ho			
Er			
Yb			
Th			
Sc			
Fe			
Ca			
S			

Table 5. Major Elements in weight percent, Zr in ppm (Zr/Al Calculated with Al ppm values).

			Major Element Wt. %						Chemical Ratios			
Sample Name	**Depth (mbsf)**	**Unit**	**TiO2**	**Ti**	**Al2O3**	**Al**	**Mn**	**Zr (ppm)**	**Al2O3/ TiO2**	**Al/Ti**	**Mn/Al**	**Zr/Al (ppm)**
64D-3H-2W-20-22-M	7.19	IIIa	0.867	0.520	21.400	11.326	0.061	124.174	24.687	21.794	0.0054	0.091
64D-3H-2W-20-22-S	7.2	IIIa	0.903	0.542	20.076	10.625	0.069	151.506	22.220	19.616	0.0065	0.070
64D-3H-2W-78-80-M	7.78	IIIa	0.872	0.523	20.788	11.002	0.059	151.119	23.831	21.038	0.0054	0.073
64A-3H-1W-81-83-S	7.83	IIIa	0.926	0.555	18.448	9.764	0.064	164.918	19.927	17.591	0.0066	0.059
64A-3H-1W-81-83-BROWN	7.84	IIIa	0.808	0.484	20.773	10.994	0.059	163.548	25.718	22.704	0.0054	0.067
64D-3H-2W-83-85-BROWN	7.85	IIIa	0.862	0.517	19.994	10.582	0.062	136.895	23.201	20.482	0.0058	0.077
64D-3H-2W-87-89-BROWN	7.87	IIIa	0.877	0.526	17.674	9.354	0.065	161.273	20.162	17.799	0.0069	0.058
64D-3H-2W-122-124-M	8.22	IIIb	0.856	0.513	20.227	10.705	0.066	144.455	23.620	20.852	0.0062	0.074
64D-3H-2W-122-124-S	8.23	IIIb	0.862	0.517	17.667	9.350	0.074	125.764	20.501	18.098	0.0079	0.074
64A-3H-1W-140-142-M	8.4	IIIb	0.853	0.512	20.064	10.619	0.064	131.661	23.514	20.758	0.0060	0.081
64A-3H-1W-140-142-S	8.41	IIIb	0.851	0.510	17.266	9.138	0.069	140.762	20.284	17.907	0.0075	0.065
64D-4H-1W-140-142	10.2	IVa	0.502	0.301	10.173	5.384	0.054	160.410	20.283	17.906	0.0101	0.034
64D-5H-1W-110-112	13.2	IVa	0.484	0.290	10.166	5.381	0.053	174.069	21.004	18.543	0.0098	0.031
64D-5H-2W-10-12	13.7	IVa	0.464	0.278	9.965	5.274	0.051	173.038	21.459	18.944	0.0096	0.030
64D-5H-2W-60-62	14.2	IVa	0.471	0.283	9.931	5.256	0.079	146.683	21.063	18.594	0.0151	0.036
64D-5H-2W-110-112	14.7	IVa	0.449	0.269	9.743	5.156	0.064	157.060	21.713	19.168	0.0123	0.033
64D-7N-1W-20-22	16.6	IVa	0.484	0.290	10.234	5.416	0.064	163.721	21.162	18.682	0.0119	0.033
64D-15N-1W-30-32	25.7	IVb	0.455	0.273	9.658	5.111	0.044	160.615	21.240	18.751	0.0085	0.032
64D-22N-1W-43-45	32.83	IVb	0.438	0.263	8.965	4.745	0.031	157.210	20.464	18.066	0.0066	0.030
Upper Crustal Values (McLennan, 2001)			-	**Ti**	-	**Al**	**Mn**	**Zr**	-	**Al/Ti**	**Mn/Al**	**Zr/Al**
			-	0.410	-	8.040	0.060	0.019	-	19.610	0.0075	0.046

Table 6. Trace Elements in ppm.

Sample Name	Depth (mbsf)	Unit	La	Ce	Pr	Nd	Sm	Eu	Gd	Tb	Dy	Ho	Er	Yb	Th	Sc	Zr	Th/Sc	Zr/Sc
64D-3H-2W-20-22-M	7.19	IIIa	1.70	1.38	1.41	1.44	1.59	1.40	5.60	1.33	1.41	1.21	1.15	1.20	16.39	15.86	124.17	1.03	7.83
64D-3H-2W-20-22-S	7.2	IIIa	1.74	1.46	1.46	1.50	1.66	1.55	5.91	1.42	1.54	1.33	1.25	1.27	16.32	16.00	151.51	1.02	9.47
64D-3H-2W-78-80-M	7.78	IIIa	1.84	1.36	1.52	1.55	1.72	1.62	5.99	1.43	1.54	1.33	1.27	1.28	17.50	18.48	151.12	0.95	8.18
64A-3H-1W-81-83-S	7.83	IIIa	1.81	1.32	1.52	1.57	1.76	1.62	6.12	1.52	1.63	1.40	1.33	1.33	16.27	16.00	164.92	1.02	10.31
64A-3H-1W-81-83-BROWN	7.84	IIIa	1.79	1.50	1.50	1.55	1.70	1.61	5.99	1.45	1.50	1.31	1.23	1.26	17.59	19.11	163.55	0.92	8.56
64D-3H-2W-83-85-BROWN	7.85	IIIa	1.46	1.28	1.25	1.29	1.42	1.37	5.15	1.24	1.30	1.14	1.06	1.07	13.93	14.25	136.89	0.98	9.60
64D-3H-2W-87-89-BROWN	7.87	IIIa	1.43	1.26	1.25	1.30	1.46	1.43	5.47	1.33	1.41	1.23	1.15	1.16	13.00	14.53	161.27	0.90	11.10
64D-3H-2W-122-124-M	8.22	IIIb	1.71	1.42	1.42	1.45	1.60	1.45	5.62	1.36	1.44	1.26	1.19	1.23	17.28	15.48	144.45	1.12	9.33
64D-3H-2W-122-124-S	8.23	IIIb	1.38	1.23	1.21	1.24	1.39	1.30	5.12	1.23	1.33	1.17	1.09	1.12	12.65	12.79	125.76	0.99	9.83
64A-3H-1W-140-142-M	8.4	IIIb	1.80	1.41	1.48	1.50	1.64	1.45	5.77	1.39	1.45	1.26	1.19	1.23	17.59	15.82	131.66	1.11	8.32
64A-3H-1W-140-142-S	8.41	IIIb	1.51	1.35	1.30	1.32	1.46	1.43	5.41	1.32	1.39	1.25	1.18	1.20	13.42	14.04	140.76	0.96	10.02
64D-4H-1W-140-142	10.2	IVa	0.81	0.81	0.81	0.83	0.97	0.96	3.50	0.96	1.02	0.91	0.84	0.87	7.42	7.44	160.41	1.00	21.56
64D-5H-1W-110-112	13.2	IVa	0.76	0.76	0.77	0.78	0.90	0.92	3.66	0.91	0.95	0.86	0.80	0.84	7.40	6.89	174.07	1.07	25.27
64D-5H-2W-10-12	13.7	IVa	0.84	0.84	0.83	0.85	0.97	1.00	3.91	0.95	1.01	0.92	0.85	0.91	8.44	7.53	173.04	1.12	22.97
64D-5H-2W-60-62	14.2	IVa	0.67	0.71	0.72	0.74	0.85	0.87	3.53	0.85	0.90	0.79	0.74	0.77	5.95	6.29	146.68	0.95	23.31
64D-5H-2W-110-112	14.7	IVa	0.76	0.81	0.80	0.82	0.96	1.00	3.88	0.95	0.99	0.89	0.83	0.85	9.15	7.21	157.06	1.27	21.78
64D-7N-1W-20-22	16.6	IVa	0.98	0.96	0.93	0.96	1.10	1.11	4.34	1.06	1.15	1.00	0.94	0.94	8.76	7.94	163.72	1.10	20.62
64D-15N-1W-30-32	25.7	IVb	0.64	0.66	0.68	0.69	0.79	0.84	3.36	0.84	0.85	0.78	0.71	0.75	6.04	6.58	160.61	0.92	24.41
64D-22N-1W-43-45	32.83	IVb	0.72	0.73	0.72	0.74	0.84	0.87	3.45	0.85	0.88	0.78	0.72	0.75	6.84	6.85	157.21	1.00	22.94
			Trace Element (ppm)															Chemical Ratios	
Upper Crustal Values (McLennan, 2001)			La	Ce	Pr	Nd	Sm	Eu	Gd	Tb	Dy	Ho	Er	Yb	Th	Sc	Zr	Th/Sc	Zr/Sc
			30	64	7.1	26	4.5	0.88	3.8	0.64	3.5	0.8	2.3	2.2	10.7	13.6	190	0.79	13.97